Effects and Modifications in In/Se and In/Sb Systems by Swift Heavy Ion Irradiation

Thesis submitted to
Cochin University of Science and Technology

By

R. Sreekumar

In partial fulfillment of the requirements
for the award of the degree of

DOCTOR OF PHILOSOPHY

Department of Physics
Cochin University of Science and Technology
Cochin – 682 022, Kerala, India

October 2008

Effects and Modifications in In/Se and In/Sb Systems by Swift Heavy Ion Irradiation

Ph.D thesis in the field of material science

Author:

R. Sreekumar
Thin Film Photovoltaic Division,
Department of Physics
Cochin University of Science and Technology
Kochi - 682 022, Kerala, India
E-mail: srii10@gmail.com

Advisor:

Dr. K. P. Vijayakumar
Professor,
Department of Physics
Cochin University of Science and Technology
Kochi - 682 022, Kerala, India
E-mail: kpv@cusat.ac.in

Cochin University of Science and Technology
Kochi - 682 022, Kerala, India

October 2008

Dedicated

To Achan and Amma

Prof. K. P. Vijayakumar
Department of Physics
Cochin University of Science and Technology
Cochin – 682 022

21st October 2008

Certificate

Certified that the work presented in this thesis entitled "*Effects and Modifications in In/Se and In/Sb Systems by Swift Heavy Ion Irradiation*" is based on the authentic record of research done by Mr. R. Sreekumar under my guidance in the Department of Physics, Cochin University of Science and Technology, Kochi - 682 022, India and has not been included in any other thesis submitted for the award of any degree.

Prof. K. P. Vijayakumar
(Supervising Guide)

Phone : +91 484 2577404 extn 24 Fax: 91 484 2577595 email: kpv@cusat.ac.in

Declaration

I hereby declare that the work presented in the thesis entitled "Effects and modifications in In/Se and In/Sb systems by swift heavy ion irradiation" is based on the original research work done by me under the guidance of Prof. K. P. Vijayakumar, Department of Physics, Cochin University of Science and Technology, Kochi - 682022, India and has never been included in any other thesis submitted for the award of any degree.

R. Sreekumar

Kochi – 682022
21st October 2008

Acknowledgements

I wish to express my deepest sense of gratitude to my guide and supervisor Prof. K. P. Vijayakumar, who, in spite of all the responsibilities and duties, found time to share his expertise and knowledge and inspired us to work towards the chosen goal with utmost confidence. I am deeply indebted to him for his gentle and inspiring guidance, forbearance, constant encouragement and support.

It is with a particular pleasure that I acknowledge Dr. C. Sudha Kartha for her guidance and valuable suggestions during my entire research work. The encouragement and ideas given by her during our lab meetings is worth mentioning here.

I would like to express my sincere thanks to Dr. D. K. Avasthi, Material Science division, Inter University Accelerator Centre (IUAC) (formerly Nuclear Science Centre), New Delhi, India for his valuable advise and guidance for completing ion irradiation work. I greatly acknowledge his valuable discussions and suggestions throughout this work.

I would like to express my gratitude to Dr. S. A. Khan, IUAC, Dr. Manavendar Kumar, D. C. Agarwal, Y. K. Mishra and S. R. Abhilash, target Lab, IUAC for their sincere co-operation extended to me during online RBS measurements and all the beam time I have utilized. I would like to thank Dr. Ambuj Tripati, IUAC and Vikas for taking AFM measurements.

I am very much obliged and thankful to IUAC, New Delhi for providing ion beam irradiation facility for experiment and granting fellowship during my research work. I gratefully acknowledges 'Pelletron group', IUAC for providing stable ion beams during experiments.

I am thankful to Institute of Physics, Bhubaneswar, India for providing RBS experimental facility. I would like to thank Dr. Biju Raj Sekhar, Boby and Sinu for there excellent support and assistance during RBS experiment at IOP.

I am grateful to Y Kashiwaba and Abe, Department of Electrical and Electronic Engineering, Iwate University, Japan for XPS measurements and the support they have extended to me for completing my Ph.D work.

I extend my sincere thanks to Prof. Godfrey Louis, The Head, Department of Physics, Cochin University of Science and Technology and all other former Head of the Department for allowing me to use the facilities. I greatly acknowledge the help and guidance of all the faculty members of the Department of Physics through out my research work.

With a sense of gratitude, I am thankful to all the office and library staff of the Department of Physics and the technical staff at USIC for all the help and cooperation.

I specially appreciate the sincere support of Dr. P. M. Ratheesh Kumar for all the support extended to me during my initial stage of research work.

I would like to express my sincere appreciation to my colleagues in the Thin Film Photovoltaic Division, Ramkumar sir, Paulraj, Shyamala teacher, Teny Teresa John, Beena, Sreekumar, JK, Kishore, Anita, Deepa, Tina, Meril, Susan, Vimal, Pramitha, Rajesh Menon, Rajesh C S, Rajesh Mon, Sajeesh, Manju, Dhanya, Nimmi, Subramanyan, Jafar, Poornima and Sree Roop for all the help they had extended to me

I also extend my thanks to Jisha, Vinayaraj, Senoy, Arun V, Arun A, Sasankan, Rajeev, Amritesh, Kannan, Rajesh, Swapna, Hysen, Lakshmi, Thangaraju, Sija,

Indu, Salini, Selvi, Sajeev, Reshmi, Manojettan and all my friends in Department of Physics, CUSAT for their sincere help and co-operation throughout this work.

I am thankful to Ramankutty sir for encouraging me in my educational endeavors during my M.Sc. Studies.

I am greatly indebted to love and care showered upon me by my relatives-in-law.

I record my deep and utmost gratitude to my parents, brother, sister-in-law and Meenakshi for their selfless support, motivation, encouragements, patience and tolerance during the entire period of my work.

I thank my wife Asha for being there for me always.

I thank all my well wishers.

Last but not least I thank the God almighty for the blessings he has showered on me.

R. Sreekumar

Contents

Page no:

Preface

Publications

Chapter 1 1

A brief introduction to swift heavy ions, need of thin film Solar cells, preparation and characterisation techniques used in the study

1.1 Introduction 5

1.2 Swift heavy ions 6

1.2.1 Production of swift heavy ions 7

1.2.2 Effects and use of swift heavy ions 8

1.3 Ion beam mixing 10

1.4 Need for thin film solar cells 12

1.5 Solar cells using compound semiconductors 13

1.6 Material for window layer 14

1.7 Materials under study 16

1.7.1 Indium selenide 16

1.7.2 Indium antimonide 18

1.8 Thin Film Preparation Techniques 19

1.8.1 Chemical bath deposition technique 20

(a) Selenium film deposition 21

1.8.2 Thermal evaporation by resistive heating 22

1.8.3 Electron beam evaporation 23

1.9 Characterisation techniques 24
1.9.1 Thin film thickness 24
1.9.2 X-ray diffraction studies 25
1.9.3 Optical characterisation 27
(a) Determination of band gap energy 27
(b) Photoluminescence 28
1.9.4 Electrical Characterization 32
(a) Sheet resistance 32
(b) Photosensitivity 33
(c) Conductivity type 34
1.9.5 X-ray Photoelectron Spectroscopy (XPS) 35
1.9.6 Atomic Force Microscopy (AFM) 36
1.9.7 Rutherford backscattering technique 38

Chapter 2 45

Part A - Effect of annealing on the formation of γ-In_2Se_3

2.1 Introduction 49
2.2 Experiment 49
2.3 Results and discussion 51
2.3.1 X-ray diffraction analysis 51
2.3.2 Optical studies 54
2.3.3 X-ray photoelectron spectroscopy analysis 59
2.3.4 Electrical studies 63
2.3.5 Rutherford backscattering analysis 64
2.4 Conclusion 66

Part B - Effect of indium concentration on the c-axis growth of γ-In_2Se_3 67

2.5 Introduction 71

2.6 Results and discussion 72

2.6.1 X-ray diffraction analysis 72

2.6.2 Optical Absorption Studies 79

2.6.3 Electrical Studies 86

2.7 Conclusion 87

Chapter 3 93

Investigations on the anomalous negative photoconductivity in γ-In_2Se_3

3.1 Introduction 97

3.2 Experiment 98

3.3 Result and discussion 99

3.3.1 X-ray diffraction analysis 99

3.3.2 Optical studies 100

(a) Optical absorption 100

(b) Photoluminescence 102

3.3.3 Photoconductivity studies 104

(a) Room temperature photoconductivity 104

(b) Low temperature photoconductivity 109

3.4 Conclusion 111

Chapter 4 113

Low temperature material synthesis and ion beam mixing in In/Se bilayer systems using swift heavy ion irradiation

Part A - Online interface mixing study using swift heavy ions: An attempt 115

4.1 Introduction 119

4.2 Experiment 120

4.3 Principle of Rutherford backscattering technique 122

4.4 Discussion 125

4.5 Conclusion 131

Part B - Single-phase InSe formation using SHI irradiation and low temperature annealing 133

4.6 Introduction 137

4.7 Experiment 138

4.8 Result and discussion 139

4.8.1 Rutherford backscattering analysis 139

4.8.2 X-ray diffraction analysis 140

4.8.3 Optical absorption study 143

4.9 Conclusion 145

Part C - Ion beam mixing in In/Se bilayer system at different electronic energy regime 147

4.10 Introduction 151

4.11 Experiment 152

4.12 Results and Discussion 153

4.12.1 Rutherford backscattering analysis 153

(a) Irradiation using 100 MeV Ag ions 153

(b) Irradiation using 80 MeV Ni ions 154

(c) Irradiation using 90 MeV Si ions 155

4.12.2 Atomic force microscopy analysis 159

4.12.3 X-ray diffraction analysis 161

(a) Irradiation using 100 MeV Ag ions 161

(b) Irradiation using 80 MeV Ni ions 166

(c) Irradiation using 90 MeV Si ions 169

4.12.4 Optical absorption studies 171

(a) Irradiation using 100 MeV Ag ions 171

(b) Irradiation using 80 MeV Ni ions 177

(c) Irradiation using 90 MeV Si ions 178

4.13 Conclusion 182

Chapter 5 189

Effect of SHI irradiation on γ-In_2Se_3 thin films

5.1 Introduction 193

5.2 Experiment 194

5.3 Results and discussion 196

5.3.1 X-ray diffraction analysis 196

5.3.2 Optical studies 201

(a) Determination of band gap and Urbach energy 201

(b) Photoluminescence 208

5.3.3 Electrical study 212

(a) Room temperature photoconductivity 212

5.4 Conclusion 215

Chapter 6 219

Integration of InSb in Si matrix using swift heavy ion irradiation

6.1 Introduction 223

6.2 Experiment 224

6.3 Results and discussion 225

6.3.1 X-ray diffraction analysis 225

(a) Irradiation using 100 MeV Au ions 225

(b) Irradiation using 100 MeV Ag ions 227

(c) Irradiation using 80 MeV Ni ions 228

6.3.2 Rutherford backscattering analysis 231

6.3.3 X-ray photoelectron spectroscopy analysis 234

6.4 Conclusion 239

Chapter 7 243

Summary and outlook

7.1 Conclusion 247

7.2 Scope for future work 248

Preface

Currently, there is an increasing interest to reduce the synthesis temperature of materials. Ion beam mixing (IBM) is one of the tools for synthesis of compound formation using low energy ions. The compound phases, in general, are achievable at relatively lower temperature in the process of IBM. IBM by high energy heavy ions was first demonstrated by Dufour et al. in 1993 and since then several researchers have shown mixing in various insulator/insulator, metal/insulator, metal/metal and metal/semi-conductor systems. These high energy ion beams are also used for material modification, manipulation of electrical, optical and structural properties of materials. In the present work we used high energy heavy ion beams for preparation and modification of indium selenide thin films. We also used these ion beams to prepare InSb thin films on Si substrate at room temperature, and found that it is possible even to integrate InSb with Si.

Since 1970's silicon solar cells are dominating the photovoltaic industry. One of the main drawbacks of the Si based solar cells is the high production cost due to the usage of extra pure Si wafers. This leads to the thin film solar cells which use very less amount of material, as these are only few micro-meters thick whereas the Si solar cells used are about 300 micro meter thick Si. Compound semiconductor based solar cell uses Gallium arsenide, cadmium telluride, copper indium diselenide and copper indium gallium diselenide as absorber layer. All these material uses cadmium sulphide as window layer, which is very toxic. When it is considered for large scale pilot production, it can cause environmental hazards. Lots of research is being carried out to replace CdS window layer. Suitable substitutes for CdS are In(OH, S), SnS_2, ZnSe, In_2S_3, In_2Se_3 etc. In the present study we are focussing on In_2Se_3 films. One of the main concerns with In_2Se_3 is the presence of multi-phases of indium selenide in a single layer. By the present work, we prepared and characterised single phase

indium selenide thin films and recommend this material as a plausible substitute for CdS window layer.

Indium antimonide (InSb) is the binary semiconductor in the III-V group having the lowest band gap of 0.17eV at 300K, corresponding to infrared wavelength 6.2 μm. This material is mainly used in fields of magnetic sensors, infrared detectors and in infrared laser devices. Direct growth of InSb on the Si substrate is very difficult because of large lattice mismatch - over 19% - and different thermal expansion co-efficient between InSb and Si. In the present study we tried to grow InSb on Si using ion beam irradiation. By Integrating InSb with highly advanced Si circuitry, one could get significant gain in terms of reliability and speed. Moreover, high density of integration will allow considerable cost savings in the manufacturing process.

In the present work we used 100 MeV Au, 100 MeV Ag, 80 MeV Ni, 40 MeV and 90 MeV Si ions for irradiating In/Se and In/Sb systems. The effects and modifications on these systems were studied in detail. The major findings of the work is summarised in six chapters preceded by an introductory chapter.

Chapter 1 gives a brief introduction to swift heavy ions, its effects and use in material modification such as manipulation of structural, optical and electrical properties. The need of compound semiconductor based thin film solar cells is also described. The importance of cadmium free material for window layers in solar cell fabrication is suggested and a material (indium selenide) which is less toxic as compared to CdS is recommended. Finally the preparation and characterisation technique used in the present study is narrated.

Chapter 2 is divided into parts. First part gives a detailed study on the effect of annealing In/Se bilayer system at temperature ranging from 100°C to 400°C, leading to the formation of different phases of indium selenide. We used X-ray diffraction technique and optical absorption studies to identify multi-phases of

indium selenide present in the film. Present study proved that multi-phased films were formed at lower annealing temperatures and annealing at 400°C is required to obtain single phase indium selenide thin films. The second part deals with effect of indium concentration on the growth of γ-In_2Se_3 along the c-axis. We tried to grow In_2Se_3 along c-axis by varying annealing temperature and indium concentration. It was observed that the growth of In_2Se_3 crystallites along (006) plane (c-axis) depends on indium concentration

Chapter 3 deals with the photoconductivity studies of indium selenide thin films. Interestingly γ-In2Se3 film showed negative photoconductivity at room temperature. We analysed the cause of negative photoconductivity in the sample and found that the trapping of photogenerated carriers and destruction of conduction band electrons resulted in negative photoconductivity. Photoconductivity of the films exhibited a strong dependence on the concentration of indium in the films. Trap levels and recombination centre in the samples were identified using optical absorption and photoluminescence studies respectively.

Chapter 4 is again divided into three parts. The first part of this chapter summarises the attempt to study on-line/in-situ ion beam mixing between In/Se bilayer system using 'Rutherford Backscattering Spectroscopy' with the help of 40 MeV silicon ions, deviating from conventional RBS using 3 MeV He ions. The second part deals with the formation of single phase indium selenide at lower annealing temperature induced by 40 MeV Si ion irradiation. In/Se bilayer system was irradiated using 40 MeV Si ions and annealed at different temperatures. In the case of irradiated sample, single phase indium selenide formation occurred at much lower annealing temperature as compared to the un-irradiated sample. Third part of the chapter elucidates the effects of inter-layer mixing between In/Se bilayer system at different electronic energy regimes. Irradiation study indicated the dependence of threshold fluence and energy of swift heavy ions required for interlayer mixing to take place between In/Se

bilayer systems. Optical absorption study depicted that the band gap of indium selenide can be tuned/ varied with the help of swift heavy ion irradiation followed by 100°C annealing.

Chapter 5 deals with the effect of 90 MeV Si ions on γ-In_2Se_3 thin films. Study proved that the optical band gap of indium selenide can be enhanced using SHI irradiation without any considerable variation in structural and electrical properties. The increase in optical band gap was attributed to the annihilation of localized defect bands, near the conduction and valence band edges, on irradiation. It was observed that the sample, which had negative photoconductivity, exhibited positive photoconductivity, after irradiation.

Chapter 6 presents the works done to integrate In/Sb with Si through swift heavy ion beam mixing. The samples of In/Sb deposited on Si substrate were irradiated using 100 MeV Au, 100 MeV Ag and 80 MeV Ni ions. Threshold fluence for InSb phase formation, without any post irradiation annealing, was found to be $1x10^{13}$ ions/cm^2 for all energies. But integration of InSb in Si matrix was achieved only using 100 MeV Au ions with a fluence of $3x10^{13}$ ions/cm^2.

In chapter 7 all the major achievements of the present work and scope for future works are summarised.

Journal publications

1. Enhancement of band gap and photoconductivity in gamma indium selenide due to SHI irradiation, **R. Sreekumar**, R. Jayakrishnan, C. Sudha Kartha, K.P. Vijayakumar, S. A. Khan, D. K. Avasthi. J. Appl. Phys. **103** (2008) 023709.
2. Anomalous photoconductivity in gamma In_2Se_3, **R. Sreekumar**, R. Jayakrishnan, C. Sudha Kartha and K.P. Vijayakumar, J. Appl. Phys. **100** (2006) 033707.
3. Swift heavy ion induced interface mixing in In/Sb, **R. Sreekumar**, P.M. Ratheesh Kumar, C. Sudha Kartha, K.P. Vijayakumar, D. Kabiraj, S.A. Khan, D. K. Avasthi, Y. Kashibawa and T. Abe, Semicond. Sci. Technol. **21** (2006) 382.
4. Different phases of indium selenide prepared by annealing In/Se bilater at various temperatures: Characterisation Studies, **R. Sreekumar**, R. Jayakrishnan, C. Sudha Kartha, K. P. Vijayakumar, Y. Kashibawa and T. Abe. Sol. Energy Mater. Sol. Cells **90** (2006) 2908.
5. SHI induced single-phase InSe formation at lower annealing temperature, **R. Sreekumar**, P.M. Ratheesh kumar, C. Sudha Kartha, K.P. Vijayakumar, D. Kabiraj, S.A. Khan and D. K. Avasthi, Nucl. Instr. and Meth. B **244** (2006) 190.

Conference publications

1. Use of SHI irradiation in gamma In_2Se_3 thin films for PV devices in outer space application, **R. Sreekumar**, Anita R. Warrier, C. Sudha Kartha, K. P. Vijayakumar, S. A. Khan, D. K. Avasthi. 2nd European Optical Society Tropical Meet: Optical Microsystems '07, September 30th to 3rd October 2007, Capri, Italy.
2. Effect of indium concentration and annealing temperature on the c-axis growth of γ-In_2Se_3, R**. Sreekumar**, C. Sudha Kartha and K. P. Vijayakumar, The 17th AGM of the Material Research Society of India,

February 2006, Lucknow, India

3. Effect of Indium concentration on the electrical properties of γ-In_2Se_3, **R. Sreekumar**, R.Jayakrishnan, C. Sudha Kartha and K. P. Vijayakumar, International conference on Optoelectronic Materials and Thin films for Advanced Technology 2005, Kochi, India.
4. SHI induced single-phase InSe formation at lower annealing temperature, **R. Sreekumar**, P.M. Ratheesh kumar, C. Sudha Kartha, K.P. Vijayakumar, D. Kabiraj, S.A. Khan and D. K. Avasthi, Indo-German workshop: Synthesis and modification of Nano structured materials by energetic ion beams, February 2005, New Delhi, India.
5. Enhanced interlayer mixing in In/Se bilayer system due to SHI irradiation, **R. Sreekumar**, C. Sudha Kartha, K.P. Vijayakumar, D. Kabiraj, S.A. Khan and D. K. Avasthi, DAE Solid State Physics Symposium 2004, Amritsar, India.

CHAPTER 1

A brief introduction to swift heavy ions, need of thin film solar cells, preparation and characterisation techniques used in the study

Abstract

A brief introduction to swift heavy ions and its effects on materials are described in the first part of this chapter and this is followed by the brief description on the need of compound semiconductor based thin film solar cells. The importance of cadmium free material as the window layer in solar cell fabrication is clearly brought in here and a material (indium selenide) which is less toxic as compared to CdS is recommended. Last part of the chapter deals with the preparation and characterisation techniques used in the present study.

1.1 Introduction

Semiconductor materials form the back bone of electronic industry. Tunability of the properties like structural, electrical, optoelectronic etc. and the capability to form junction make semiconductor the un-avoidable component in electronic devices. Since semiconductors can be prepared in 3-dimentional (bulk semiconductors), 2-dimentional (thin film), 1-dimentional (quantum wires) and in zero dimensional (quantum dot) forms, these materials can be accommodated in huge structured as well as in nano-structured devices. Among these materials, silicon is dominating the major share. Probably this may be because of the fact that research is being carried out in Si for the last 10 decades and researchers have already studied every aspect of this material. Later, lots of compound semiconductors were also introduced to the electronic industry. One of the main advantages of the compound semiconductors is the ability to manipulate the properties of the material by controlling the concentration / stoichiometry of the elements present in the compound. More over at least in some cases, the process of doping can be avoided/ becomes much easy process. Now compound semiconductors like GaAs, InSb, CdS, CdTe etc have already made their mark in the electronic industry along with Si.

Research in the field of usage of energetic ion beams in material science and devices has been constantly growing since last three decades. Low energy ion beams, which impart energy of an order ~10 KeV/ amu to the materials, are now an unavoidable/ indispensable part of modern electronic industry and analytical laboratories. Particle accelerators providing (medium energy) MeV ion beams are now available commercially and are being utilised by industries. Since last two decades, ion beams with energy ranging from few tens of MeV to GeV of different elements (practically all elements) are used for the manipulation of material properties, surface modification, characterisation and synthesis of novel materials. These high energy heavy ions, which losses about 1 MeV/ amu to the material, are known as swift heavy ions (SHI) and are now predominantly used

for the synthesis of metal silicides and electrical isolation in sub-micrometer regime. In the present work, we exploited SHI to modify the properties of indium selenide thin films and synthesis of indium selenide and indium antimonide thin films.

1.2 Swift heavy ions

First nuclear particle accelerator was built in 1930's. It was intended to probe into the nucleus by nuclear reactions. Since then, the particle accelerator was playing an important role in material science. Presently, accelerators which can deliver particles with an energy ranging from few kilo electron volts to several hundreds of giga electron volts are available. Particle or ion beams accelerated from these accelerators are classified into two, depending upon the energy imparted to the materials through which it passes. These are the low-energy and high energy heavy ion beams. Low energy ion beams have an energy ranging from few keV to few hundreds of keV, which losses energy to the material (up to 10 keV/ amu) through elastic collisions with the nucleus or atoms of the material. This type of energy loss is called 'nuclear energy loss' $(dE/dx)_n$ [1]. Whereas high energy heavy ions known as "swift heavy ions (SHI)" have energy ranging from few tens of MeV to few GeV and losses energy to the target ($\geq$ 1 MeV/amu) predominantly via inelastic collisions with the target material. These projectile ions impart energy to the electron cloud and these electrons transfer energy to the lattice via electron-phonon interactions [1]. This type of energy loss is called 'electronic energy loss' $(dE/dx)_e$, and in this case, the nuclear energy loss is very much negligible as compared to that of electronic energy loss. Figure 1.1 shows the 'nuclear and electronic energy loss' versus 'Energy' plot of Ag ions in indium. We can see that, at higher energies (100 MeV), nuclear energy loss is negligible as compared with electronic energy loss. Nuclear energy loss is maximum when the energy of Ag ion is 225 keV.

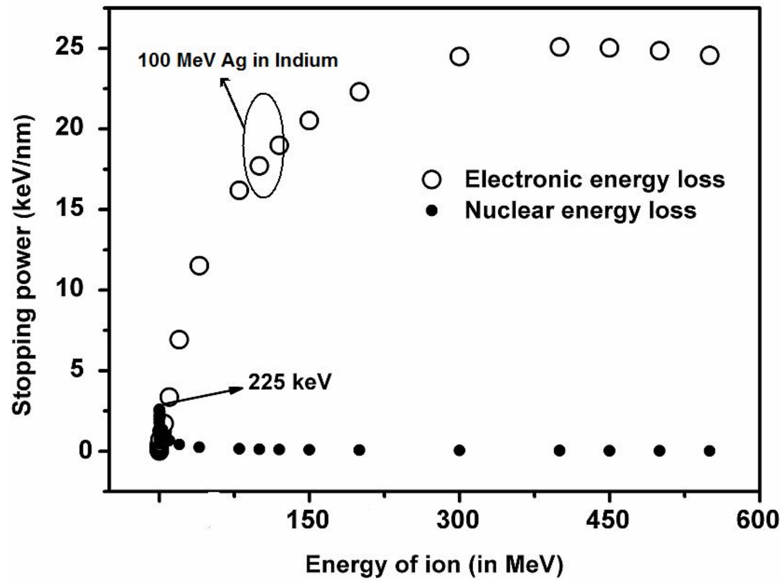

Figure 1.1: Nuclear energy loss and electronic energy loss versus 'Energy' plot.

1.2.1 Production of swift heavy ions

Swift heavy ions are generated using "particle accelerators". In the present study, we used the "15 UD Pelletron accelerator" available at the 'Inter University Accelerator Centre [IUAC]', New Delhi, India. This accelerator can generate a terminal voltage up to 15 million volts and ions of the required elements with energy of few hundred million electron volts (MeV). Figure 1.2 shows the schematic of the 15 UD Pelletron accelerator. Negative ions are generated in the SNICS (source of negative ions by cesium sputtering) ion source. The sputter source uses accelerated cesium ions, striking a cold cathode, to produce a negative ion beam of cathode material. A thin layer of cesium condensed over the cathode surface enhances negative ion production. These ions are extracted from the ion source by applying a positive injection voltage (generally V_{inj}=220 kV), with an energy ($E_{inj} = q\ V_{inj}$) where q is the charge state of the ion (q=1).

These singly charged ions are then mass analysed (by injector magnet) and are accelerated towards the Pelletron accelerator which is set with a positive terminal voltage of V. It will then acquire an energy, $E_1 = V$, (since q=1). Now the 'Charge stripper' stripes off the electrons from the ions to make the ions multiply charged positive ions. These positive ions are again accelerated with positive potential V so that the energy becomes, $E_2 = q\ V$, (where q is the charge state of the multiply charged ion). Ions with a total energy $E = E_{inj} + V + q\ V$, are then taken away to different beam line for irradiation studies, after the mass analysis.

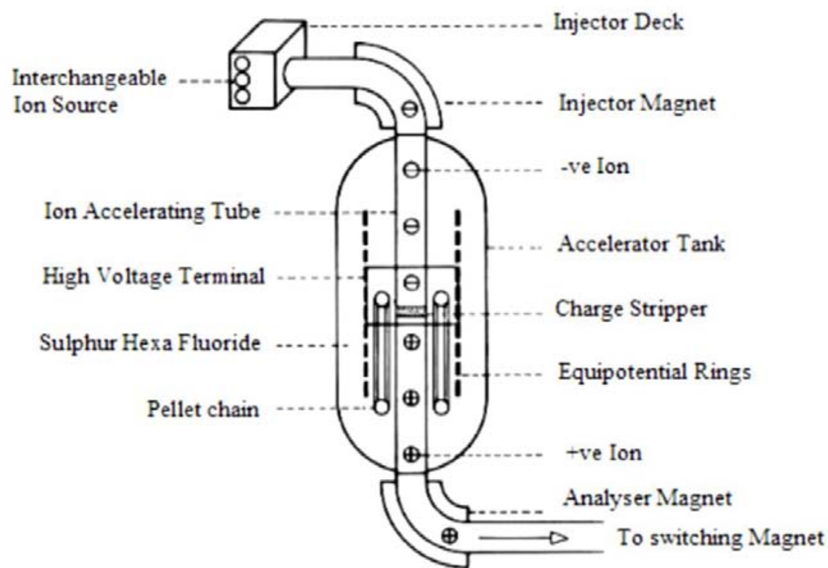

Figure 1.2: Schematic of 15 UD Pelletron accelerator.

1.2.2 Effects and use of swift heavy ions

As swift heavy ions (SHI) passes through the target material, it produces electronic excitation of the atoms in the material. Effect of SHI is different in different class of materials. It is more active in insulators than in metals and

semiconductors [2]. Different models were proposed to explain the effect of SHI in materials, coulomb explosion [3, 4, 5] and thermal spike model [6, 7, 8]. During the passage of SHI through the materials, the target atoms are ionised by electronic excitation. As a result, a cylinder of positive ion was created along the path of ions. These positive ions are mutually repulsive and explode radially due to conversion of electrostatic energy to coherent radial atomic movements under coulomb forces until the ions are screened by conduction electrons. As a result, ion tracks may be formed along the path of the projectile ion due to radial coulomb explosion. This process viz., coulomb explosion, is predominant in insulators where there is little conduction electrons. According to thermal spike model, SHI transmits its energy to the electrons of target materials as kinetic energy via inelastic collision. This kinetic energy is transmitted to the lattice by electron-phonon interactions, resulting in the increase of lattice temperature above the melting point of the material, followed by rapid quenching. This leads to the formation of 'amorphous track' along the path of the projectile ion when the melt solidifies.

Intense electronic energy deposition can be effectively used to modify material properties. Electronic energy loss in the materials can be varied from few eV/Å upto few 10's of keV/Å by choosing appropriate ions and energies. This remarkable ability of SHI provides unique opportunity to engineer properties of materials. SHI irradiation is now considered as an advanced technique to modify structural, optical and optoelectronic properties of thin films (thickness up to few micro meters) through intense electronic energy deposition. Vast number of studies was reported on structural and micro structural phase transformation in poly crystalline and single crystal materials due to swift heavy ion irradiation [9-17]. Tremendous energy deposition to the material can produce various changes in the material. It can produce columnar defect [18], point defect [19] and even amorphous tracks along the path of its motion [20].Using ion beam irradiation, one can create new defects as well as anneal out pre-existing defects in materials [21, 22]. SHI are also used to produce materials with novel properties, which

cannot be generated by any other means. In the present study we used SHI irradiation to manipulate optoelectronic properties of indium selenide thin films.

1.3 Ion Beam mixing

Currently, there is an increasing drive to reduce the synthesis temperature of materials. Ion beam mixing (IBM) is one of the tools for synthesis of compounds, using low energy ions, using which one can achieve compound formation at relatively lower temperatures [23, 24]. In this technique, bi-layers or multi-layers of materials are deposited over suitable substrates and these systems are subjected to ion beam irradiation. Ions lose energy to the target material through nuclear interaction with the atoms of target material (elastic collision). The atomic transport mechanism at the interface by low energy ion beams is explained as 'collision cascade' formed at the interface due to the atomic migration across the interface [25, 26]. When the energy transferred to the target atoms exceeds the displacement threshold of 20-50 eV, the atoms are pushed from their lattice positions and may collide with other target atoms [27]. In this manner, a recoil cascade is initiated, where thousands of atoms are relocated by a single ion [28]. If the recoil cascade overlaps with the interface of a layered system, this should result in atomic mixing in the vicinity of interface [29]. Using low energy ions, fluence of the order of $1x10^{17}$ ions/cm^2 is required to obtain mixing between bi-layer/multi-layer systems.

IBM, using high energy heavy ions, was first demonstrated by Dufour et al. [30] in 1993 and since then, several researchers have shown mixing in various insulator/insulator [2, 31], metal/insulator [32], metal/metal [33, 34] and metal/semi-conductor [24, 30, 35] systems. IBM, in the electronic energy regime, can be explained using two different models, namely (i) Coulomb-explosion model [3, 4, 5] and (ii) thermal spike model [3, 7, 8]. According to Coulomb-explosion model, as swift heavy ions passes through the material, it losses

energy to the electrons in the material, by exciting the electrons and ionizing the atom. This leads to ionized cylindrical zone along the path of the ions, with a strong electronic deficiency in the centre. This creates electrostatic repulsion between the positively charged atoms in the centre resulting in an explosion-like atomic motion perpendicular to the path of ions [6]. This can lead to mixing at the interface of the bi-layer/multi-layer systems. This type of mixing is only seen in insulators.

In the case of metals and semiconductors, mixing is explained using 'thermal spike' model. Energy transferred by the SHI to the lattice electrons will be imparted to the lattice via electron-phonon coupling. This results in the heating of the lattice and generation of 'Gaussian like' temperature profile around the path of the ions. The temperature can rise above the melting point of the material and cylindrical molten track of few nanometers can be formed. Mixing between bilayer can occur by inter-diffusion through the molten track, if the interface of the two materials in contact melted during irradiation. One of the advantage of IBM using high energy ($\geq$ 1 MeV/amu) heavy ions (SHI) over low energy ion mixing is that, the fluence required for mixing is about 10^{13} ions/cm^2 to 10^{14} ions/cm^2, which is two to three orders less, compared to low energy ion induced mixing [1].

In the present study, we used IBM to prepare indium selenide and indium antimonide from In/Se and In/Sb bilayer systems. These are two entirely different systems in which indium selenide is used in solar cell fabrication whereas, indium antimonide is used in magnetic and infrared sensors. By this work, we could investigate whether it is possible to make single phase indium selenide and/or enhance the optoelectronic properties of indium selenide by SHI irradiation. In the next section we discuss the need of thin film solar cells and the present status of our material, indium selenide, which can be used as window layer in solar cell fabrication.

1.4 Need for Thin Film Solar Cells

Solar cell is a device which converts sunlight directly to electrical energy. The modern solar cell consists of solid-state semiconductor 'P-N' junction, which was first developed by Bell Labs in 1954 by D. M. Chapman and C. S. Fuller, using Si. The first solar cell produced power less than a watt. Since then extensive research was being carried out on solar cell technology and now the cells are produced in quantities of several hundreds of gigawatt per year. Because of this, the cost of the photovoltaic (PV) devices has dropped from US $100 per watt [in 1970's] to about $4 per watt [in 2008].

Since 1970's silicon solar cells are dominating the PV industry. But even now, lot of research is being done to improve the efficiency of Si solar cells. Maximum efficiency of about 24.7% was achieved in single junction crystalline Si solar cells as of now in laboratory scale by M. Green et al. [36]. Silicon concentrator solar cell with efficiency of 27.6%, was achieved by a manufacturing company 'Amonix' (USA) [37]. One of the main drawbacks of the Si based solar cells is its high production cost due to the usage of extra pure Si wafers and the high degree of clean rooms required for the fabrication. Again the equipment used for the fabrications are very costly.

This leads to the thin film solar cells which use very less amount of material, as these are only few micro-meters thick and can efficiently convert light into electrical energy. Although thin film solar cells produce less electricity per square meter than the conventional Si solar cells, they make up for this by using orders of magnitude less active material per square meter. This can make significant savings in comparison with the conventional Si solar cells which are 100's of micrometers thick. In the case of Si solar cells, for generating one watt of electricity, one requires about $1.14 worth Si, while it requires only $0.14 worth semiconductor in thin film solar cells.

1.5 Solar Cells Using Compound Semiconductors

The materials for solar cell fabrication are selected on the basis of the properties of the material such as absorption co-efficient, photoconductivity, mobility of the carriers, optical band gap etc. The materials used should have high absorption co-efficient in the visible range and a band gap of 1.45 – 1.5 eV, which is found to be the optimum band gap of the absorber layer in the single junction solar cells [38]. Gallium arsenide (GaAs), Indium phosphide (InP) and Cadmium telluride (CdTe) are semiconductor materials that have band gap energies very near to the optimum value. GaAs and InP are too costly for large scale production; CdTe has toxicity problem due to Cd and Te, even though this is a very stable material. Maximum efficiency of about 25.1% was reported using GaAs (single junction) solar cells [39], whereas an efficiency of 40.7% was obtained with a triple junction GaInP/GaInAs solar cell [40]. Copper indium diselenide (CIS) and Copper indium gallium diselenide (CIGS) are the other two materials having direct band gap and very high optical absorption co-efficients. These two materials are presently being widely studied for application in solar cells, with the corresponding module technology, just reaching the stage of pilot production. CIS and CIGS are p-type semiconductors and are always used in a hetero-junction structure with very thin n-type cadmium sulphide (CdS) layer. The efficiency record obtained to date for a small size laboratory cell is 19.9% which is having only 3 μm thickness for absorber layer [41]. This is very impressive for a thin film polycrystalline solar cell. (Very recently n-type indium sulphide thin films were also used, but it is being studied in laboratory scale only).

A further degree of freedom is obtained by the partial substitution of Se_2 by S_2 [42]. This material, [$CuInS_2$] is also emerging as a promising absorber material for solar cell application [43-45]. A record efficiency of 11.4 % was reported with this material [46]. The efficiency of CIGS modules of size 30 cm x 30 cm as fabricated in pilot production line are between 9 to 12 % [47]. Recently a 59

cm x 59 cm module with 13.4% efficiency was reported [48]. One of the main advantage of solar cells based on compound semiconductor like CIS, CIGS are that they do not have the problem of light induced degradation (Stabler-Wronski effect (SWE)), in which the efficiency decreases to a stabilised but lower value after 1000 h of illumination [49]. SWE is due to the creation of new defects (dangling bonds) that act as additional recombination centres.

CdTe is the other material with a band gap of 1.45 eV which absorbs almost fully the visible light within 1 μm. A typical CdTe heterojunction solar cell structure consists of a n-Cds and p-CdTe deposited on a glass substrate coated with a transparent conducting oxide layer. The efficiency record for CdTe solar cell is 16.5% as reported by Wu et al. [50] on laboratory cell, and an efficiency of 8-9% is expected for modules.

1.6 Material for Window Layer

The n-type window layer used along with the absorber layers like CIS, CIGS and CdTe is CdS which has a wider band gap of 2.2 eV. When one goes for large scale pilot production, there will be definitely environmental hazards and safety issues related to cadmium waste (unreacted) and the by-products released as a result of the process. In addition to this, the reuse / removal of cadmium remaining the aged / old photo voltaic device is another severe problem. Due to these problems, research for other materials has already been started with the aim of replacing the CdS window layer with materials, such as In(OH, S), SnS_2, In_2S_3, ZnSe, indium selenide etc [51-53]. Major focus of these works is on developing binary compounds.

Indium selenide is one of such materials, which can be effectively used as a window layer. It is a group III-VI compound semiconductor with direct band gap of 1.8 – 2 eV (γ-In_2Se_3) [54]. This material has a tetragonal bonding

structure and crystallises in defect wurtzite structure. Since CIS and γ-In_2Se_3 have tetragonal structure with lattice parameters a=5.5 Å, c=11.13 Å and a=7.11 Å, c=19.34 Å respectively, lattice mismatch will be very much less. Recently Gordillo et al. [55] reported an efficiency of 8.3% for Mo/CIS/In_2Se_3/ZnO solar cell, with an open circuit voltage of 0.45 V and short circuit current density 30.8 mA/cm^2. This proved that indium selenide is very good substitute for CdS, even though the band gap is slightly lower when compared to CdS. On the other hand, if one has to use In_2Se_3 as the window material, the band gap has to be enhanced to get better cell characteristics as well as to allow the visible light to pass through it.

The main disadvantage of indium selenide is the co-existence of numerous phases together in a single film. This is because of the narrowness of the formation temperature for different phases of this material, which exists in different stoichiometry such as InSe, In_6Se_7, In_3Se_4 and In_2Se_3. Among these, In_2Se_3 exists in at least in five different phases α, β, γ, δ and κ depending upon the optical and structural variations. There are several publications giving large quantity of data about structural, electrical and optical properties of In_2Se_3 [56-59]; but the results are rather confusing and even contradictory, because most of the measurements are done on multi-phased films.

Taking all the facts mentioned above into account, we tried to prepare single phase indium selenide thin films. We also tried to increase the optical band gap of the material from 1.8 eV to a value above 2.2 eV (as that of CdS) without considerable variation in the electrical and structural properties. Since 1980 energetic ion beams are used for material modification. In this work, we used energetic ion beams for synthesis and modification of material properties of indium selenide thin films.

In addition to indium selenide thin films, irradiation studies were carried out on In/Sb system also. The motivation behind choosing In/sb system was that, the

mixing between metal – semimetal induced by energetic ion beams are not well studied. Again this In/sb system is deposited on Si wafer. Growth of InSb on Si is very difficult because of the lattice mismatch between InSb and Si wafers. By this study, we not only tried to prepare InSb on Si wafers but also tried to integrate InSb with Si matrix.

1.7 Materials under study

1.7.1 Indium selenide

Indium selenide is a direct band gap binary chalcogenide compound semiconductor of the III-VI group. Optical and photoelectrical properties of the material make it suitable for solar cell application. As mentioned above indium selenide exists in different stoichiometry such as InSe, In_6Se_7, In_3Se_4 and In_2Se_3. In_2Se_3 phase alone exists in five different phases α, β, γ, δ and κ respectively. α-In_2Se_3 phase crystallises in layered structure and is meta-stable at room temperature. But this phase is stable at temperatures higher than 823 K. β-In_2Se_3 phase can be obtained by heating α-In_2Se_3, which can be stabilised in room temperature (RT) by doping with Sb. The κ phase of In_2Se_3 has the same defect structure of γ phase with modification in structural vacancies. Figure 1.3 shows the phase diagram of In-Se system, in which we can see the narrowness of formation temperature of different stoichiometric In-Se compounds.

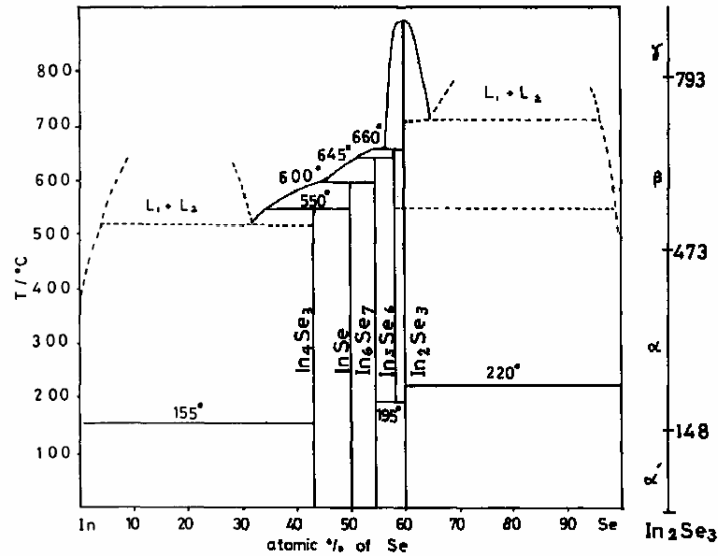

Figure 1.3: Phase diagram of In-Se system

InSe (indium mono-selenide) is a layered semiconductor with hexagonal structure (a=4.005 Å, c=16.64 Å) [60]. The layers interact with each other through Van der walls forces, while within the layer, atoms are bounded by valence forces. Because InSe has a layered structure there are no dangling bonds on the surface layer making it a potential material for hetero-junction devices. It has a direct band gap of 1.3 eV which again makes it a good absorber material in solar cells [61]. Apart from the use of indium selenide in PV application, it can be also be used for phase change random access memory (PRAM) devices [62], sensors [63] and in solid state batteries [64]. The property of In_2Se_3 to reduce the electrical resistivity, by crystallisation from amorphous phase, by an order of 10^5 makes it suitable for PRAM device application. γ- In_2Se_3 has distorted hexagonal wurtzite structure (a=7.11 Å, c=19.34 Å) in which one-third of the metal/cation sites are vacant [60, 65]. These types of semiconductors with such a structure

have the merit of being able to trap ions or molecules selectively at vacant sites and therefore, are suitable for sensors of small particles.

1.7.2 Indium antimonide

Indium antimonide (InSb) is the binary semiconductor in the III-V group having the lowest band gap. It has a band gap of 0.17eV at 300 K corresponding to infrared wavelength 6.2 μm. Another peculiarity of this material is its low effective electron mass and high mobility [66, 67]. Mobility of about 23000 to 65000 $cm^2 V^{-1} s^{-1}$ was reported for InSb films [66, 68]. InSb attracted several research groups because of the wide applications in magnetic sensors, infrared detectors as well as in infrared laser devices [69-71]. Different techniques such as molecular beam epitaxy (MBE) [66, 72], metalorganic magnetron sputtering [73], metalorganic vapour phase epitaxy [74] and vertical Bridgemen technique [70] have been used to prepare InSb films. Most of the studies were done on GaAs and bulk InSb substrates. This was to avoid the lattice mismatch problem. Recently crystalline Mn-Zn ferrite substrates were used for epitaxial growth [75]. Lattice mismatch between InSb and GaAs is only 14.6% where as with Si it is about 19%. Hence direct growth of InSb on Si substrate is very difficult and little has been reported. To reduce the lattice mismatch, thin buffer layers of fluoride [76], GaAs [68], Ge [77] and indium [76, 78] were given prior to the growth of InSb. Growing InSb on hetero-substrates (substrates other than bulk InSb) often caused defects in the epitaxial films. But the hetero-substrates opened up possibilities for new types of devices which used both the epitaxial semiconductor films and the substrates as active regions. Very few studies are performed in direct growth on Si substrates [79-81]. For device applications, amplification and signal processing are required. Usually it has been done using discrete circuits which are physically separated from the InSb sensor array. By Integrating InSb with highly advanced Si circuitry, one could get significant gain in terms of reliability and speed. Moreover, high density of integration will allow considerable cost savings in the manufacturing process. However, direct

growth of InSb on the Si substrate is very difficult, because of large lattice mismatch [over 19%] and different thermal expansion co-efficient. Recently significant advance in InSb devices has been achieved and developed large area InSb focal plane arrays on Si substrates [82, 83]. In the present study we tried to integrate InSb with Si substrate using ion beam mixing.

1.8 Thin Film Preparation Techniques

A thin film is defined as low-dimensional material created by condensing atomic/molecular/ionic species of matter, in a controlled manner. Thin films have been extensively used in physical research and device fabrications [84].Basic properties of thin films such as composition, crystal phase and orientation, film thickness and microstructure are controlled by deposition conditions. A wide variety of microstructures and consequently properties can be obtained by simply varying the deposition conditions during the growth of the film. Thin film properties are also strongly dependent on substrate materials, substrate temperature, rate of deposition and background pressure. Application and the properties of the given material determine the most suitable technique for the preparation of thin films of that material.

The thin films prepared for the studies presented in this thesis were mainly deposited using a combination of chemical bath technique and vacuum evaporation. Indium selenide thin films were prepared by annealing In/Se bilayer systems at 100 to 400°C, in which Se layer was deposited using chemical bath deposition [CBD] technique. Indium layer was then deposited over this, using vacuum evaporation technique (resistive heating). Indium antimonide was prepared by ion beam irradiation of In/Sb bilayers. Here, In was deposited using resistive heating and Sb by electron beam evaporation.

Generally any thin film deposition involves the following steps: a source material is converted into the vapour form (atomic/molecular/ionic species) from

the condensed phase (solid or liquid), which is transported to the substrate and then it is allowed to condense on the substrate surface to form the solid film [85]. Depending on how the atoms/molecules/ions/clusters of species are created for the condensation process, the deposition techniques are broadly classified into two categories, viz. physical methods and chemical methods.

Chemical bath deposition, chemical vapour deposition, and spray pyrolysis are examples of chemical method of thin film deposition. Thermal evaporation, electron beam evaporation, rf and dc sputtering and pulsed laser deposition (PLD) are examples of physical methods of thin film preparation.

1.8.1 Chemical bath deposition technique

Chemical bath deposition [CBD] or solution deposition technique is one of the simplest and cost effective techniques for preparing thin films of elemental and compound materials. The experimental set-up consists of a beaker containing the solution of the salt which is to be deposited and a substrate dipped in it. The process is carried out in atmospheric pressure and relatively low temperature. An aqueous solution of a metal complex, when mixed with a solution of chalcogen bearing compound, precipitation of the chalcogenide occurs under certain conditions. When precipitation is controlled, the compound gets deposited on clean substrate or other nucleating centres, present in the solution. In the present work, this technique was made use of to deposit Selenium film.

According to solubility product principle, in a saturated solution of a weakly soluble compound, the product of molar concentrations of its ions called the ionic product is a constant at a given temperature. Precipitation of solid phase occurs due to super saturation of the reaction bath. At a given temperature, when the ionic product exceeds the solubility product, precipitation occurs. Otherwise the solid phase produced will dissolve back into the solution resulting in no net precipitation. In a typical CBD set up, substrates are immersed in a solution

containing the cations and anions and controlled precipitation leads to formation of thin films.

There are two possibilities for thin film deposition in CBD. One is the 'ion-ion process' in which the ions condense on the substrate surface to form the film. The other is the 'cluster by cluster process' in which colloidal particles of the compound formed in the solution gets adsorbed at the substrate surface to form thin layers. There are many factors, which influence the deposition process viz. nature of reactants, temperature, pH value and concentration of ions, nature of the substrate and duration of reaction.

(a) Selenium film deposition

For selenium film deposition a stock solution of 0.1 M Sodium Selenosulphate (Na_2SeSO_3) was prepared by adding Se powder to aqueous solution of excess sodium sulphite (Na_2SO_3) kept at 100°C with constant stirring. This solution should be kept at 100°C for at least 3 h with constant stirring to obtain clear solution of sodium selenosulphate solution. The pH of the stock solution is kept at a value of ~ 10. It was found out by Keith et al. [86] and Bindu et al. [87] that at pH ≥ 10, the Na_2SeSo_3 solution was stable. The chemical reaction taking place can be written as;

$$Se + Na_2SO_3 \Leftrightarrow Na_2SeSO_3 \qquad (1.1)$$

This solution is made to 0.025 M by adding distilled water. In order to trigger the precipitation, dilute acetic acid was added to maintain the pH of the solution between 4.2 and 4.7. The substrates were kept in the solution facing the walls of the beaker. Uniform red-brown coloured Se films were obtained after ~6 hours. We could control the thickness of the film by increasing the duration of time the substrates kept in the solution. Figure 1.4 shows the experimental set-up of CBD technique.

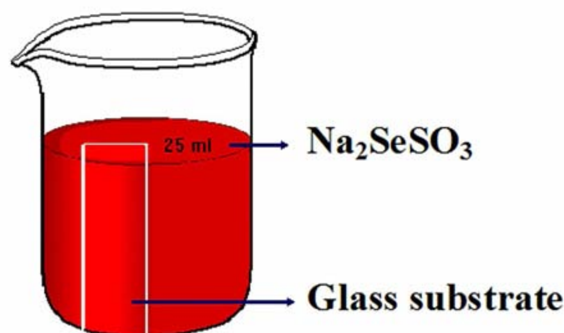

Figure 1.4: Showing the set-up of chemical bath deposition of Se film.

The growth condition and optimisation of Se film was done in our laboratory earlier by Bindu et al. and reported elsewhere [87-89].

1.8.2 Thermal evaporation by resistive heating

Thermal evaporation is the most widely used technique for the preparation of thin films of metals, alloys, and also many compounds. A vacuum environment, in which sufficient amount of heat is given to the evaporants to attain the vapour pressure necessary for the evaporation, is the only requirement for this technique. Evaporated material is allowed to condense on a substrate kept at a suitable temperature.

When evaporation is made in vacuum, the evaporation temperature will be considerably lowered and the formation of the oxides and incorporation of impurities in the growing layer will be reduced. Evaporation is normally done at a pressure of 10^{-5} Torr. At this pressure, a straight line path for most of the emitted vapour atoms is ensured for a substrate to source distance of nearly 10 to 50 cm [90]. Characteristics and quality of the deposited film will depend on substrate temperature, rate of deposition, ambient pressure, etc. Uniformity of the film depends on the geometry of the evaporation source and its distance from

the source. Deposition by thermal evaporation is simple, convenient and is widely used [91]. Thermal evaporation by resistive heating has been used for the deposition of indium layer in the present study.

1.8.3 Electron beam evaporation

In electron beam (e-beam) evaporation a stream of electrons is accelerated through fields of typically 5–10kV and focussed onto the surface of the material for evaporation. The electrons lose their energy very rapidly upon striking the surface and the material melts at the surface and then evaporates. That is, the surface is directly heated by impinging electrons, in contrast to conventional heating modes. Direct heating allows the evaporation of materials from water-cooled crucibles, which are necessary for evaporating reactive and in particular, reactive refractory materials, to avoid almost completely the reactions with crucible walls. This allows the preparation of high purity films because crucible materials or their reaction products are practically excluded from evaporation [91, 92].

Electron beam guns can be classified into thermionic and plasma electron categories. In the former type, the electrons are generated thermionically from heated refractory metal filaments, rods or disks. In the latter type, the electron beams are extracted from plasma confined in a small space.

In the present study, antimony (for the preparation of InSb) was evaporated using e-beam evaporation technique using a 3 kW electron beam source and a six-inch diameter diffusion pump backed by a rotary pump.

1.9 Characterisation Techniques

Optimisation of the preparation conditions to obtain films with required properties is the main task in research. This has to be carried out on the basis of detailed structural, optical and electrical properties of the films obtained at different growth conditions. In the following sections the techniques used for the film characterizations are discussed briefly.

1.9.1 Thin film thickness

Thickness plays an important role in the film properties unlike a bulk material. Reproducible properties are achieved only when the film thickness and the deposition parameters are kept constant. Film thickness may be measured either by in-situ monitoring of the rate of deposition or after the film deposition. In the present work, thicknesses of the thin films were measured by a stylus profiler (Dektak 6M).

Stylus profiler is an advanced technique for measuring thickness both thin and thick films. It is capable of measuring steps even below $100\acute{A}$. This instrument can also be used to profile surface topography and waviness, as well as, measuring surface roughness in the sub nanometer range. The instrument takes measurements electro-mechanically by moving the sample beneath a diamond-tipped stylus. The high precision stage moves the sample beneath the stylus according to a user-programmed scan length, speed and stylus force. The stylus is mechanically coupled to the core of an LVDT (Linear Variable Differential Transformer). As the stage moves the sample, the stylus rides over the sample surface. Surface variations cause the stylus to be translated vertically. Electrical signals corresponding to stylus movement are produced as the core position of the LVDT changes. The LVDT scales an AC reference signal proportional to the position change, which in turn, is amplified and converted to a digital format through a high precision, integrating, analog-to-digital converter. The film

whose thickness has to be measured is deposited with a masked region to create a step on the sample surface. Thickness of the sample can be measured accurately by measuring the vertical motion of the stylus over the step.

1.9.2 X-ray diffraction studies

Electrical and optical properties of the thin films grown are mainly influenced by the crystallographic nature of the films. X-ray diffraction (XRD) studies were carried out to study the crystallographic properties of the thin films prepared.

The basic law involved in the XRD technique is the Bragg's law. When monochromatic x-rays impinge upon the atoms in a crystal lattice, each atom acts as a source of scattering. The crystal lattice acts as series of parallel reflecting planes. The intensity of the reflected beam at certain angles will be maximum when the path difference between two reflected waves from two different planes is an integral multiple of λ. This condition is called Bragg's law and is given by the relation [93],

$$2dSin\theta = n\lambda \qquad (1.2)$$

Where n is the order of diffraction, λ is the wavelength of the x-rays, d is the spacing between consecutive parallel planes and θ is the glancing angle. Figure 1.6 shows the Bragg's reflection of X-rays from atomic layers.

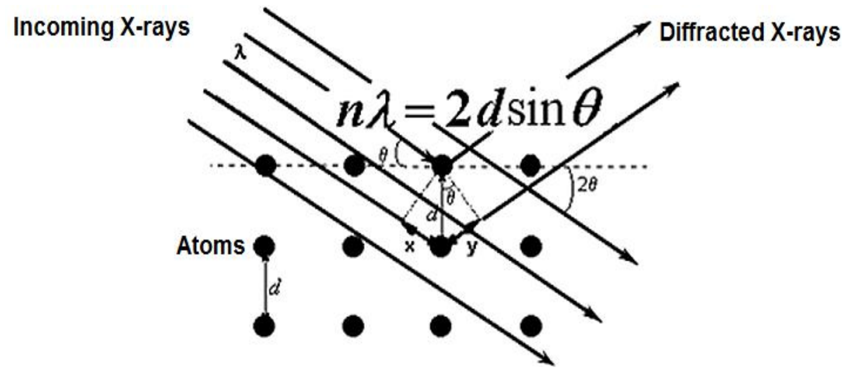

Figure 1.5: Showing X-ray diffracted from the atomic layers obeying Bragg's law.

XRD studies give a whole range of information about the crystal structure, grain orientation, average crystalline size and stress in the films. Experimentally obtained diffraction patterns of the sample are compared with the standard powder diffraction files published by joint council for powder diffraction studies (JCPDS) or the International Centre for Diffraction Data (ICDD).

The average grain size of the film can be calculated using the Debye Scherrer's formula [93],

$$d = \frac{0.9\lambda}{\beta \cos\theta} \tag{1.3}$$

Where, λ is the wavelength of the x-ray (Cu k_{α} line with λ=1.5405 Å) and β [in radians] is the full width at half maximum of the peak with maximum intensity.

The lattice parameter values for different crystallographic systems can be calculated from the following equations using the (hkl) parameters and the inter-planar spacing d.

Cubic system, $$\frac{1}{d^2} = \frac{h^2 + k^2 + l^2}{a^2} \tag{1.4}$$

Tetragonal system, $$\frac{1}{d^2}=\frac{h^2+k^2}{a^2}+\frac{l^2}{c^2} \qquad (1.5)$$

Hexagonal system, $$\frac{1}{d^2}=\frac{4}{3}\left(\frac{h^2+hk+k^2}{a^2}\right)+\frac{l^2}{c^2} \qquad (1.6)$$

XRD measurements of the films in the present studies were carried out using Philips X-pert Pro. X-ray diffractometer.

1.9.3 Optical characterisation

(a) Determination of band gap energy

Intrinsic optical absorption of a single photon across the band gap is the dominant optical absorption process in a semiconductor. When the energy of the incident photon (hν) is larger than the band gap energy, the excitation of electrons from the valence band to the empty states of the conduction band occurs. Light passing through the material is then absorbed and the number of electron-hole pairs generated depends on the number of incident photons $S_0(\nu)$ per unit area, per unit time, per unit energy. Frequency, [ν] is related to wavelength [λ] through the relation, $\lambda = c/\nu$, where c is the velocity of light. Photon flux S(x,ν) decreases exponentially inside the crystal according to the relation [68],

$$S(x,\nu)=S_o(\nu)*e^{-\alpha x} \qquad (1.7)$$

Where α is the absorption coefficient of the material, given by α=4πkυ/c, where k is the extinction coefficient. The absorption coefficient can be deduced from the absorption spectra using the relation,

$$I=I_0e^{-\alpha t} \qquad (1.8)$$

Where, I is the transmitted intensity and I_0 is the incident intensity of the light and t is the thickness of the film. For the parabolic band structure, the relation between absorption coefficient and band gap of the material is given by [94, 95],

$$\alpha = \frac{A}{h\upsilon}\left(h\upsilon - E_g\right)^r \qquad (1.9)$$

ie $$(\alpha h\nu)^{1/r} = A\left(h\nu - E_g\right) \qquad (1.10)$$

Where E_g is the band gap of the material, r is the index equal to 1/2, 2, 3 and 3/2 for allowed direct transitions, allowed indirect transitions, forbidden indirect transitions and forbidden direct transitions respectively. 'A' is the parameter which depends on the transition probability. In the case of direct band gap material, r = 1/2.

Then equation 1.10 becomes,

$$(\alpha h\nu)^2 = A\left(h\nu - E_g\right) \qquad (1.11)$$

at α =0, $$E_g = h\nu \qquad (1.12)$$

Thus we can obtain the optical band gap of a material by extrapolating the straight line portion of $(\alpha h\nu)^2$ versus $h\upsilon$ plot to α=0. In the present study, optical absorption spectra were recorded with the help of UV-VIS-NIR spectrophotometer (model: Hitachi U-3410).

(b) Photoluminescence

Luminescence in solids is the phenomenon in which [valence] electronic in solids are excited by optical energy from an external source and the excited electrons de excite releasing the energy as light. These excited charge carriers return to ground state through radiative or non-radiative transitions, by emitting photons or by emitting heat via phonon interaction respectively. The phenomenon of de-excitation of charge via photon emission is called photoluminescence [96]. There are mainly two types of Photoluminescence (PL): Intrinsic and extrinsic photoluminescence, depending on the nature of electronic transition producing it.

(i) Intrinsic luminescence

Intrinsic luminescence is again classified into three; band-to-band, exciton and cross-luminescence.

Band –to –band luminescence: Luminescence owing to the band-to-band transition, ie through the recombination of an electron in the conduction band with a hole in the valance band, can be seen in pure crystal at relatively high temperature. This has been observed in Si, Ge and IIIb-Vb compounds such as GaAs.

Exciton luminescence: An exciton is a composite particle of an excited electron and a hole, interacting with one another. It moves in a crystal conveying energy and produces luminescence owing to the recombination of the electron and the hole. There are two kinds of excitons: Wannier exciton and Frenkel exciton.
The Wannier exciton model describes an exciton composed of an electron in the conduction band and a hole in the valence band bound together by coulomb interaction. Wave function of the electron and hole in Wannier exciton is much larger than the lattice constant. Excitons in IIIb-Vb and IIb-VIb compounds are examples for Wannier exciton. Frenkel exciton model is used in cases where electron and hole wave functions are smaller than lattice constant. The excitons in organic molecular crystals are examples of Frenkel exciton.

Cross luminescence: Cross luminescence is produced by the recombination of an electron in the valance band with a hole created in the outer most core band. This is observed in number of alkali and alkaline-earth halides and double halides. This takes place only when the energy difference between the top of valance band and that of conduction band is smaller than the band gap energy. This type of luminescence was first observed in BaF_2.

(ii) Extrinsic luminescence

Luminescence caused by intentionally incorporated impurities, mostly metallic impurities or defects, is classified as extrinsic luminescence. Most of the observed type of luminescence of practical application belongs to this category. Intentionally incorporated impurities are 'activators' and materials made luminescent in this way are called 'phosphors'.
Extrinsic luminescence in ionic crystals and semiconductors is classified into two types: unlocalized and localized. In the former type, the electrons and holes of the host lattice participate in the luminescence process, while in localized type the luminescence excitation and emission process are confined in a localized luminescence centre.

Unlocalised type: In semiconductors donors and accepters act as luminescence activators. There are two types of luminescence transitions i.e. the transition of a free carrier to a bound carrier and the transition of a bound electron at a donor to a bound hole at an acceptor. These kinds of luminescence lines and bands are usually observed in compound semiconductors.
Localised type: Various kinds of metallic impurities intentionally incorporated in ionic crystals and semiconductors create efficient localized luminescence centres.

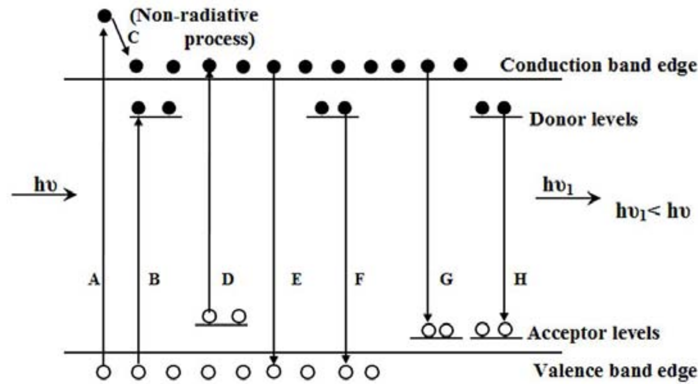

Figure 1.6: Different luminescence processes in solids. Process 'A'- Carrier excitation with energy hυ, 'B' and 'D'- extrinsic absorption to and from defects, 'C'- non-radiative transition, 'E', 'F', 'G' and 'H' represents the radiative band-to-band, bound to free, free to bound and donor to acceptor transitions respectively.

Photoluminescence is one of the non-destructive and precision techniques used to detect defects in semiconductor materials. It is also used to study biological samples, to detect cancerous tissues etc. Without defects, semiconductors are useless. But it is very essential to control and detect the defects in materials. PL is a simple and contact less technique useful for this purpose. This can be made to scan over the sample surface to analyse the uniformity of sample. When semiconductor materials are irradiated with photons with energy higher than its band gap, excitation of charge carriers to higher energy takes place by absorbing the photon. These excited charge carriers return to ground state by radiative or non-radiative transitions, i.e., by emitting photons or by emitting heat via phonon interaction respectively. Figure 1.6 shows the schematic representation of different transitions in solids.

The main components of PL set-up are monochromatic light source, normally a laser with energy higher than the band gap of the material, a detector to detect

the emitted luminescence from the sample and lenses for focussing. Intensity and spectral content of this PL emission help in the direct measurement of various important material properties. In the present study PL is used to determine the defect levels in the samples. It is particularly suited for the detection of shallow level impurities, but can be applied to certain deep level impurities provided their recombination is radiative.

For low temperature PL measurements, samples were placed inside a cryostat and cooled to temperatures near liquid Helium. Low temperature PL measurements are necessary to obtain the spectroscopic information by minimizing thermally activated non-radiative recombination processes and thermal line broadening. Thermal distribution of carriers excited into a band contributes a width of approximately kT/2 to an emission line originating from that band (where k is the Boltzman constant and T, temperature in kelvin). This makes it necessary to cool the sample to reduce the width. The thermal energy kT/2 is only 0.18meV at T=4.2 K.

In the present work, PL measurements were carried out in the temperature range 12 to 300 K with a closed cycle liquid Helium cryostat (Janis Research Inc.). The temperature was maintained with an accuracy of $\pm$ 1 K using a temperature controller (Lake Shore Model 321). The 632.8 nm line of a He-Ne laser (5 mW, Melles Griot) was used as the excitation source. The laser beam was focused onto the samples with a beam diameter of 1mm. Emission spectra were analyzed using spectrophotometer (Ocean optics NIR 512) having a InGaAs linear array detector.

1.9.4 Electrical characterization

(a)Sheet resistance

Resistivity of a semiconductor material is largely influenced by different factors such as lattice vibrations, impurity concentration, crystallinity, strain, displaced

atoms in the lattice, grain boundaries etc. Resistivity, ρ of a specimen with rectangular shape can be expressed as,

$$R = \frac{\rho l}{bt} \qquad (1.13)$$

Where 'R' is the resistance, 'l' the length, 'b' the breadth and 't' the thickness of the specimen. Resistivity of a bulk material is constant unlike thin films which are thickness dependent. Hence for thin films, we can express the resistance of the film as sheet resistance, given by

$$R_s = \frac{\rho}{t} = \frac{Rb}{l} \qquad (1.14)$$

Where 'b' is the length of the electrode and 'l' the distance between the electrode. In the present study for measuring the sheet resistance two electrodes were drawn 0.5 cm apart using silver paste with a length of 0.5 cm. Two probes from source measuring unit (digital multimeter) were connected to the silver electrodes using magnanin wires as pressure contacts. Voltage in the range 0-5 V was applied and corresponding current was measured with the kelp of a computer which is interfaced with the source measuring unit (SMU-123X, KEITHLY).

(b) Photosensitivity

Photosensitivity of a semiconductor material is defined as the measure of the minority carriers generated in the material under illumination, and is expressed as the ratio of difference between the dark current (I_d) and photocurrent (I_l) to the dark current.

$$S = \frac{I_l - I_d}{I_d} \qquad (1.15)$$

Samples were illuminated using a tungsten halogen lamp of intensity 100 mW/ cm^2 for 60 s prior to photoconductivity measurement.

(c) Conductivity type

Conductivity type of a semiconductor material can be determined by hot or thermoelectric probe method. This technique employs the 'Seebeck effect' to determine the type of conductivity. The sign of the thermal emf or Seebeck voltage generated by the temperature gradient tells whether the material has n-type or p-type conductivity. In this method two probes are kept in contact with the sample surface, with one hot and the other cold. Thermal gradients produce currents in a semiconductor, the majority carrier currents for n and p-type materials are given by,

$$J_n = -qn\mu_n P_n \frac{dT}{dx} \tag{1.16}$$

$$J_p = -qp\mu_p P_p \frac{dT}{dx} \tag{1.17}$$

Where q is the charge, n and p are the number of electrons and holes, μ the mobility of the charge carriers, $\frac{dT}{dx}$ the temperature gradient, $P_n < 0$ and $P_n >$ 0 are the differential thermoelectric power.

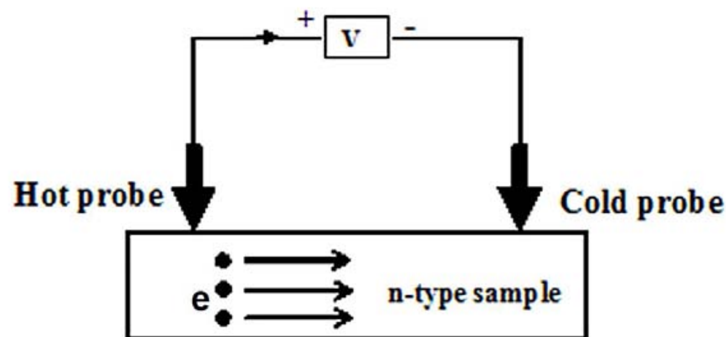

Fig 1.7: Schematic representation of hot probe technique.

In fig 2.4, $\frac{dT}{dx} > 0$, and the electron current in an n-type sample flows from left to right. The thermoelectric power can be thought of as a current generator. A part of the current flows through the voltmeter causing the hot probe to develop positive potential with respect to the cold probe. Electrons diffuse from the hot to the cold region setting up an electric field that opposes diffusion. The electric field produces a potential detected by the voltmeter with the hot probe positive with respect to the cold probe. Analogous reasoning leads to the opposite potential for p-type samples [97].

1.9.5 X-ray Photoelectron Spectroscopy (XPS)

X-ray Photoelectron Spectroscopy (XPS), earlier known as Electron Spectroscopy for Chemical Analysis (ESCA), is pioneer tool for the determination of chemical state and quantitative atomic composition of the materials [97]. It is basically a surface analysis technique which can give chemical and compositional information up to ~ 50 to 70 Å. This technique is mainly used to detect compound formation and to distinguish the chemical state of the elements, such as whether the element is exist in sulphate or as sulfide state in a compound.

In XPS technique, high energy monochromatic X-ray photons are used to irradiate the specimen under study. This results in the emission of inner core electrons from the specimen. Kinetic energy E_k, of these core electrons were measured using an spectrometer/ energy analyzer. Then the binding energy E_b, of the core electron can be given as [98],

$$E_b = h\nu - E_k - \varphi \qquad (1.18)$$

Where $h\nu$ is the energy of the X-ray and φ the work function of the spectrometer. Energy of the ejected electrons gives the signature/ characteristics

of the atoms and their chemical environment. Binding energy of the core electron is affected by the valence electron and therefore by the chemical environment of the atoms. When the chemical environment of the atoms changes, it will change the local charge surroundings of the atom. This change reflects as the variation in binding energy. Hence the change in the binding energy can give information about the valence state/ compound formation of the atom in the sample. This will help to find out whether the element present in the sample is in pure or in compound form. In the present study X-ray Photo electron spectra were recorded using ULVAC-PHI Unit (model: ESCA-5600CIM). To obtain the depth-wise information, outer layers of the samples were sputtered using 200 keV Ar ions and XPS spectra was recorded.

1.9.6 Atomic Force Microscopy (AFM)

Following the invention of the scanning tunnelling microscope, a number of new scanning probe microscopes (SPM) were developed that used the key components of the scanning tunnelling microscope. One of the most important SPM is the atomic force microscope [AFM] which is used for the surface morphological study [99]. AFM operates by measuring the forces between a probe and the sample. These forces depend on the nature of the sample, the distance between probe and the sample, the probe geometry and the sample surface contamination. The main parts of the AFM nanoscope are a diode laser, photo detector, piezo-elecctric transducer and an AFM tip, normally made of Si_3N_4 attached to the end of a spring cantilever, which are interfaced with a computer. In AFM, a sharp tip is scanned over a surface of the sample with feedback mechanisms that enable the piezo-electric scanners to maintain the tip at a constant force or height above the sample surface. The nanoscope employs an optical detection system in which the tip is attached to the underside of a reflective cantilever. A diode laser is focused onto the back of a reflective cantilever. As the tip scans the surface of the sample, moving up and down obeying the contour of the surface, the laser beam is deflected off the attached

cantilever into a dual element photodiode. The photo detector measures the difference in light intensities between the upper and lower photo detectors, and then converts to voltage. Feedback from the photodiode, through software control from the computer, enables the tip to maintain either a constant force or constant height above the sample. In the constant force mode the piezo-electric transducer monitors real time height deviation. In the constant height mode, the deflection force on the sample is recorded. The latter mode of operation requires calibration parameters of the scanning tip to be inserted in the AFM head during force calibration of the microscope. In the present work, AFM-Nanoscope-E, Digital Instruments, was used for the measurements. The measurements were taken in contact mode.

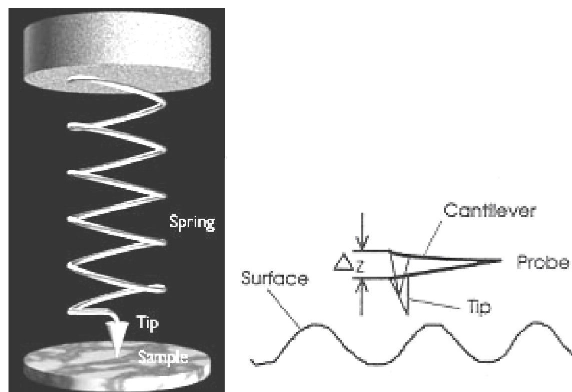

Figure 1.8: The essential elements of an AFM

An AFM images a surface in a manner analogous to the gramophone stylus sensing the groves of gramophone disk. The essential elements of an AFM are shown in the figure 1.8. The tip is attached to a cantilever type spring as shown in the figure. As the tip and sample interact, forces act on the tip and cause the

cantilever (spring) to deflect. The cantilever position is monitored by a position detector. The output of the detector is connected to a feedback controller that regulates the force between the sample and the tip by moving the sample up or down. The amount of deflection is proportional to the force acting on the tip.

$$F_{spring} = -k.\Delta Z \qquad (1.19)$$

Where k is the spring constant of the cantilever and ΔZ is the deflection of the cantilever.

Various modes of AFM measurements include contact mode, dynamic force mode, phase mode, friction force microscope, magnetic force microscope, surface potential microscope, etc are scanning probes microscopes slight variation in the working principles from that described above.

1.9.7 Rutherford Backscattering technique

Rutherford backscattering spectroscopy (RBS) is one of the ion beam assisted characterization technique for material identification and ion beam mixing study. It can also provide information about the composition of multi-elemental samples, thickness of thin films, depth-profile of elements and can be used to identify unknown elements in the material [100]. In RBS analysis, a collimated beam of energetic ions, usually 2-3 MeV He or H ions, are allowed to impinge on the sample at off normal incidence. Backscattered ions from the sample are usually detected with the help of particle detector. The signal is further amplified, shaped and finally analysed using a multi-channel analyser, to obtain RBS spectra. The principle and geometry of RBS is explained in chapter 4, section 4.2.

Reference

1. D.K. Avasthi, Current Science **78** (2002) No: 11, 1297
2. S. Kraft, B. Schattat, and W. Bolse, J. Appl. Phys. **91** (2002) 1129
3. G. Schiwietz, E. Luderee, G. Xiao, P. L. Grande, Nucl. Instrum. Methods B **175** (2001) 1
4. R. L. Fleisher, P. B. Price, R. M. Walker, Nuclear Tracks in Solids, University of California Press, 1975
5. A. Akkermann, J. Levinson, D. Ilberg, Y. Lifshitz, Editor - R. Baragiola, Ionisation of Solids by Heavy Particles, NATO Advanced Study Institutes Series 306, Plenum Press, New York, 1992, p. 431
6. Wolfgang Bolse, Surface and Coatings Technology **158** (2002) 1.
7. F. Seitz, J. S. Koehler, Solid State Phys. **2** (1956) 305
8. Z. G. Wang, Ch. Dufour, E. Paumier, M. Toulemonde, J. Phys.: Condens. Matter **6** (1994) 6733
9. B. Schattat and W. Bolse, Nucl. Instrum. Methods. Phys. Res. B **225**, (2004) 105.
10. P. Sathyavathi, S. T. Chavan, D. Kanjilal and V. N. Bhoraskar, Nucl. Instrum. Methods. Phys. Res. B **156**, (1999) 72.
11. D. C. Ingram and A. W. McCormick, Nucl. Instrum. Methods. Phys. Res. B **34**, (1988) 68.
12. A. Benyagoub, F. Couvreur, S. Bouffard, F. Levesque, C. Dufour and E. Paumier, Nucl. Instrum. Methods. Phys. Res. B **175**, (2001) 417.
13. C. Gilbert- Mougel, F. Couvreur, J. M. Costantini, S. Bouffard, F. Levesque, S. Hemon, E. Paumier and C. Dufour, J. Nucl. Mater. **295**, (2001) 121.
14. S. Nakao, K. Saitosh, M. Ikeyama, H. Niwa, S. Tanemura, Y. Miyagawa and S. Miyagawa, Thin Solid Films **281**, (1996) 10.
15. S. Balamurugan, B. R. Mehta, D. K. Avasthi, F. Singh, Akhilesh. K. Arora, M. Rajalakshmi, G. Raghavan, A. K. Tyagi and S. M. Shivaprasad, J. Appl. Phys. **92**, (2002) 3304.

16. M. S. Kamboj, G. Kaur, R. Thangaraj and D. K. Avasthi, J. Phys. D; Appl. Phys. **35**, (2002) 477.
17. P. Shah, S. Kumar, A. Gupta and D. K. Avasthi, Nucl. Instrum. Methods. Phys. Res. B **156**, (1999) 222.
18. Wolfgang Bolse, Beate Schattat Nucl. Instr. and Meth. B **190** (2002) 173.
19. M. Levalois and P. Marie, Nucl. Instr. and Meth. B **156** (1999) 64
20. Ch. Dufour, A. Audouard, F. Beuneu, J. Dural, J. P. Girard, A. Hairie, M. Levalois, E. Paumier, and M. Toulemonde, J. Phys.: Condens. Matter **5**, 4573 (1993)
21. R. Sreekumar, R. Jayakrishnan, C. Sudha Kartha, K.P. Vijayakumar, S. A. Khan, D. K. Avasthi. J. Appl. Phys. **103** (2008) 023709.
22. S. O. Kucheyev, J. S. Williams, C. Jagadish, J. Zou, C. Evans, A. J. Nelson, A. V. Hamza, Phys. Rev. B **67** (2003) 94115
23. Sankar Kumar and V. N. Kulkarni, Thin Solid Films **333** (1998) 20
24. Sarvesh Kumar, R. S. Chauhan, R. P. Singh, W. Bolse and D. K. Avasthi et al. Nucl. Instr. and Meth. B **212** (2003) 242
25. W. Bolse, Nucl. Instrum. Methods B **141** (1998) 133
26. W. Bolse, Nucl. Instrum. Methods B **148** (1999) 83
27. W. Bolse, Surface Coatings and Technology **158-159** (2002) 1
28. P. Sigmund, Rev. Roumaine Phys. **17** (1972) 823
29. P. Sigmund, A. Gras-Marti, Nucl. Instrum. Methods **182-183** (1981) 25
30. C. Dufour, Ph. Bauer, G. Marchal, J. Grilhe, C. Jaouen, J. Pacaud and J. C. Jousset, Europhys. Lett. **21**(6) (1993) 671
31. D.K. Avasthi, W. Assmann, H. Nolte and H.D. Mieskes, Nucl. Instr. and Meth. B **156** (1999) 143
32. Ajay Gupta, Suneel Pandita, D. K. Avasthi, G. S. Lodha and R. V. Nandedkar, Nucl. Instr. and Meth. B **146** (1998) 265
33. R. Lagnay, A. Dunlop, F. Dunstter and N. Lorenzelli, Nucl. Instr. and Meth. B **106** (1995) 28

34. Alejandro Crespo-Sosa, Manuel Munoz and Juan-Carlos Cheang-Wong, Materls. Sci. and Eng. B **100** (2003) 297

35. S. K. Srivastava, D. Kabiraj, B. Schattat, H. D. Carstanjen and D. K. Avasthi, Nucl. Instr. and Meth. B **219** (2004) 815

36. Martin A. Green, Keith Emry, Yoshihiro Hishikawa, Wilhelm Warta, Prog. Photovolt: Res. Appl. **16** (2008) 435

37. http://www.amonix.com/solar_efficiency_world_record.html.

38. S. M. Sze, Physics of Semiconductor Devices, Wiley and Sons, New York (1981) p-798

39. Martin A. Green, Keith Emry, D. L. King, S. Igari, W. Werta, Prog. Photovolt., Res. Appl. **13** (2005) 387

40. R. R. King, D. C. Law, K. M. Edmondson, C. M. Fetzer, G. S. Kinsey, H. Yoon, R. A. Sherif, N. H. Karam, Appl. Phys. Lett. **90** (2007) 183516

41. M. A. Contreras, K. Ramanathan, J. Abu Sharma, F. Hasoon, D. L. Young, B. Egaas, R. Noufi, Prog. Photovolt. Res. Appl. **13** (2005) 209.

42. T. M. Friedelmeier and H. W. Schock, in Proceedings of the 2nd World Conference on PV Solar Energy Conversion, J. Schmid *et al.*, Eds. 1998, pp. 1117 - 1120.

43. Y. Ogawa, A. J. Waldan, Y. Hashimoto and K. Ito, Jpn. J. Appl. Phys. **33** (1994) L1775

44. S. Uenishi, K. Tohyama and K. Ito, Sol. Energy Mater. Sol. Cells **35** (1994) 231

45. Y. Onuma, K. Takeuchi, S. Ichikawa, m. Harada, H. Tanaka, A. koizumi and Y. Miyajima, Sol. Energy Mater. Sol. Cells **69** (2001) 261

46. N. Meyer, A. Meeder, D. Schmid, Thin Solid Films **515** (2007) 5979.

47. B. Dimmler *et al.*, in Proceedings of the 2nd World Conference on PV Solar Energy Conversion, J. Schmid *et al.*, Eds. 1998, pp. 419-423.

48. Proceedings of 22nd EU Photovoltaic Solar Energy Conference, Milano, Italy (2007)

49. D. L. Staebler and C. R. Wronski, ibid. **31** (1977) 292

50. X. Wu, J. C. Keene, R. G. Dhere, C. De Hart, D. S. Albin, A. Duda, T. A. Gessert, S. Asher, D. H. Levi, P. Sheldon, Proceedings of the 17th European PVSEC (2001) p.995
51. Teny Theresa John, S. Bini, C. Sudha Kartha, K. P. Vijayakumar, T. Abe and Y. Kashiwaba and Y. Yasuhiro, Semicond. Sci. Technol. **18** (2003) 491
52. J. George, C. K. Valsala Kumari, J. Crystal Growth **63** (1983) 233
53. S.T. Lakshmikumar and A.C. Rastogi, Sol. Energy Mater. Sol. Cells **32** (1994) 7
54. C. Julien, A. Cheavy and D. Siapkas. Phys. Status Solidi A **118** (1990) 553
55. G. Gordillo and C. Calderon. Sol. Energy Mater. Sol. Cells **77** (2003) 16321
56. C. Amory, J.C. Bernede and S. Marsillac, J.Appl. Phys. **94** (2003) 6945
57. D. Eddike, A. Ramdani, G. Brun, J.C. Tedenae and B. Leautard, Mater. Res. Bull. **33** (1998) 519.
58. J. Ye, S. Soeda, Y. Nakamura and D. Nittono, Jap. J. Appl. Phys. (Part 1) **37** (1998) 4264.
59. C. H. de. Groot and J.S. Moodera, J. Appl. Phys. **89** (2001) 4336
60. S. Popovic, A. Tonbic, B. Grezetta-Plenkovic, B. Celustka and R. Trioko, J. Appl. Crystallogr. **12** (1979) 416.
61. J. V. Mc Canny and R. B. Murray, J. Phys. C **10** (1979) 1211.
62. Heon Lee, Dae Hwan Kang and Lung Tran, Material Science and Engineering B **119** (2003) 196
63. M. Yudasaka, T. Matsuoka and K. Nakanishi, Thin Solid Films **146** (1987) 65
64. P. Gomes da Costa, M. Balkanski and R. F. Wallis, Phys. Rev. B **43** (1991) 7066.
65. A. Likforman and D. Carre, Acta Crystallogr. Sect. B **34** (1978) 1.
66. B.V. Rao, D. Gruznev, T. Tambo and C. Tatsuyama, Semicon. Sci. Technol. **16** (2001) 216
67. Stradling. R. A, Braz. J. Phys. **26** (1996) 7
68. J. I. Chyi, D. Biswas, S. V. Iyer, N. S. Kumar, H. Morkox, R. Bean, K. Zanio, R. Grober and D. Drew, J. Vac. Sci. Technol. B **7** (1989) 345.
69. Gert Finger, Reinhold J. Dorn, Manfred Meyer, Leander Mehrgan, Jorg Stegmeier and Alan Moorwood, Nucl. Instr. and Meth A. **549** (2005) 79

70. Atsushi Okamoto, Takashi Yoshida, Shogo Muramatsn and Ichiro Shibasaki, J. Crystal Growth **201** (1999) 765
71. Ozer. S and Besikci, J. Phys. D : Appl. Phys. **36** (2003) 559
72. Orias. G, Hoffman A. W and Casselman M. F, SPIE J. **627** (1986) 408
73. Webb. J. B and Halpren. C, Appl. Phys. Lett. **47** (1985) 831
74. Chang. P. K and Bedair S. M, Appl. Phys. Lett. **46** (1985) 383
75. H. Fujioka, T. Ikeda, K. Ono, S. Ito, M. Oshima, Journal of crystal Growth **241** (2002) 309.
76. W. K. Liu, J. winesette, Weilman Ma, Xuemei Zhang, M. B. Santos, X. M. Fang and P. J. Mc Cann, J. Appl. Phys. **81** (1997) 1708.
77. M. Mori, Y. Tsubosaki, T. Tambo, H. ueba and C. Tatsuyama, Appl. Surf. Sci. **117** (1997) 512.
78. J. I. Chyi, D. Biswas and S. U. Iyer, Appl. Phys. Lett. **54** (1989) 1016
79. Franklin. G. E, Rich. D. H, Hawoong Hong, Miller. T and Chiang T. C, Phy. Rev. B **45** (1992) 3426
80. B. V. Rao, D. Gruznev, T. Tambo and C. Tatsuyama, Semicond. Sci. Technol. **16** (2001) 216
81. B.V. Rao, Atoji. M, Li D M, Okamoto. T, Tambo. T and Tatsuyama. C, Jap. J. Appl. Phys. **37** (1998) L1297
82. Michel. E, Xu J, Kim J. D, Ferguson. I and Razeghi. M, IEEE Phot. Tech. Lett. **8** (1996) 673
83. Rogalski. A, Infrared Phys. Technol. **43** (2002) 187
84. K.Wasa, M.Kitabatake, H.Adachi, Thin Film Materials Technology Sputtering of Compound Materials, William Andrew Inc and Springer-Verlag GmbH & Co.KG, United States, 2004. Chap.1
85. A. Goswami, Thin Film Fundamentals. New Age International (P) Limited, New Delhi, 1996. Chap.1
86. G. A. Kitaev and G. M. Fofauov, Zh. Priki. Khim (Leningrad) **43** (1970) 1694
87. K. Bindu, Ph.D Thesis, Department of Physics, Cochin University of Science and Technology, Kochi, India, May (2002)

88. K.Bindu, M. Lakshmi, S. Bini, C. Sudha Kartha and K. P. Vijayakumar, Proceedings of the National Symposium on Science and Technology of vacuum and Thin films (2001) p-33
89. K.Bindu, M. Lakshmi and C. Sudha Kartha, Semicond. Sci. Tech. **17** (2002) 270.
90. K. L. Chopra, Thin Film Phenomena, Robert E. Krieger Publishing Co. Inc., New York, 1979. Chap.1
91. L. Holland, Vacuum Deposition of Thin films, John Wiley & Sons Inc., New York, 1956. Chap.1
92. J. George, Preparation of thin films, Marcel Dekker Inc., New York, 1992.
93. B. D. Cullity, Elements of X-ray Diffraction (Reading, M A: Addison-Wesley) (1978) p. 170
94. J. I. Pankove, Optical process in semiconductors (Dover Publications, Inc. New York 1971), p. 3, 34
95. J. Bardeen, F.J.Blatt, L.H. Hall, Proceedings of the conference on Photoconductivity, Atlantic City,1954 (J. Wiley and Sons, Inc; New York 1956) p.146
96. D. R. Vij (Ed.) Luminescence of solids, Plenum Press, New York, 1998
97. Dieter K. Schroder, Semiconductor Materials and Device Characterisation, John Wiley and Sons, New York, (1998)
98. John F. Moulder, William F. Stickle, Peter E. Sobol and Kenneth D. Bomben, Perkin Elmer Corporation, USA (1992) p-20
99. P. E .J. Flewit and R. K. Wild, Physical methods for material characterization, second edition, IOP publishing, London, 2003. Chap. 7
100. Wei Kan Chue, James W Mayer and Marc A. Nicolet, Backscattering Spectrometry, Academic Press Inc. Florida (1978) p-23

CHAPTER 2

Part A

Effect of annealing on the formation of γ-In_2Se_3

Abstract

This part of the chapter gives a detailed study on the effect of annealing In/Se bilayer system at temperature ranging from 100°C to 400°C, leading to the formation of different phases of indium selenide. Multi-phases of indium selenide were identified using X-ray diffraction technique and optical absorption studies. Present study proved that multi-phased films were formed at lower annealing temperatures and annealing at 400°C is required to obtain single phase indium selenide thin films. X-ray photoelectron spectroscopy and Rutherford backscattering technique was used for compositional analysis.

2.1 Introduction

Indium selenide is a group III-VI compound semiconductor having direct band gap. Very recently it gained great importance due to potential application in photovoltaic device fabrication [1]. Depending upon the optical band gap of the film, it can be used as a window layer [2] in CIS/In_2Se_3 as well as an absorber layer [3, 4] in CdS/In_2Se_3 solar cells. γ-In_2Se_3 with wider band gap of 1.8 eV [5] is used as window layer while β-In_2Se_3 having a band gap 1.55 eV can be used as an absorber layer in solar cell fabrication. It is difficult to produce single phase and stoichiometric indium selenide due to the co-existence of several phases like InSe, In_2Se_3, In_4Se_3 and In_6Se_7 [10]. Among these, In_2Se_3 exists in five different phases, α, β, γ, δ and κ depending on the structural and optical properties [11]. A large number of studies were carried out on this material [6-14], but the results were rather confusing because of the existence of numerous phases in the same sample. This is one of the main drawbacks of this material. Presence of multi-phase in a single film can destroy the crystalline property of the material [11]. During the film growth process, there may be competitions between different phases present in the film. As a result of this, amorphous phases of indium selenide can be formed along with crystalline phase. Sensitive techniques like photoluminescence and electroluminescence were required to detect multi-phases in the film. In the present study, we have used optical absorption spectroscopy, which is a relatively inexpensive and commonly used analytical tool to detect the multi-phase in the film.

2.2 Experiment

Thin films of selenium with thickness 150 nm (measured using stylus thickness profiler) were deposited onto the glass substrate by using chemical bath deposition technique [15], over which 56 nm of In was deposited using resistive heating, maintaining a pressure of ~ $2x10^{-5}$ mbar during evaporation. Molybdenum boat was was used for evaporation. These In/Se bilayer films were

annealed at different temperatures from 100°C to 400°C for 1hour in vacuum (2x10^{-5} mbar.), keeping heating and cooling rate at 3°C/ min. Samples annealed at different temperatures 100°C, 150, 200, 300 and 400 ^{o}C were named as IS100, IS150, IS200, IS300 and IS400 respectively.

Another set of samples with thickness of Se layer 200 nm and indium layer of thicknesses 28 nm, 42 nm and 56 nm were prepared to study the effect of In concentration . The films annealed at temperatures 100, 150, 200, 300 and 400°C with In thickness 28 nm were named as 28IS 100, 28IS 150, 28IS 200, 28IS 300 and 28IS 400 respectively. Samples having indium film of thickness 42nm were named as 42IS 100, 42IS 150, etc. and that with thickness 56nm as 56IS 100, 58IS 150, etc.

X-ray diffraction (XRD) patterns were recorded in the range 2θ = 10° to 60° using Cu K_{α} (λ=1.5405 Å) radiation employing Philips (X'pert Pro.) X-ray diffractometer. Depth profiling of the samples was done using X-ray photoelectron spectroscopy (XPS) (ULVAC-PHI unit model: ESCA-5600CIM) employing argon ion sputtering. Optical absorption spectra were recorded with the help of UV-VIS-NIR spectrophotometer (model: Hitachi U-3410). Dark and photoconductivity were measured using source measuring unit (SMU-123X KIETHLY) in the voltage range 0-5 mV at room temperature. Electrical contacts were given through two patches of silver paint in the form of two end contacts, with a separation of 5 mm, such that the film area for the measurement was 5 mm^{2}. The output from the sample was taken using magnanin wire contacts given to the silver paint electrodes. Illumination was given to 5 mm^{2} area using (60 mW/cm^{2}) halogen bulb for 60 s and I-V were measured. Photoconductivity was measured under illumination time equal to 60 s.

Rutherford backscattering (RBS) measurements were carried out with 3 MeV He ions from 3 MV Tandem Pelletron Accelerator (Model-9SDH2). Here the ions were allowed to hit the samples at an angle 10° and back scattered ions were

detected using a silicon barrier detector placed at 170° in the backscattering geometry. Detector resolution was 20 keV and detector solid angle was 1msr. The RBS analysis was performed using GISA simulation [16].

2.3 Results and discussion

2.3.1 X-ray diffraction analysis

Figure 2.1 shows the XRD pattern of 'as deposited' Se film. It clearly indicated an amorphous nature. But on depositing indium over Se, we could see drastic change in the crystallinity of Se film (Fig. 2.2a). Annealing the In/Se system at 100°C resulted in the formation of γ-In_2Se_3 and In_6Se_7 (Fig. 2.2(b)). Unreacted In was also present in the film. But annealing at 150°C resulted in complete diffusion of In into Se, to form γ-In_2Se_3 along (212) at 2θ=29.81 and In_6Se_7 along (410) at 2θ=36.31, without any trace of elemental In (Fig. 2.2(c)). Single-phase β-In_2Se_3 was formed on annealing at 200 °C with grain orientation along (101) at 2θ=25.85 and (110) planes at 2θ=45.14 (Fig. 2.2(d)) [JCPDS card: 72-1470]. Annealing at 400°C resulted in formation of highly crystalline γ-In_2Se_3 having grains oriented along (110) at 2θ=25.04 and (006) at 2θ=27.65 respectively [JCPDS card: 40-1407] Formation of β-In_2Se_3 at 200°C annealing temperature was reported earlier and the following relation was suggested by Likforman et al. between the phases of In_2Se_3 [17].

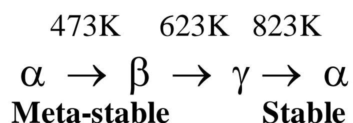

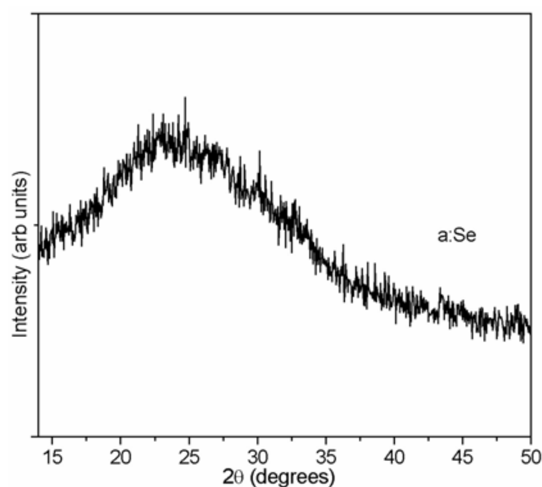

Figure 2.1: XRD spectrum of Selenium film prepared by CBD technique.

Samples annealed at 300°C had both β and γ phase of In_2Se_3. Interestingly existence of low temperature β-phase with high temperature γ-phase was reported earlier [18]. Indium selenide, formed at temperature up to 300°C, showed less crystallinity. This might be due to the presence of multi-phase indium selenide. The presence of mixed phase could disturb the crystallization of In_2Se_3 [11]. But the film formed at 400°C exhibited much better crystallinity as per the XRD results. In the process of crystallization, there may be competition between the grains of two phases, leading to poor crystallinity [11]. Less crystalline film formed at 200°C and 300°C could also be considered as the intermediate state of re-orientation of grains. The nature of re-orientation of grains at 200°C was reported by our own group, Bindu et al. [19]. They could not observe any phase transformation. In the present study, a complete transformation from β phase to γ phase was observed on annealing at 400°C, which was in accordance with the phase diagram given above.

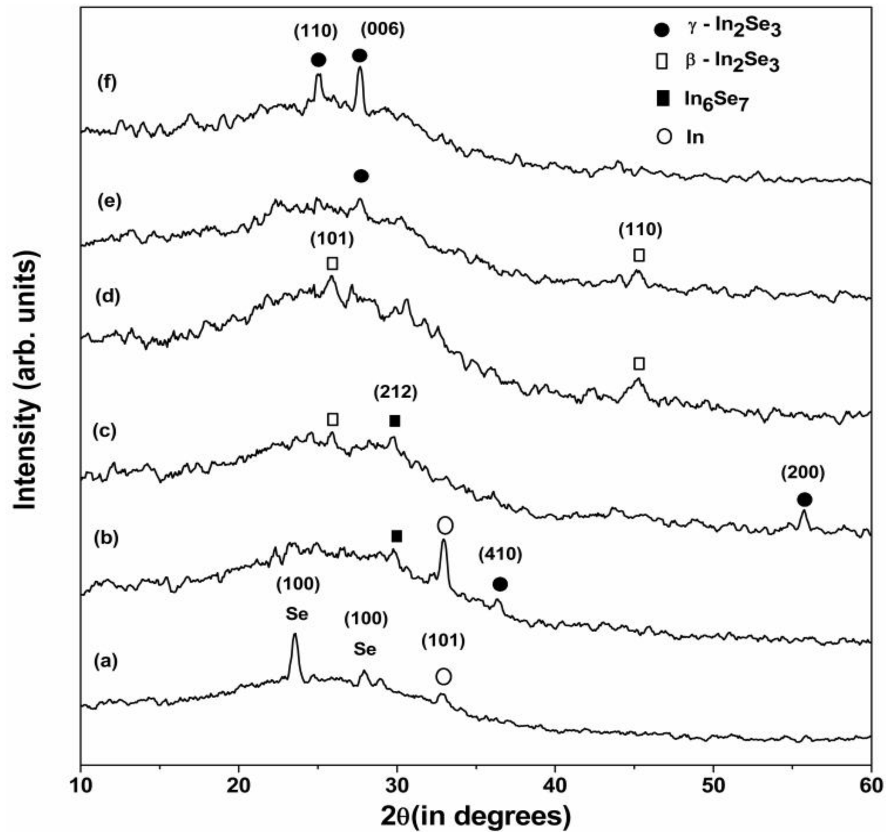

Figure 2.2: XRD spectrum of In/Se system (a) pristine (b) IS100 (c) IS150 (d) IS200 (e) IS300 (f) IS400

Average grain size of the samples was calculated using Debye scherrer's formula [20] (see section 1.10.2), and tabulated in Table 2.1. This shows that the average grain size of the films formed at 200°C and 300°C were poor and as the annealing temperature increased to 400°C the average grain size improved considerably.

Table 2.1: Showing average grain size of indium selenide thin films prepared at different annealing temperatures

Sample Identity	2θ	FWHM	Average grain size (Å)	Measured d-value (Å)	Standard d-value (Å)	Phase
IS100	29.81	0.81	101.7	2.99	3.00	In_6Se_7
IS150	55.72	0.27	330.6	1.65	1.65	γ-In_2Se_3
IS200	45.14	0.95	90.3	2.01	2.01	β-In_2Se_3
IS300	27.53	1.53	53.5	3.24	3.23	γ-In_2Se_3
IS400	27.65	0.19	416	3.22	3.23	γ-In_2Se_3

2.3.2 Optical studies

Optical absorption spectra of IS100, IS150 and IS300 showed peaks in the range 600 nm - 500 nm, in addition to the strong absorption in the range 850 nm – 700 nm. Figure 2.3(a) and (b) exhibit the optical absorption spectra of IS100 and IS300 respectively. This multiple absorption might be due to the presence of secondary phase [21] and/or defect levels present in the samples [22]. IS100 has (Fig. 2.3(a)) an absorption peak at 870 nm and is attributed to transition to a defect level present in the forbidden energy gap (detailed study regarding this has been done and is described in chapter 3). As the preparation temperature increased to 200 ^{o}C, absorption in the range 850 nm – 700 nm became very weak (Fig. 2.4). This might be due to the elimination of the secondary phases (γ-In_2Se_3 and In_6Se_7) present in the film and formation of single β-In_2Se_3. From XRD spectra (Fig. 2.2(d)), one could see that there is only one phase (β-In_2Se_3) present in IS200. Interestingly we observed only one absorption edge in the case of IS400 (Fig. 2.4). X-ray diffraction study showed single phase In_2Se_3 formation in the case of IS400 also.

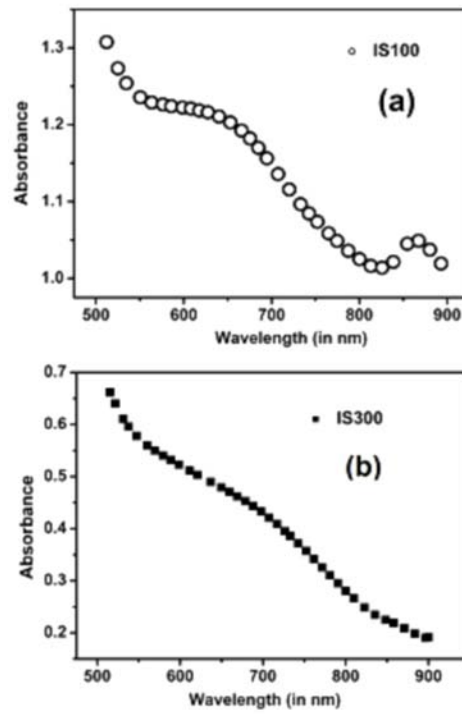

Figure 2.3: Optical absorption spectra of (a) IS100 and (b) IS300

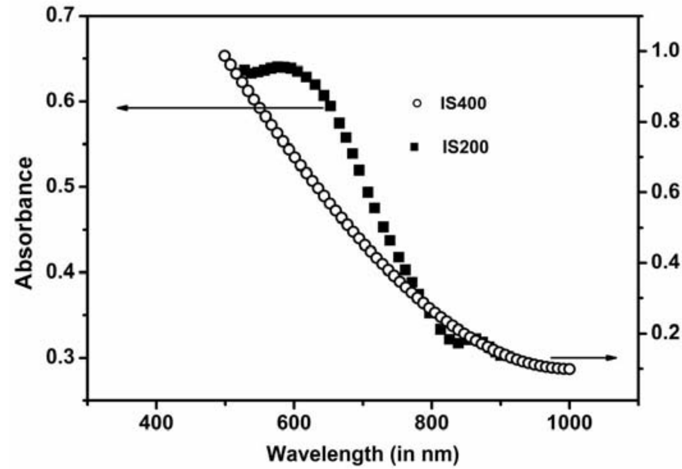

Figure 2.4: Optical absorption spectra of IS200 and IS400

According to the theory of optical inter-band absorption in solids, at the absorption edge, the absorption coefficient α varies with the photon energy (hν) according to the expression $\alpha h\nu = A\ (h\nu - E_g)^n$, where 'A' is a constant , 'E_g' is the optical energy gap and 'n' is an index with value ½ for the direct and 2 for in-direct allowed transitions [23]. The value of 'n' was determined by plotting ln(αhυ) versus ln(hυ-E), where E is the energy corresponding to the optical transition [24]. The slope of the plot would give the value of 'n'. Figure 2.5 show the ln (αhυ) versus ln (hυ-E) plot of IS400 corresponding to E ~ 2 eV. Slope of the plot showed n~1/2, indicating direct allowed transition. Most of the transition in the indium selenide samples showed n ~ 1/2 and hence for determining the optical band gap of the samples, $(\alpha h\upsilon)^2$ versus hυ plots were used.

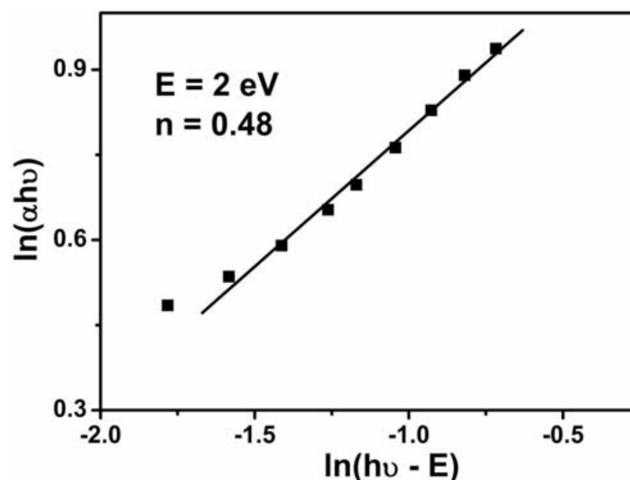

Figure 2.5: Shows the ln(αhυ) versus ln(hυ-E) plot of IS400

The optical band gap (E_g) of the samples was determined by extrapolating the straight line portion of $(\alpha h\upsilon)^2$ versus hυ plot to $\alpha = 0$, where hυ is the incident photon energy and α is optical absorption coefficient, determined from the absorption spectra [23]. Extrapolating the other straight line portions of $(\alpha h\upsilon)^2$ versus hυ plot to $\alpha = 0$, gave the indications of defect levels and/or the band gap of the secondary phase present in the sample [21, 23,25].

Figure 2.6 shows the $(\alpha h\upsilon)^2$ versus hυ graph of IS200, IS400 and figure 2.7 shows that of IS100, IS150, IS300 respectively. In the case of IS200 and IS400 optical band gap was obtained as 1.52 eV and 2 eV respectively, by extrapolating the straight line portion of $(\alpha h\upsilon)^2$ versus hυ plot to $\alpha = 0$. But in the case of IS100, IS150 and IS300 there were two straight line portions corresponding to two transitions in the sample. Extrapolating these two straight line portions to $\alpha = 0$, we obtained two energies. These two energies are attributed to the band gap of the different indium selenide phases present in the sample. Band gaps obtained for IS100 were 1.31 eV and 1.68 eV. IS150 exhibited 1.58 eV and 1.74 eV while for IS300 these were 1.5 eV and 2 eV. Of

these, the lower value was due to In_6Se_7 phase or β-In_2Se_3 phase while the higher one was due to γ-In_2Se_3. Optical band gap of β-In_2Se_3 reported by Julien et al. was 1.55 eV [26] and that of γ-In_2Se_3 is 1.8 – 2 eV [5,9]. X-ray diffraction also confirmed the mixed phase in IS100, IS150 and IS300. This proved that the films formed at lower annealing temperatures (IS150 and IS300) are having mixed phases (β and γ-In_2Se_3) and an annealing temperature of 400 ^{o}C is required for the formation of single phase γ-In_2Se_3.

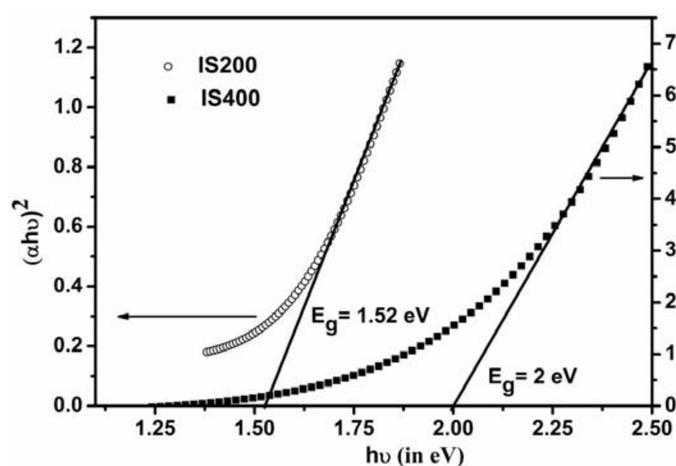

Figure 2.6: $(\alpha h\nu)^2$ versus hν graph of IS200 and IS400

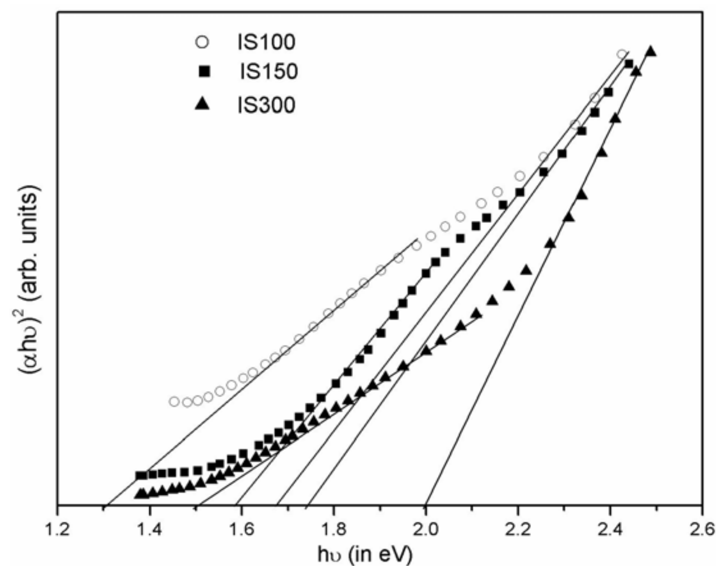

Figure 2.7: $(\alpha h\nu)^2$ versus hν graph of IS100, IS150 and IS300

2.3.3 X-ray photoelectron analysis

XPS studies were carried out on In/Se systems annealed at different temperatures. In the spectra X-axis shows the binding energy and Y-axis represents the depth/thickness of the sample. Depth-wise XPS measurements were done from the surface layer to the interior of the sample, by etching the surface layer of the material, using argon ion sputtering. Here after the etching of one layer was completed, XPS measurement as performed and this is 'one cycle' Like this 16 cycles of etching were performed on the sample to reach the substrate surface. Each sputtering removes approximately ~180 Å of the material.

From XPS analysis, one could clearly observe diffusion of In into Se layer in as prepared sample (Fig. 2.8(a)). Probably this must be the reason for the

crystallinity of Se film just after deposition of indium. However, the binding energies (BE) of In and Se did not indicate any compound formation. Sample annealed at 100 ^{o}C showed formation of indium selenide. The BE of In and Se were 444.8 eV and 54.8 eV respectively (Fig. 2.6(b)). BE of In ($3d_{5/2}$) in elemental state is in the range 443.55 to 444 eV while that in In_2Se_3 state is 444.8 eV [27]. Similarly BE of Se ($3d_{5/2}$ level) in elemental state is in the range 55.07 to 55.5 eV and in In_2Se_3 state this is 54.8 eV [27]. This clearly indicated the formation of γ -In_2Se_3. One could also see the presence of a very this layer of adsorbed oxygen on the surface of all the films.

The BE values obtained in the XPS analysis, clearly indicated that the films formed were In_2Se_3. When XPS results of IS150 showed a perfect mixing (Fig. 2.8(c)), results of IS200 indicated a shift towards higher BE (Fig. 2.8(d)). This might be due to the formation of β-In_2Se_3. However the peaks were again shifted to 444.8 eV in the case of IS300. This might be due to the phase transition taking place between 200 ^{o}C and 300 ^{o}C towards γ-In_2Se_3 from β-In_2Se_3. This transition was indicated in XRD also (Fig. 2.2(e)). A uniform mixing was observed in the case of IS400 (Fig. 2.8(f)).

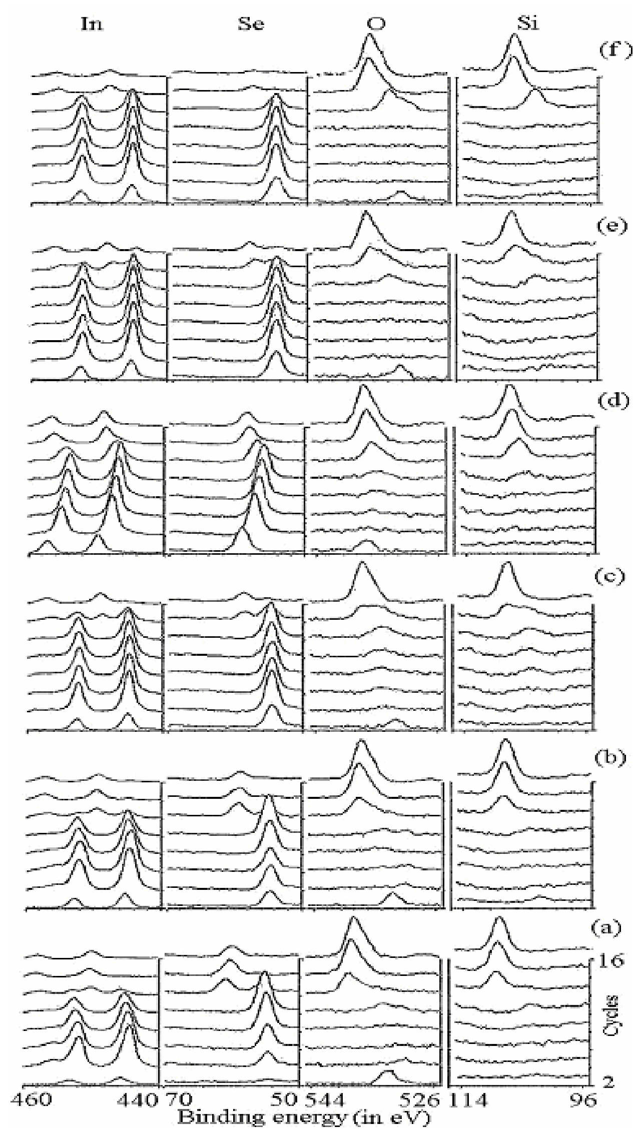

Figure 2.8: XPS spectrum of In/Se (a) Pristine (b) annealed at 100°C (c) 150°C (d) 200°C (e) 300°C (f) 400°C

Figure 2.9(a), (b) and (c) show the depth wise compositional analysis of IS200, IS300 and IS400 respectively. In the spectra X-axis shows the sputtering time (0 represents the surface and as the sputtering time increases information from the interior of the sample is obtained) and Y-axis shows the atomic concentration of different species present in the sample. The study showed that both indium and selenium were present uniformly throughout the depth in same proportion. Composition of In and Se in IS200, IS300 and IS400 were deduced as 58:38, 58:38 and 60:40 respectively. The low value of Se may be due to the preferential sputtering of Se during etching. This is one of the main drawbacks of XPS analysis, that it could not give correct information of atomic percentage of elements. To cross check the result (compositional analysis) obtained from XPS analysis we have performed Rutherford backscattering studies on these samples to find out the actual composition of indium selenide films (see section 2.4.5).

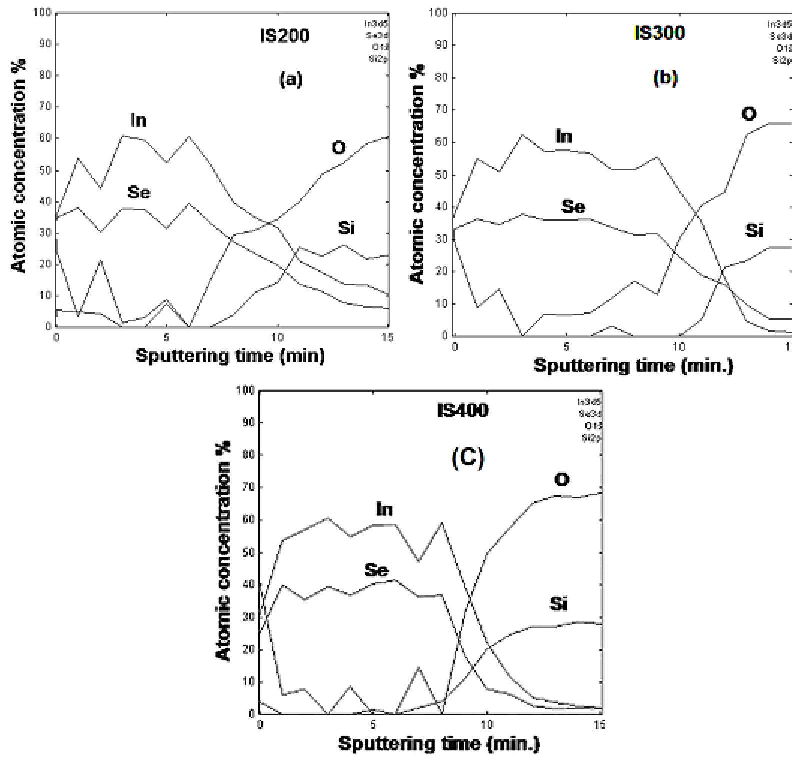

Figure 2.9: Shows the depth-wise composition of (a) IS200, (b) IS300 and (c) IS400

2.3.4 Electrical studied

Dark and photo conductivities of all the samples were measured at room temperature. In the case of IS100, photo current was almost equal to the dark current. IS150 also did not show any significant increase of photo current. But there was a large increase in photocurrent of IS200 and IS300 while IS400 had only a slight increase. Photosensitivity ($\Delta I/I_D$), (ie, the ratio of difference between photocurrent and dark current to the dark current) of IS100, IS150, IS200, IS300 and IS400 were -0.04, 0.07, 58.22, 18.24 and 0.37 respectively.

Low value of photosensitivity observed for IS100 and IS150 might be due to the destruction of minority carriers on illumination [21] (a detailed study to find out the cause of reduction in photosensitivity is carried out and presented in chapter 3).

Resistances of IS100 and IS150 were 3.5 kΩ and 3.4 kΩ respectively. IS200 and IS300 showed high sheet resistance of $8.7 \times 10^9\ \Omega$ and $15 \times 10^9\ \Omega$ respectively. This high sheet resistance might be due to the formation of β-In_2Se_3. Sharp increase in resistance was observed for IS200, which might be due to the phase transition [26], resulting in reduction of majority carriers. Due to this, minority carriers were protected leading to high photocurrent. IS400 had a sheet resistance of 6 kΩ. This reduction in sheet resistance indicated again the elimination of β phase.

2.3.5 Rutherford backscattering analysis

Graph in figure 2.10 depicts the RBS spectra of pristine and IS100 to IS400. Height of the interface i.e., the lower energy edge of In peak and higher energy edge of Se peak (marked by B) was increasing with increase in annealing temperature. This indicated that the mixing between In and Se was increasing with increase in annealing temperature. Compositional analysis was done using the formula [28],

$$m/n = A_A \sigma_A (E,\theta) / A_B \sigma_B (E,\theta) \qquad (2.1)$$

Where m/n is the stoichiometric ratio of a compound thin film A_mB_n ; A_A and A_B are the area under the curve of the elements A and B respectively and σ_A and σ_B are the scattering cross-section of element A and B respectively, given as,

$$\sigma_A (E,\theta) = \left(Z_1 Z_2 e^2 / 4E \right)^2 / Sin^4 (\theta/2) \qquad (2.2)$$

Where Z_1 and Z_2 are the atomic number of the probing ions and target atoms respectively, e is the electronic charge, θ the scattering angle and E the energy of the probing ion beam.

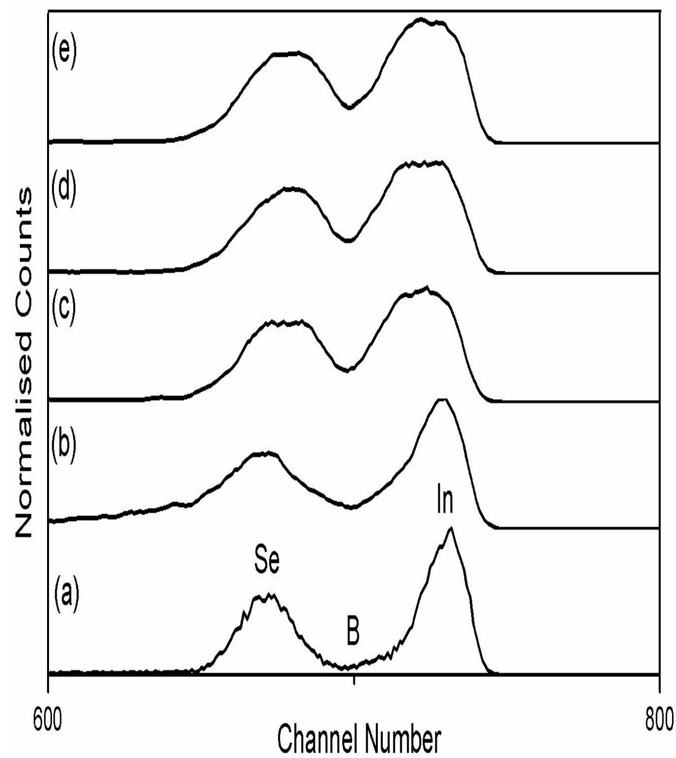

Figure 2.10: RBS spectrum of In/Se system (a) pristine (b) annealed at 100°C (c) 200°C (d) 300°C and (e) 400°C

Composition of In and Se in the films were calculated and tabulated in table 2.2. Composition analysis was also done using computer simulation GISA [16], which was in good agreement with those obtained from earlier calculation. Composition of the film IS100 was found to be not in aggrement with that of

simulated value and this was due to the existence of elemental In and Se in the film.

Table 2.2: Compositional analysis done using RBS on IS200, IS300 and IS400. Simulation has been carried out using GISA computer programme.

Annealing temperature in °C	Composition in %			
	Calculated		Simulated	
	In	Se	In	Se
200	36.75	63.25	37.75	62.25
300	37.5	62.5	38	62
400	36.18	63.82	38	62

2.4 Conclusion

Annealing In/Se bilayer films at lower temperature resulted in the formation of multi-phase film. Single phase β-In_2Se_3 with a band gap of 1.52 eV can be obtained at an annealing temperature of 200°C. But an annealing temperature of 400°C is required to obtain single phase γ-In_2Se_3 with a band gap of 2 eV. The study proved that, by optical absorption spectroscopy one could investigate the presence of secondary phases in the film. A phase transformation from β-In_2Se_3 to γ-In_2Se_3 as well as a structural re-orientation occurs at an annealing temperature of 400°C. RBS and XPS analysis proved formation of near stoichiometric (38:62) In_2Se_3 samples at higher temperatures.

CHAPTER 2

Part B

Effect of indium concentration on the c-axis growth of γ-In_2Se_3

Abstract

This part of the chapter deals with effect of indium concentration on the growth of γ-In_2Se_3 along the c-axis. We tried to grow In_2Se_3 along c-axis by varying annealing temperature and indium concentration. It was observed that the growth of In_2Se_3 crystallites along (006) plane (c-axis) depends on indium concentration. From the present study, we could say that there is a critical temperature and ratio (In/Se) above which γ-In_2Se_3 could be grown along c-axis..

2.5 Introduction

Due to the potential application of indium selenide thin films in photovoltaic devices fabrication, this material has been widely studied recently. For photovoltaic application one prefers crystalline films rather than amorphous films, since crystalline films provide low resistance for the charge carriers. In amorphous films, grain boundaries act as hurdles for charge carriers, thereby increasing the resistivity. In thin film solar cells, motion of the carriers is to be perpendicular to the substrate. Hence it is very important to have thin films with grain growth perpendicular to the substrate, making the motion of the charge carriers easier leading to the reduction of the series resistance.

Like most of the III_2-VI_3 compound semiconductors, γ-In_2Se_3 has tetrahedral bonding structure and this material crystallizes in hexagonal defect wurtzite structure. It has to be noted that, if any phase of In_2Se_3 shows semi-conducting properties, its crystal structure should be based on the tetrahedral bonding [29]. Again, in order to satisfy the octet rule for SP^3 hybridization, one-third of the cation sites are vacant in III-VI compounds [30, 31, 32]. Such structural vacancies behave as one atomic species and some times become ordered. These vacancies usually appear along the c-axis of wurtzite structure.

Lots of study has been carried out to understand the crystalline nature of In_2Se_3 thin films and it has been generally observed that InSe (hexagonal) and α-In_2Se_3 (rhombohedral) phases crystallize in layered structure, whereas, γ phase has defect wurtzite structure. The layered structure of α-In_2Se_3 consists of loosely stacked covalently bonded layers, including five atomic layers of Se-In-Se-In-Se [33, 34, 35], which are considered to be a spontaneous super lattice along c-axis. But β and δ phases have the hexagonal structure with lattice parameters a = 4.015 Å, c = 19.22 Å [JCPDS – 40 1408] and a = 4.014 Å, c = 9.64 Å respectively [JCPDS – 34 1313]. The κ phase of In_2Se_3, as reported recently by Groot et al. [14], have the same defect structure of γ phase with modification in

the structural vacancies, which slightly changes the lattice parameter and destroys the high symmetry of γ-In_2Se_3.

For photovoltaic application, it is well known that the thin films used should be textured with large grain size. In the case of hexagonal structure, the dangling bonds are present mainly in the face parallel to the c-axis [36]. Hence it is very critical to obtain films with a texture of (00l), having minimum trapping effect to photo generated carriers. Studies showed that γ-In_2Se_3 can be grown on different substrates along c-axis. Emziane et al. [37] demonstrated that γ-In_2Se_3 can be grown along c-axis in different substrates like glass, SnO_2, gold coated glass and mica sheet [37]. To obtain films with preferential orientation along c-axis, there exist a critical temperature and In/Se ratio. In the present study we have optimized the critical temperature and ratio to obtain In_2Se_3 along c-axis.

2.6 Results and discussion

2.6.1 X-ray diffraction analysis

(a) 28IS series of samples

Figure 2.11 depicts the XRD pattern of 28IS series of samples prepared at different temperatures, ranging from 100°C to 400°C. Thin films of In_2Se_2 were obtained even at 100°C annealing (Fig. 2.11(b)). Two peaks of In_2Se_3 were seen at 2θ=29.28 and 2θ=38.2 corresponding to (201) and (211) planes respectively, on annealing at 100°C (Fig. 2.11(b)). An additional peak at 2θ=55.78 (β-In_2Se_3) appeared at the expense of the peak at 2θ=29.28 for 28IS 150 (Fig. 2.11(c)), and this peak representing (201) plane completely vanished on annealing at 200°C (Fig. 2.11(d)). On increasing the annealing temperature further to 400°C, growth along (211) plane became predominant. Average grain size of the samples was calculated using Debye Scherrer's formula [20], and the results are tabulated in Table 2.3. There is a clear increase in average grain size of the samples with the increase in the annealing temperature. Lowest grain size of 105 Å was observed

for the sample annealed at 150 °C and the maximum [351 Å] was for the sample annealed at 400°C [duration of annealing-1 h]. One thing to be noted here is that the samples formed on annealing at 150 °C and 400 °C were composed of multi-phase of In_2Se_3. These samples contain both γ and β phases of In_2Se_3.

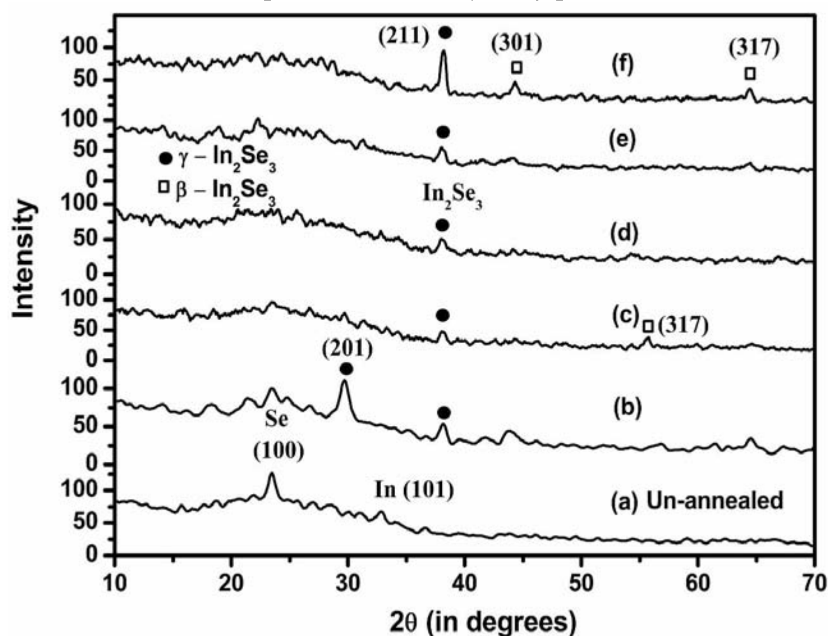

Figure 2.11: XRD spectrum of In/Se system (a) un-annealed (b) 28IS 100 (c) 28IS 150 (d) 28IS 200 (e) 28IS 300 and (f) 28IS 400.

Table 2.3: Showing the average grain size of 28IS series of samples.

Sl. No.	Sample identity	2θ	Average grain size (in Á)
1.	28IS 100	29.28	147
2.	28IS 150	38.2	105
3.	28IS 200	38.2	182
4.	28IS 300	38.2	202
5.	28IS 400	38.2	351

(b) 42IS series of samples

Figure 2.12 shows the XRD pattern of 42IS series of samples. Here we could observe that at lower annealing temperature (up to 150°C) In_2Se_3 phase was formed along (201) plane (Fig. 2.12(b)). As in the case of 28IS series, the sample formed at an annealing temperature of 150°C showed reflection from β-In_2Se_3 phase with γ phase (Fig. 2.12(c)). On annealing at 200°C, both reflections from γ and β disappeared and a new reflection from In_6Se_7 along (201) was observed. The film became completely amorphous on annealing at 300°C (Fig. 2.12(e)). But in the case of 42IS 400 grains were oriented in (006) direction and crystallinity was much better (Fig. 2.12(f)). In this case we could see a re-orientation of grains as well as re-crystallisation on annealing at 400°C. Interestingly one could see that the grains were oriented along the c-axis, which is perpendicular to the substrate plane.

Table 2.4: Showing the average grain size of 42IS series of samples

Sl. No.	Sample identity	2θ	FWHM	Average grain size (in Á)
1.	42IS 100	29.61	0.370	222 Å
2.	42IS 150	29.73	0.378	217 Å
3.	42IS 200	21.89	0.242	334 Å
4.	42IS 300	-	-	-
5.	42IS 400	27.6	0.172	475 Å

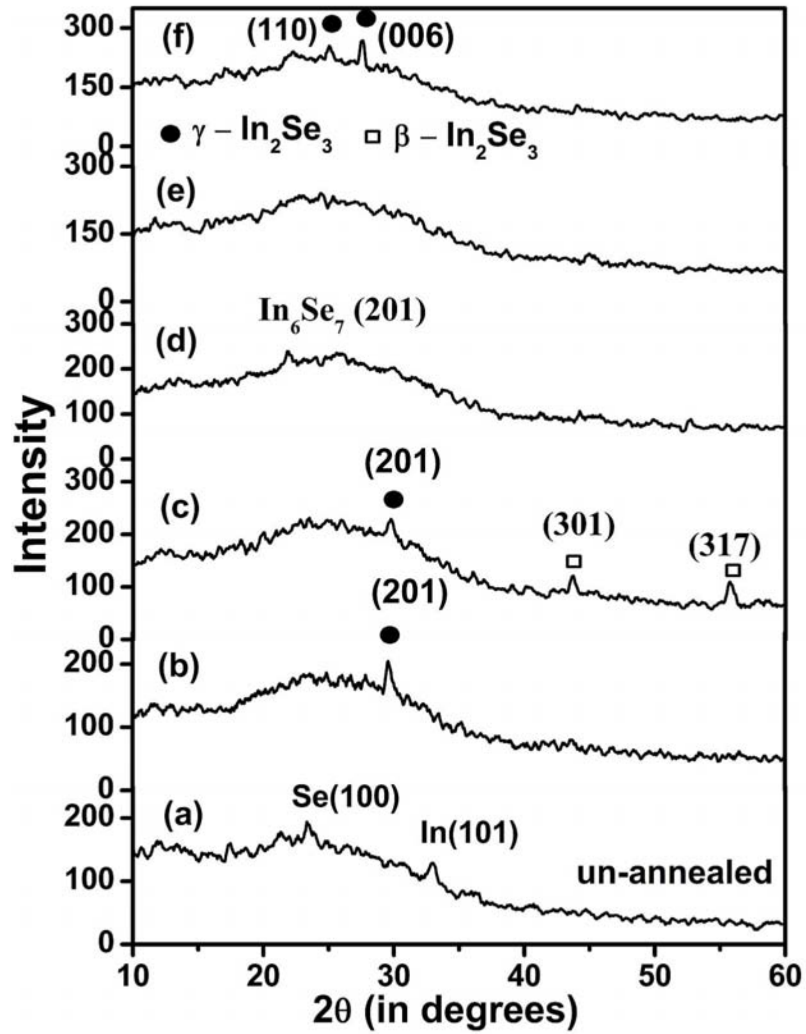

Figure 2.12: XRD pattern of In/Se system (a) pristine (b) 42IS 100 (c) 42IS 150 (d) 42IS 200 (e) 42IS 300 and (f) 42IS 400

(c) 56IS series of samples

Figure 2.13 shows the XRD pattern of the 56IS series. On increasing the indium thickness (concentration) to 56 nm, the c-axis growth of γ-In_2Se_3 started even at 150°C annealing (Fig. 2.13(b)). But annealing at 200°C resulted in complete amorphisation of the sample (Fig. 2.13(c)), and recrystallisation started at 300°C (Fig. 2.13(d)). Here also we could see recrystallisation as well as a re-orientation of plane from (201) to (006). But the recrystallisation occurred at much lower annealing temperature (300°C) in comparison with the 42IS series, where the re-orientation occurred at 400°C.

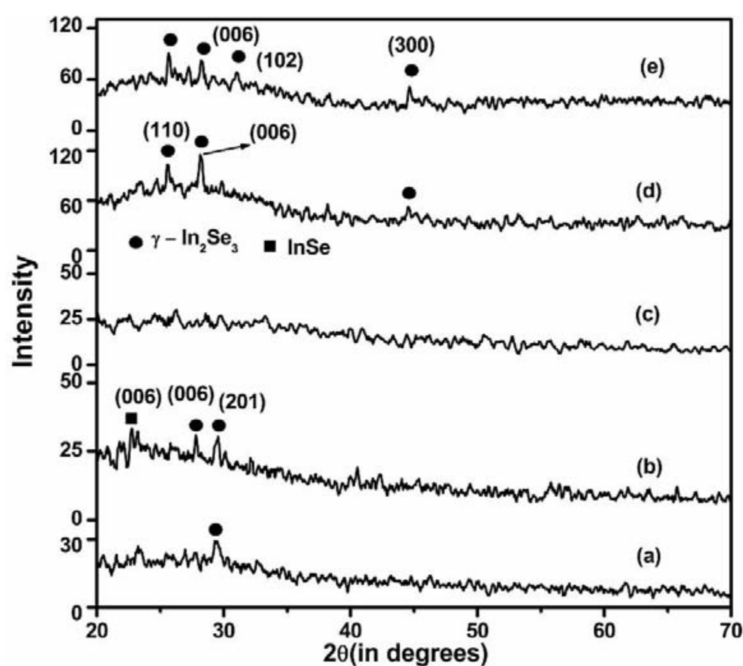

Figure 2.13 : XRD spectrum of In/Se system with Se=200nm and In=56nm, annealed at different temperatures (a) 56IS 100 (b) 56IS 150 (c) 56IS 200 (d) 56IS 300 and (e) 56IS 400

The average grain size of the samples were calculated and found that the sample annealed at 150°C showed the highest grain size. Values are tabulated in Table 2.5. The samples formed after recrystallisation (at 300°C and 400°C), were having smaller grains in comparison with that before recrystallisation. The lattice parameters of the samples were also found to be in good agreement with the reported value, a=7.13 Å, c=19.01 Å (values tabulated in Table 2.5) [37, 38, 39]. After recrystallisation the lattice parameters (a and c), reduced on annealing at 300°C. On increasing the annealing temperature (to 400°C) it further reduced. Decrease in lattice parameters might be due to the constraints acting along the c-axis due to the recrystallisation. During annealing, there can be competitions between grains of different phases which results in amorphous phase. Absence of secondary phases after annealing at 300 and 400°C showed that the constraints were exerted during the growth of the grains. It was shown by Amory et al. that the presence of InSe and In_4Se_3 could disturb the crystallisation of In_2Se_3 along c-axis [11]. In our case, we could see the presence of InSe phase in 56IS 150.

Table 2.5: Average grain size and lattice parameters of 56IS series of samples. (Lattice parameters of 56IS 100 was not determined because there was only one reflection from (201) plane. In the case of 56IS 200, sample was completely amorphous).

Sl. No.	Sample identity	2θ	FWHM	Average grain size	Lattice parameter a	Lattice parameter c
1	56IS 100	29.46	0.481	171 Å	-	-
2	56IS 150	27.82	0.179	457 Å	7.06 Å	19.24Å
3	56IS 200	-	-	-	-	-
4	56IS 300	28.2	0.206	399 Å	6.97 Å	19.01 Å
5	56IS 400	25.66	0.198	401 Å	6.94 Å	18.91 Å

For the sample 42IS 400, the film growth was along c-axis [i.e. (006) plane] (Fig. 2.12(f)), whereas for 28IS 400 the growth was along (211) plane. It was shown by Emziane et al. [36] that temperature $\geq$ 300°C was required for obtaining crystalline γ-In_2Se_3. He also showed that grains would grow along c-axis for In rich (Se deficient) samples [36, 37]. Indium rich film (with In=42 nm; 42IS 300 sample) was completely amorphous. But samples 42IS 100, 42IS 150 and 42IS 200 were crystalline and the film grew along (201) plane. On annealing at 300°C In diffused deep into Se lattice, making the growth along (201) difficult. To grow along c-axis, [(006) plane] there was no sufficient quantity of indium atoms and/or the temperature was not enough to grow In_2Se_3 along (006) plane. The presence of secondary phase too made the growth along c-axis difficult. This was the reason for amorphous nature for 42IS 300 and was confirmed by the study using higher indium concentration (In=56 nm), in which we obtained In_2Se_3 along c-axis at comparatively lower 300°C. On increasing the indium concentration, there were more indium atoms available to probe the growth of In_2Se_3 along c-axis.

For Se rich film (Se=200 nm, In=28 nm), the film grew along (211) direction and crystallinity increased with increase in annealing temperature. Here neither the growth along c-axis nor the reorientation of planes was observed unlike in In rich films. With XRD study, we could see a common trend that, the crystallinity increased with increase in annealing temperature. Also we could see that growth along the c-axis depended on In concentration and annealing temperature. For Se rich film, film did not grow along c-axis. In the case of slightly In rich sample (In=42 nm), 400°C was required, whereas for In rich sample (In=56 nm) only 300°C was required for the growth of film along c-axis. Thus we can say that there is a critical temperature and ratio (In/Se) above which γ-In_2Se_3 can be grown along c-axis.

2.6.2 Optical Absorption Studies

(a) 28IS series of samples

Figure 2.14 shows the optical absorption spectra of 28IS series of samples in the wavelength range 1600 nm to 400 nm. All the samples showed multiple absorption except 28IS 300. The multiple absorption is due to the presence of parasite phases and/or due to defect levels, present in the forbidden energy gap [21, 25]. It was shown by Marsillac et al. [40] that the optical absorption spectroscopy was one of the tools to detect the presence of multiple phases present in the film. Even though 28IS 200 did not show secondary phases in the XRD pattern, we observed multiple absorption. This indicated that small amount of secondary phases were present in these films which were not detected by XRD analysis. The XRD analysis of the samples 28IS 150 and 28IS 400 indicated the presence of β-In_2Se_3 phase (Fig. 2.11). The optical band gap of the films were deducted from $(\alpha h\upsilon)^2$ versus $(h\upsilon)$ plot, by extrapolating the straight line portion of the plot to $\alpha = 0$, the values of which are tabulated in table 2.6. The highest value [1.9 eV] of IS150 is attributed to the γ-phase and the lowest value [1.69 eV] to the β-phase present in the film. Highest band gap of 2.43 eV is obtained for the single phase γ-phase film 28IS 300 (Fig. 2.15). The formation of single phase film might be responsible to get higher band gap.

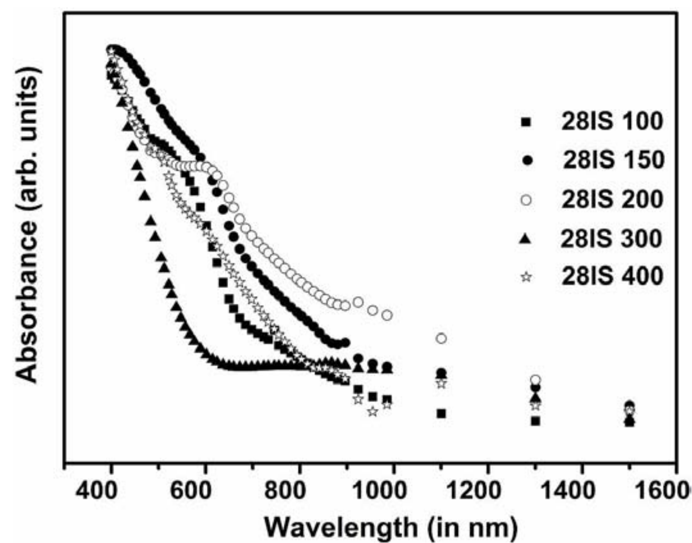

Figure 2.14: Optical absorption spectra of indium selenide samples prepared at different annealing temperature with Se=200 nm and In=28 nm.

Table 2.6: Optical band gap, resistance and photosensitivity of indium selenide prepared at different temperatures with Se = 200 nm and In = 28 nm

Sl.No:	Sample identity	Phase	Band gap (eV)	Resistance (Ω)	Photosensitivity
1.	28IS100	γ-In_2Se_3	1.84	1.4 G	25
2.	2 8IS150	γ-In_2Se_3	1.9	33 G	0.44
3.	28IS200	β and γ-In_2Se_3	1.64 2.23	41 G	0.72
4.	28IS300	γ-In_2Se_3	2.43	8.9 K	0.07
5.	28IS400	β and γ -In_2Se_3	1.92 2.07	6.8 K	0.04

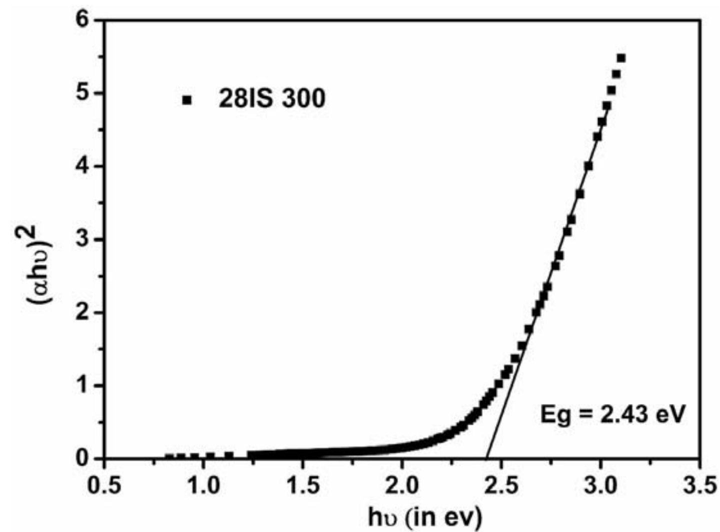

Figure 2.15: $(\alpha h\upsilon)^2$ versus (hυ) plot of sample 28IS 300 (with Se = 200 nm and In = 28 nm)

(b) 42IS series of samples

The optical band gaps of the 42IS series were measured and these are tabulated in table 2.7. We can see that there is no change in the band gap of 42IS 100. The samples 42IS 150 and 42IS 200 were formed with mixed phases of β and γ-In_2Se_3 respectively.

Table 2.7: Optical band gap, resistance and photosensitivity of indium selenide prepared at different temperatures with Se = 200 nm and In = 42 nm.

Sl.No:	Sample Identity	Phase	Band gap (eV)	Resistance (Ω)	Photosensitivity
1.	42IS100	γ-In_2Se_3	1.84	4.7 M	3.7
2.	42IS150	β and γ-In_2Se_3	1.82	140 M	30
3.	42IS200	In_6Se_7 and γ-In_2Se_3	1.72	3.2 K	0.16
4.	42IS300	In_6Se_7 and γ-In_2Se_3	1.72	24 K	0.14
5.	42IS400	γ-In_2Se_3	2.04	26 G	4.3

Presence of secondary phases was evident from the absorption spectra (Fig. 2.16), and the band gap was deducted from $(\alpha h\upsilon)^2$ versus (hυ) plot. The sample 42IS 300 was completely amorphous (Fig. 2.12 (e)), having similar absorption as that of 42IS 200. Therefore we concluded that this sample was also made of mixed phases of In_6Se_7 and γ-In_2Se_3. The presence of parasite phases destroyed the crystallization of the sample. As evident from the XRD pattern of 42IS 400 (Fig. 2.12(f)), the film was single phase γ-In_2Se_3. But in optical absorption studies it also showed an additional absorption around 640 nm. This absorption is attributed to a defect level situated 240 meV below the conduction band (or 1.8 eV above the valence band). Figure 2.17 shows the $(\alpha h\upsilon)^2$ versus (hυ) plot of 42IS 400, in which the band gap and the defect levels are identified. Inset of figure 2.17 shows the $(\alpha h\upsilon)^2$ versus (hυ) plot of 42IS 100.

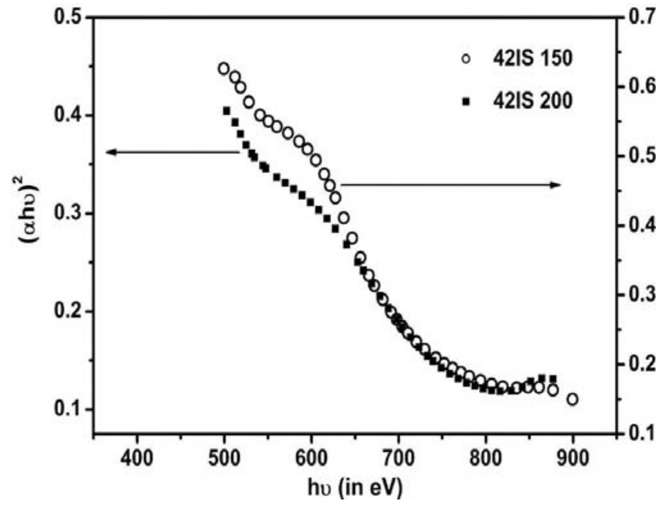

Figure 2.16: Optical absorption spectra of indium selenide samples prepared at different annealing temperatures 150 and 200 ^{o}C with Se = 200 nm and In = 42 nm.

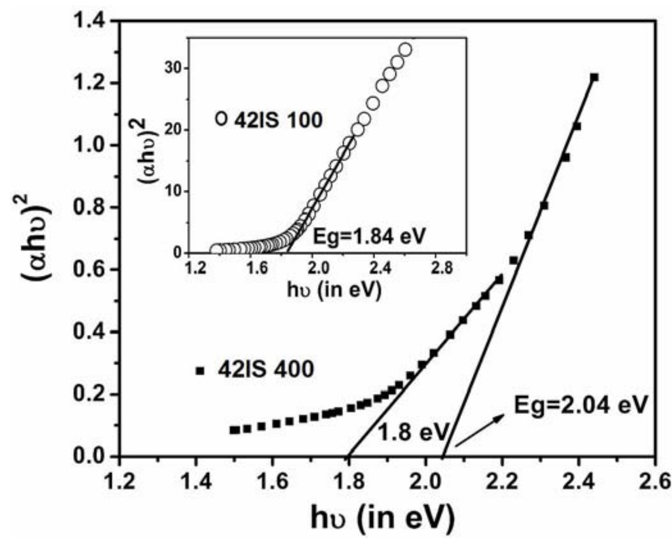

Figure 2.17: $(\alpha h\upsilon)^2$ versus (hυ) plot of sample 42IS 400, inset shows the $(\alpha h\upsilon)^2$ versus (hυ) plot of 42IS 100 (with Se = 200 nm and In = 42 nm).

(c) 56IS series of samples

Table 2.8 shows the optical band gap of 56IS series of samples prepared at different annealing temperatures. 56IS 100 does not show any variation in optical band gap. But 56IS 150 and 56IS 200 showed two band gaps and correspondingly two phases. The lowest value of 1.55 eV was attributed to the band gap of InSe phase and 2 eV was that of γ-In_2Se_3 (Fig. 2.18). As in the case of 28IS 300, the sample formed with single phase γ-In_2Se_3. It showed only one absorption, corresponding to energy of 1.96 eV. But in the case of 56IS 400, two absorptions were observed, one in the range of 600 to 700 nm and the second in the range of 500 to 600 nm (inset of figure 2.19). Since the sample did not show any secondary phase in the XRD study, the absorption in the range 600 to 700 nm corresponding to an energy 1.76 eV is attributed to an absorption to a defect level 1.76 eV above the valence band (figure 2.19).

Table 2.8: Showing the optical band gap, resistance and photosensitivity of indium selenide prepared at different temperatures with Se = 200 nm and In = 56 nm.

Sl.No:	Sample Name	Phase	Band gap (eV)	Resistance (Ω)	Photosensitivity
1.	56IS100	γ-In_2Se_3	1.84	9 K	-0.1
2.	56IS150	InSe and	1.7	3 G	72
		γ-In_2Se_3	1.92		
3.	56IS200	InSe and	1.56	3.9 K	0.19
		γ-In_2Se_3	2		
4.	56IS300	γ-In_2Se_3	1.96	45 G	62
5.	56IS400	γ-In_2Se_3	2.04	5.6 G	0.53

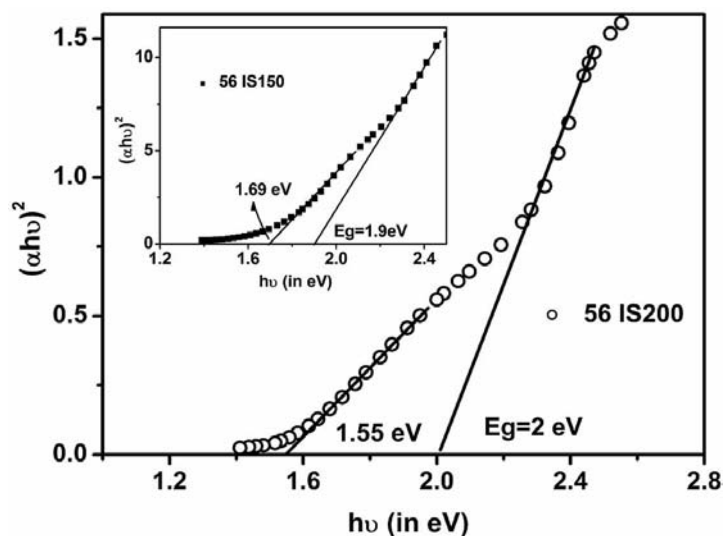

Figure 2.18: $(\alpha h\upsilon)^2$ versus $(h\upsilon)$ plot of sample 56IS 200, inset shows the $(\alpha h\upsilon)^2$ versus $(h\upsilon)$ plot of 56IS 150 (with Se = 200 nm and In = 56 nm).

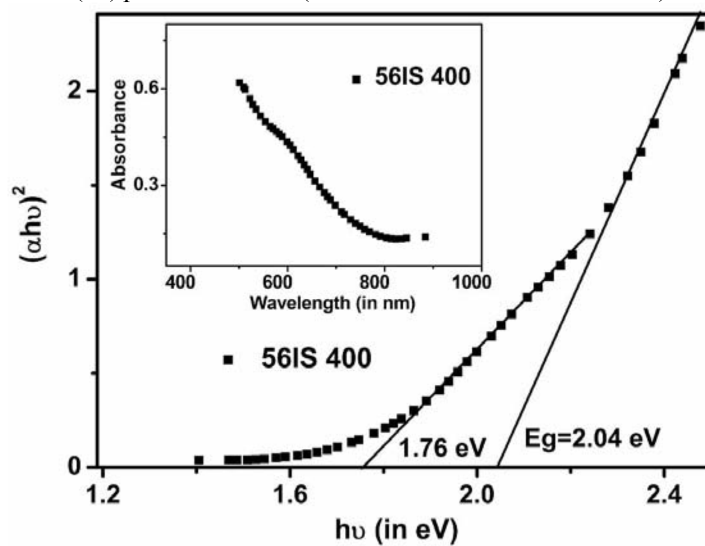

Figure 2.19: $(\alpha h\upsilon)^2$ versus $(h\upsilon)$ plot of sample 56IS 400, inset shows the absorption spectra of 56IS 400 (with Se = 200 nm and In = 56 nm).

2.6.3 Electrical Studies

Electrical studies on the 28IS series of samples showed decrease in resistance on increasing the annealing temperature (Table 2.6). The sample 28IS 100 which showed a resistance of 1.4 GΩ reduced to 6.8 K (28IS 400) on annealing at 400°C. Maximum photosensitivity ($P = \Delta I/I_D$) of 25 was exhibited by 28IS 100 and it was minimum [0.04] for the sample annealed at 400 ^{o}C (28IS 400). In this case, we observed that the average grain size (crystallinity) of the samples increased with increase in annealing temperature. This might be the reason for decrease in resistance with the increase in annealing temperature. However, the photosensitivity of the films decreased on annealing. In fact this parameter should have increased since the increase in grain size reduced the grain bonding density allowing the photo generated carriers to survive. The presence of multiple phases may be the reason for the reduction of photosensitivity.

In the case of 42IS and 56IS series, we could notice a random variation of resistance with annealing temperature (Table 2.7 and 2.8). This might be due to the presence of multiple phases present in the sample. It was reported by Groot et al. [14] that γ-In_2Se_3 films were highly resistive than the films having mixed phases. But this was not true for all the samples presented here. One interesting thing to be noted is that unlike crystalline films, the amorphous films 42IS300 and 56IS200 showed low resistance of 24 kΩ and 3.9 kΩ respectively. However the photosensitivity was minimum for the samples 42IS 300 and 56IS 200 [0.16 and 0.19 respectively]. In the case of amorphous samples, the grain boundary density will be high and it might be destroying the photo-generated carriers, resulting in low photosensitivity.

In the case of 42IS series, 42IS 150 showed the maximum photosensitivity of 30 at room temperature. The photosensitivity decreased with increase in annealing temperature, [0.16 to 0.14], from 200 to 300 ^{o}C. This decrease in photosensitivity was due to the increase in grain bonding density per unit

volume of the films [41]. At the grain bonding of each of the crystallites the incomplete atomic bonding could act as trap centers. These could trap the charge carriers at the grain boundaries, and hence a space charge was be built up locally. On increasing the annealing temperature to 400 ^{o}C, the photosensitivity as well as the crystallinity (average grain size) increased. Increase in grain size decreased the grain boundary density, and this allowed photo generated carriers to survive, enhancing the photosensitivity/ transport property of γ-In_2Se_3 thin films.

One more thing to be noted is that the 42IS 400 sample was grown along c-axis (006) plane. Emziane et al. [41] showed that γ-In_2Se_3 textured along (00l) plane showed better photo conducting behavior. In the samples grown along c-axis, the presence of dangling bonds was minimum and this helped photo generated carriers to survive thereby increasing the photoconductivity. In the case of 56IS series the samples 56IS 150 and 56IS 300 were textured along (006) direction. These samples showed maximum photosensitivity [72 and 62] for 56IS 150 and 56IS 300 respectively. On increasing the annealing temperature to 400°C, the sample became randomly textured with preferential orientation along (110) plane. This reduced the photosensitivity of the sample to 0.53, giving support to the argument that the films textured along (00l) plane will show better photoconductivity.

2.7 Conclusion

Growth of γ-In_2Se_3 along c-axis depended on critical temperature and (In/Se) ratio. Se rich films never grew along c-axis irrespective of the annealing temperature (100 to 400°C), instead, it grew along (103) plane. For In rich film, 400°C was required; but as In concentration increased, only 150°C annealing was required for the growth along c-axis, and re-crystallization occurred at 300°C. The study proved that β phase of In_2Se_3 could be eliminated by increasing the indium concentration. The samples grown along c-axis showed

better photosensitivity due to the absence of dangling bonds which traps photogenerated carriers.

References

1. S.T. Lakshmikumar and A.C. Rastogi, Sol. Energy Mater. Sol. Cells **32** (1994) 7
2. G. Gordillo and C. Calderon. Sol. Energy Mater. Sol. Cells **77** (2003) 163.
3. S.M El-Sayed. Vacuum **72** (2004) 169.
4. M.A. Kenawy, H.A. Zayed and A.M.A. El-Soud. J. Mater. Sci.- Mater. Electron. **1** (1990) 115
5. C. Julien, A. Cheavy and D. Siapkas. Phys. Status Solidi A **118** (1990) 553.
6. J. Herrero and J. Ortega, Sol. Energy Mater. **16** (1987) 477.
7. B. Kobbi, D. Ouadjaout and N. Kesri, Vacuum **62** (2001) 321.
8. S. N. Sahu, Thin Solid Films **261** (1995) 98.
9. M. Yudasaka, T. Matsnoka and N. Nakanishi, Thin Solid Films **146** (1987) 65.
10. M.Parlak and C. Ercelebi, Thin Solid Films **322** (1998) 334.
11. C. Amory, J.C. Bernede and S. Marsillac, J.Appl. Phys. **94** (2003) 6945.
12. D. Eddike, A. Ramdani, G. Brun, J.C. Tedenae and B. Leautard, Mater. Res. Bull. **33** (1998) 519.
13. J. Ye, S. Soeda, Y. Nakamura and D. Nittono, Jap. J. Appl. Phys. (Part 1) **37** (1998) 4264.
14. C. H. de. Groot and J.S. Moodera, J. Appl. Phys. **89** (2001) 4336.
15. K.Bindu, M. Lakshmi, C. Sudha Kartha et al. Semicond. Sci. Technol. **17** (2002) 270.
16. S. Rath and S.N. Sahu, Europhys. Lett. **67** (2004) 294.
17. A. Likforman, P.H. Foureroy, M. Guittard, J. Flahant, R. Poirier and N. Szydlo, J. Solid State Chem. **33** (1980) 91.
18. M. Parlak and C. Erecelebi, Thin Solid Films **322** (1998) 344.
19. K. Bindhu, Ph. D Thesis, Dept. of Physics, Cochin University of Science and Technology, India. (2002) p.108.
20. Cullity B.D, Elements of X-ray Diffraction (Reading, M A: Addison-Wesley) (1978) p. 170.
21. R. Sreekumar, R. Jayakrishnan, C. Sudha Kartha and K. P. Vijayakumar, J. Appl. Phys. **100** (2006) 33707.

22. E. J. Johnson and H. Y. Fan, Phys. Rev. **139** (1965) A1991.
23. J. I. Pankove, Optical process in semiconductors (Dover Publications, Inc. New York 1971), p. 34.
24. S. Chakrabarti, D. Ganguli and S. Chaudhuri, Physica E **24**, (2004) 333
25. R. Sreekumar, R. Jayakrishnan, C. Sudha Kartha, K. P. Vijayakumar, Y. Kashiwaba and T. Abe, Sol. Energy Mater. Sol. Cells **90,** 2908 (2006).
26. C. Julien, M. Eddrief, K. kambas and M. Balkanski, Thin Solid Films **137** (1986) 27.
27. K. Bindhu, C. Sudha Kartha, K.P. Vijayakumar, T. Abe and Y. Kashiwaba, Appl. Surf. Sci. **191** (2002) 138.
28. James. W. Mayer, Marc-A. Nicolet, Backscattering Spectroscopy, Academic Press, INC. (London) LTD. (1978) p. 109.
29. Jiping Ye, Sigeo Soeda, Yoshio Nakamura and Osamu Nittono, Jpn. J. Appl. Phys. **37** (1998) 4264.
30. P. C. Newman, J. Phys. Chem. Solid. **23** (1962) 19.
31. P. C. Newman, J. Phys. Chem. Solid. **24** (1963) 45.
32. D. Lubbers and V. Leute, J. Solid State Chem. **43** (1982) 339.
33. J. Ye, Ph.D Thesis at Tokyo Institute of Technology, Tokyo, Japan, 1995.
34. J. Ye, Y. Nakamura and O. Nittono, Philos. Mag. A, **73** (1996) 169.
35. J. Ye, T. Yoshida, Y. Nakamura and O. Nittono, Appl. Phys. Lett. **67** (1995) 3066.
36. M. Emziane, S. Marsillac, J. Ouerfelli, J. C. Bernede and R. Le. Ny, Vacuum **48** (1997) 871.
37. M. Emziane and R. Le. Ny, J. Appl. Phys. **32** (1999) 1319.
38. A. Likforman, D. Messain, M. Guittard and J. Flahault, C. R. Acad. Sci. **274** (1972) 378.
39. A. Likforman, D. Carre and R. Hillel, Acta Cryst. B **34** (1978) 1.
40. S. Marsillac, A. M. Combot-Marie, J. C. Bernede, A. Conan, Thin Solid Films **288** (1996) 14.
41. M. Emziane and R. Le. Ny, Thin Solid Films **366** (2000) 191.

CHAPTER 3

Investigations on the anomalous negative photoconductivity in γ-In_2Se_3

Abstract

This chapter deals with the photoconductivity studies of indium selenide thin films. γ-In2Se3 film showed negative photoconductivity at room temperature. We tried to investigate the cause of negative photoconductivity in the sample. Photoconductivity of the films exhibited a strong dependence on the concentration of indium in the films. The trap levels and recombination centre in the samples were identified using optical absorption and photoluminescence studies respectively.

3.1 Introduction

For photovoltaic device fabrication, one prefers crystalline and photoconductive samples, having low resistance. It was first reported by Abdinov et al. [1] that InSe exhibited negative photoconductivity. This can affect the performance of the cell adversely. Hence it is very important to study the photoconductivity of the films before switching on to solar cell fabrication. But till now there was no report on negative photoconductivity exhibited by γ-In_2Se_3 thin films.

Negative photoconductivity (NPC) of a semiconductor is defined as decrease in electrical conductivity under illumination. It may be due to the reduction of mobile carriers, (electrons in n-type) in the conduction band and destruction of minority carriers in valance band. This will result in the decrease of photoconductivity, lower than the dark conductivity. This type of anomalous behaviour was observed in several other materials such as GaAs [2, 3], Au:Ge alloy [4, 5], Cobalt doped Si [6], $Cd_{1-x}Fe_xSe$ [7], n-PbTe [8] and in α-Se [9]. Different models were proposed by the authors to explain this effect. Chou et al. [3] explained NPC in GaAs as due to the rapid recombination of electrons from conduction band with "hole plasma" in donor like trap, which was ionized by the incident light. But Claude et al. [6] used the same "two level model" suggested by Stockman [10] and Johnson et al. [5], to explain the same effect in Ge. Later Chang et al. proposed "three level model" to explain the NPC in Co doped Si [11]. Highly negative photoconductivity at low intensity illumination made GaAs suitable for application in sensitive detectors [2]. However, GaAs and most of the materials mentioned above showed NPC at lower temperature (below 80K) and became positive in photoconductivity above room temperature. Interestingly in the present case, In_2Se_3 showed NPC even at room temperature. This made indium selenide useful as a detector material, which did not require liquid nitrogen temperature.

In the present chapter, we try to analyse the anomalous NPC in γ-In_2Se_3 with the help of optical absorption, photoconductivity and photoluminescence studies. It is found that the model suggested by Stockman [10] and Johnson et al. [5] is useful in explaining this phenomenon.

3.2 Experiment

Thin films of indium selenide were prepared by annealing Indium/Selenium bilayer system at 100°C for duration of one hour, at a pressure of $2x10^{-5}$ mbar. Thin films of selenium with thickness 200 nm [measured using stylus thickness profiler (Model-Dektak 6M)] were deposited on the glass substrate using chemical bath deposition technique [12]. Over this, In was deposited using resistive heating, at a pressure of ~ $2x10^{-5}$ mbar. Molybdenum boat was used for evaporation. By keeping Se thickness 200 nm, thickness of In layer was varied as 28 nm, 42 nm and 56 nm respectively. These films were annealed at 100 ^{o}C and named as 28IS 100, 42IS 100 and 56IS 100.

X-ray diffraction (XRD) patterns were recorded in the range $2\theta = 20^o$ to 60° using Cu K_α (λ=1.5405 Å) radiation employing Philips (X'pert Pro.) machine. Optical absorption spectra were recorded with the help of UV-VIS-NIR spectrophotometer (model: Hitachi U-3410) in the range 400 nm to 900 nm. For photoluminescence (PL) measurements, samples were loaded in a closed cycle liquid He cryostat (Model - CSS 100/202, Make – Janis research Inc. USA) and cooled upto 100 K, in which the temperature was measured and controlled using "Lakeshore autotuning" temperature controller. A continuous beam of 532nm from Nd:YAG laser (Model Casix – 30 mW, LDC-1500) was used as the excitation source. Focused beam of area 0.33 cm^2 (intensity 90 mW/cm^2) was used for the study. The emission spectra were recorded employing spectrometer USB 2000 (Technosource International INC.).

Dark and photo conductivities were measured using source measuring unit (SMU-123X KIETHLY) in the voltage range 0-5 V at room temperature. Low temperature photoconductivity study was performed by using a closed cycle liquid helium cryostat (Model-REF-396/D22, Make-Helix Technology Corporation, USA), in which "Lakeshore321 autotuning" temperature controller controlled the temperature. The variation in photoconductivity, with wavelength, was measured by selecting the wavelength of the incident light by means of a monochromator (Oriel, Stratford CT 06497; Model-77200) from 280 nm to 965 nm. Electrical contacts were given through two patches of silver paint, in the form of two end contacts, with a separation of 5 mm, such that the film area for the measurement was 5 mm^2. Output from the sample was taken using magnanin wire contacts, given to the silver paint electrodes. Illumination was given to the 5 mm^2 area using halogen bulb (100 mW/ cm^2) for 60 sec and I-V characteristics were measured. Photoconductivity was measured under illumination time of 60s.

3.3 Result and discussion

3.3.1 X-ray diffraction analysis

Figure 3.1 depicts the XRD pattern of IS 100 series of samples. Two peaks of γ-In_2Se_3 (JCPDS card: 23-465) were seen at 2θ=29.7 and 2θ=38.2, along (201) and (103) planes respectively, for 28IS 100 (Fig 3.1). However in the case of 42IS 100 and 56IS 100, there was only one peak, corresponding to 2θ=29.6 along (201) plane. Average grain size of the samples was calculated using Debye Scherrer's formula [13] (see section 1.10.2), and the values were found to be 147 Å, 210 Å and 208 Å for samples 28IS 100, 42IS 100 and 56IS 100 respectively, indicating an increase in grain size with the increase in indium concentration. However further increase of thickness did not show any significant effect.

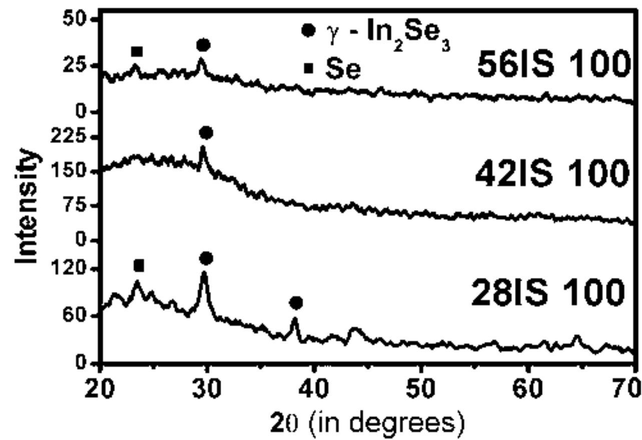

Figure 3.1: X-ray diffraction spectra of 28IS 100, 42IS 100 and 56IS 100.

3.3.2 Optical studies

(a) Optical absorption

Optical absorption spectra of 28IS 100, 42IS 100 and of 56IS 100 revealed that all the samples exhibited a strong absorption in the range 500 nm – 800 nm. But 56IS 100 showed additional absorptions in the ranges 620 nm – 800 nm and 865 nm – 990 nm (Fig.3.2). From the spectra (Fig. 3.2), one could see that the absorption edge was not so sharp, indicating that, in this film, there were strong levels existing below the conduction band [14, 15, 16].

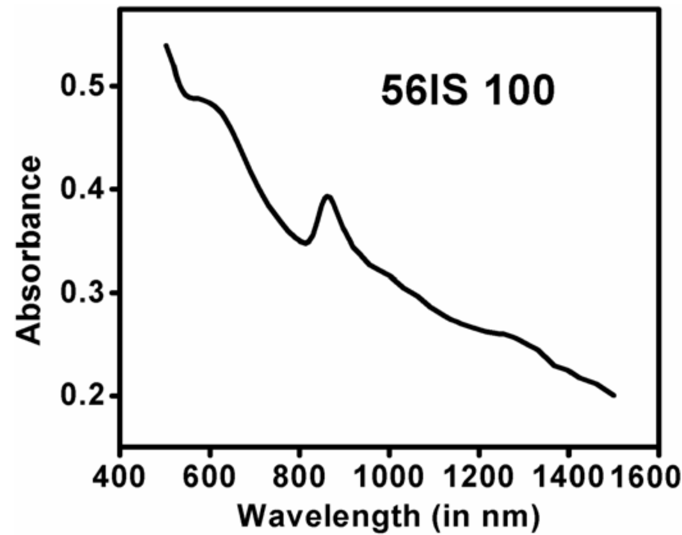

Figure 3.2: Absorption spectra of 56IS 100.

The optical band gap (E_g) of the samples was determined by extrapolating the straight line portion of $(\alpha h\upsilon)^2$ versus $h\upsilon$ plot to $\alpha = 0$ [14], where $h\upsilon$ is the incident photon energy and α is the absorption coefficient, determined from the absorption spectra. Band gap of all the samples was found to be 1.84 eV, which was very close to the reported value (1.8eV) for γ-In_2Se_3 [17]. Figure 3.3 shows the $(\alpha h\upsilon)^2$ versus $h\upsilon$ plot of 56IS 100. Extrapolating the other three straight line portions of $(\alpha h\upsilon)^2$ versus $h\upsilon$ plot (of 56IS 100) to $\alpha = 0$, one could obtain three activation energies at 1.32 eV, 1.46 eV and 1.17 eV. This could be attributed to defects levels, present in the forbidden energy gap [14]. The strong absorption in the range 620 nm-800 nm was assumed to be due to the absorption from valance band to the defect level at 1.46 eV (level-A), above the valance band (Fig. 3.3). For the samples with low indium concentration (28IS 100 and 42IS 100) we could observe only band-to-band absorption. As the indium concentration increased (56IS 100) more defects were introduced in the forbidden region, as observed from figure 3.3.

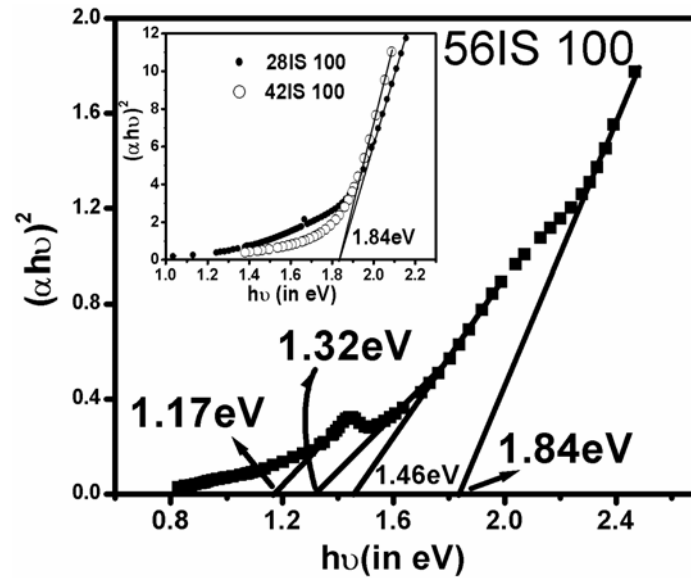

Figure 3.3: Shows the $(\alpha h\nu)^2$ versus hν plot of 56IS 100. Inset shows $(\alpha h\nu)^2$ versus hν plot of 28IS 100 and 42IS 100.

(b) Photoluminescence

Photoluminescence spectra of 28IS 100, 42IS 100 and 56IS 100, recorded at 100 K, are shown in figure 3.4. All the samples exhibited a strong emission at 802 nm, (of energy 1.55 eV) with maximum intensity for the sample 28IS 100. As the In concentration increased, the intensity of the emission decreased sharply. In addition to the emission at 1.55 eV, 28IS 100 showed another emission at 1.1 eV. The emission at 1.55 eV was attributed to the transition from conduction band to a radiative recombination center (level-B) at 290 meV, above the valence band [18]. The emission at 1.1 eV (in 28IS 100) was due to the transition from conduction band to a luminescence center (at 740 meV above the valance band) created by the cation vacancy. There was a good chance of cation

vacancy in 28IS 100, and as it had the lowest concentration of indium and on increasing the indium concentration, this emission disappeared. This very well supported our argument.

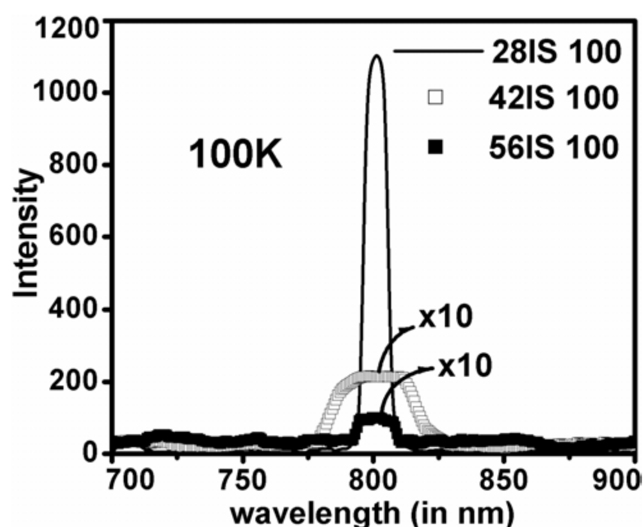

Figure 3.4: Photoluminescence spectra of 28IS 100, 42IS 100 and 56IS 100. Emission of 42IS 100 and 56IS 100 were multiplied by a factor of 10.

From the optical absorption spectrum of 56IS 100 (Fig. 3.2), one could observe a strong absorption in the range 880 nm-865 nm, corresponding to an energy 1.17 eV (Fig. 3.3). This energy (1.17 eV) was exactly coinciding with the energy difference between the levels at 290 meV (level-B) and 1.46 eV (level-A) and hence this was attributed to the excitation of carriers from the level-B to level-A. The absorption in the range 865 nm – 990 nm might be due to the transition from valance band to the defect level situated at 1.32 eV above the valance band (level-C).

3.3.3 Photoconductivity studies

(a) Room temperature photoconductivity

Conductivity of the samples, under dark and illuminated conditions, were measured at room temperature. Photosensitivity $[(I_l-I_d)/I_d]$, (ie, the ratio of difference between photocurrent and dark current to the dark current) and sheet resistance of the samples were measured and tabulated in Table 3.1. Sample 28IS 100 had the maximum photosensitivity of 24 and as the indium concentration increased, the photosensitivity decreased and became negative for 56IS 100 [Fig. 3.5(c)].

Table 3.1: Variation of photosensitivity and Sheet resistance with indium concentration

SL.	Sample identity	Photo-sensitivity	Resistance (Ω)	Band gap (eV)
1.	28IS 100	24	1 G	1.84
2.	42IS 100	1	5 M	1.84
3.	56IS 100	- 0.1	9 k	1.84

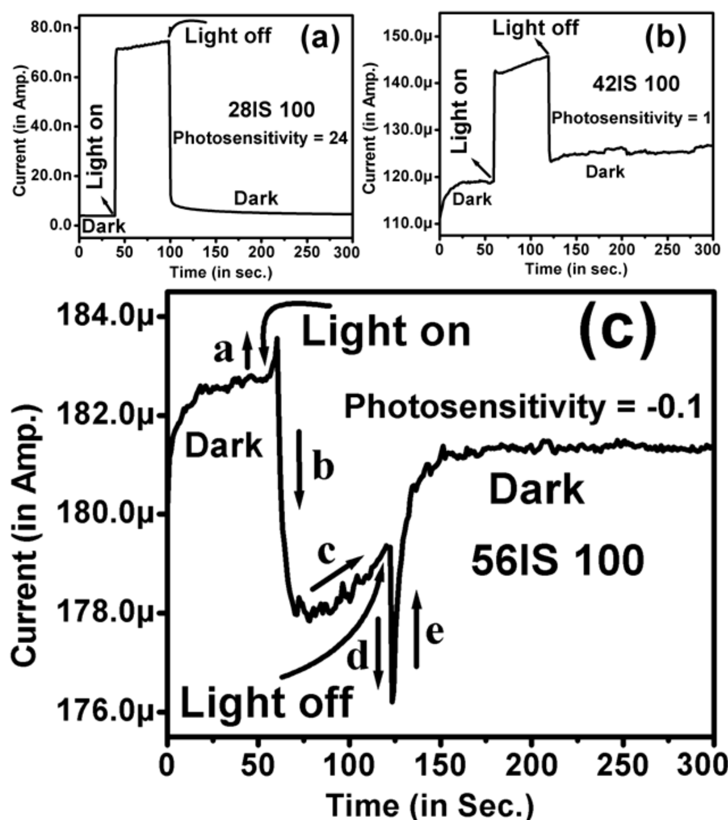

Figure 3.5: Shows the photoconductivity curve of (a) 28IS 100 (b) 42IS 100 and (c) 56IS 100.

From PL study, it was identified that there was a defect due to cation vacancy in 28IS 100 at 1.1eV below the conduction band. This vacancy might be acting as an "electron trap" in 28IS 100, reducing the electron concentration very much in this sample. This was clearly supported by the very high sheet resistance (~ 1G ohm) of the sample. Because of the electron trap, majority carriers were trapped protecting the minority carriers during illumination, resulting in an increase of the photoconductivity. Increase in indium concentration (42IS 100) eliminated

this level, leading to the decrease in resistance and photoconductivity (Table 3.1).

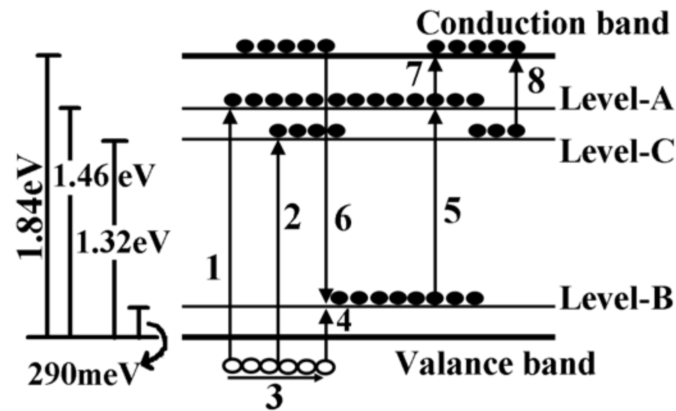

Figure 3.6: Shows the assumed band structure of 56IS 100.

Figure 3.5(c) shows the photoconductivity curve of the sample 56IS 100, which depicts the negative photoconductivity, and this is explained using figure 3.6. When the light was turned on, electrons from the valance band were excited to the levels A and C, [process (1) and (2)], situated below the conduction band, as these were not fully occupied by electrons. This resulted in the increase in concentration of holes in valence band leading to higher photoconductivity (process 3), represented by the initial increase in conductivity as the light was switched on [path "a" in Fig. 3.5(c)]. Now these holes undergo recombination through the level-B (process 4) leading to a sudden decrease of minority carriers. Process 4 and excitation of electrons from the level-B (process 5) creates more electron vacancies at level-B, which attracted electrons from the conduction band (process 6). Trapping of exited electrons was already taking place at levels A & C, as explained earlier. These three processes caused the decrease of conductivity below dark level.

After the sharp decrease of conductivity initially, one could observe a slow increase in conductivity [path "c" in Fig 3.5(c)]. This might be due to the saturation of the upper levels (levels A and C), as light falls for more time. As a result of this, some of the excited electrons might be going to the conduction band, causing the increase in conductivity. When the light is turned off, the "carrier generation process" was abruptly stopped while the "carrier loss process" was still going on, resulting in the sudden decrease of the conductivity [path "d" in Fig 3.5(c)]. But electrons were slowly released, due to thermal release, from the upper levels A and C, to the conduction band [process (7) & (8)], increasing the conductivity back to the dark level slowly [path "e" in Fig. 3.5(c)].

On analyzing the PL spectra (Fig. 3.4) one could see that the intensity of PL emission decreased with increase in In concentration. Corresponding to this, the photosensitivity also decreased. PL emission at 1.55 eV was due to the capture of electrons from conduction band by the recombination center (level-B). For 28IS 100, levels A and C were absent and hence more photo-excited carriers were available in the conduction band on illumination. These electrons were then captured by level-B for recombination. Naturally this transition from conduction band to level B resulted in high intensity PL emission. But on increasing indium concentration, more electrons were available in the conduction band and hence the level-B was remaining more or less filled in 56IS 100. This resulted in less number of transitions from conduction band to level-B, with a drastic reduction in PL emission.

Figure 3.7 shows the photo response of all the samples ("Photo-current" versus "Wavelength" plot). For 28IS 100 and 42IS 100 [Fig. 3.7(a) and (b)] one could observe that the photocurrent had a peak around 800 nm, corresponding to an energy ~ 1.55 eV. But for 56IS 100, (Fig. 3.7(c)) this peak disappeared and a broad peak appeared around 860 nm and another at 950 nm, corresponding to energies ~1.44 eV and 1.31 eV respectively. Photocurrent of the sample 28IS

100 was higher than the dark current for all wavelength. But in the case of 42IS 100, photocurrent was higher than dark current upto 700 nm (1.77 eV) and for lower wavelengths, photocurrent became lower than dark current. But in the case of 56IS 100, photocurrent was lower than dark current for the entire range of wavelengths.

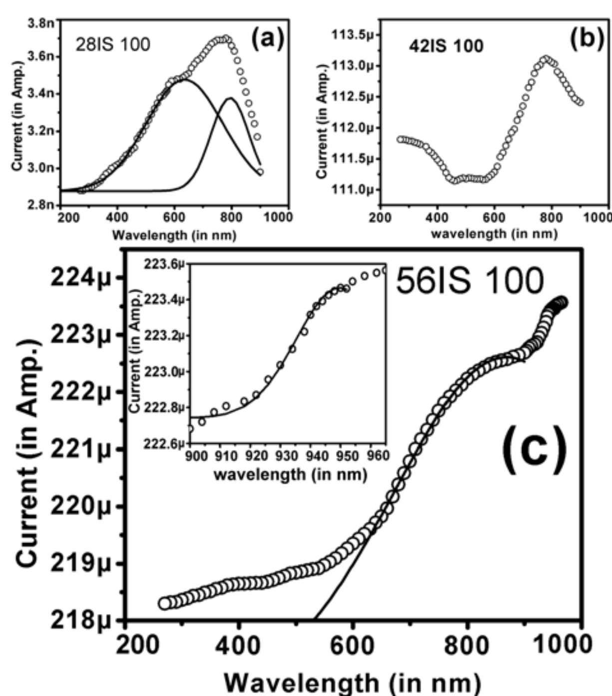

Figure 3.7: Shows the photo-response spectra of (a) 28IS 100 (b) 42IS 100 and (c) 56IS 100. Inset in Fig. 7(c) shows the peak of 56IS 100 at 950nm.

The photocurrent peak corresponding to ~800 nm suggested that the level at 1.55 eV was contributing to the photocurrent in the case of 28IS 100 and 42IS 100. It is worth mentioning here that the PL emission was also at this energy, suggesting that the electrons trapped at the level B was excited to the conduction

band, and these were enhancing the photoconductivity very much. However the photocurrent of sample 56IS 100 did not show a peak at this energy, indicating that no electrons were reaching the conduction band from the level-B. This is quite natural as there were two trap levels (A & C) near the conduction band for this sample. Interestingly, this sample had a strong peak in the photocurrent at 950 nm. This indicated that the transition was from the valance band to level-C (process 2 in Fig. 3.6), creating holes in the valence band and these holes were helping the enhancement of the photoconductivity. There was another peak at ~860 nm in the case of this sample, corresponding to energy of 1.47 eV. This was due to the excitation of carriers from valence band to level-A. These two peaks (one at 1.31 eV and the other at 1.47 eV) clearly proved beyond doubt that in 56IS 100 there was no possibility of electrons reaching the conduction band, due to the presence of the two levels A & C. This, along with the presence of the recombination center (level-B) was the reason for the negative photoconductivity of this sample.

(b) Low temperature photoconductivity

To study the effect of electron traps in 56IS 100 (Levels A and C), low temperature photoconductivity studies were carried out from 20 K to room temperature. Figure 3.8(a) shows the photoconductivity spectrum of 56IS 100 at 20 K. Here we observed only positive photoconductivity. At low temperatures, levels A and C are almost filled, as there was no thermal release of electrons at this temperature. Hence, on illumination, photo excited electrons directly reached the conduction band resulting in the increase of photoconductivity. Holes in the valance band might be still recombining at recombination center (level-B). Some of the electrons from the conduction band might be attracted to recombination center. But this might be very low in comparison with the photo-excited carriers. When light was switched off, electron excitation was stopped. But the recombination at level-B continued, resulting in sudden decrease in conductivity [path “D” in Fig. 3.8(a)]. Moreover the release of electrons from

the traps A & C was not taking place. This release was predominant only at temperature greater than 290 K [path "E" in Fig. 3.8(b) and (c)]. On increasing the temperature from 20 K to 300 K, the positive photoconductivity decreased gradually and became negative photoconductive above 300 K, ie at room temperature (Fig. 3.8(d)). As the temperature became greater than 300 K, electron vacancies were created in the traps levels A and C and hence photo excited electrons were trapped in these traps prohibiting them from reaching the conduction band.

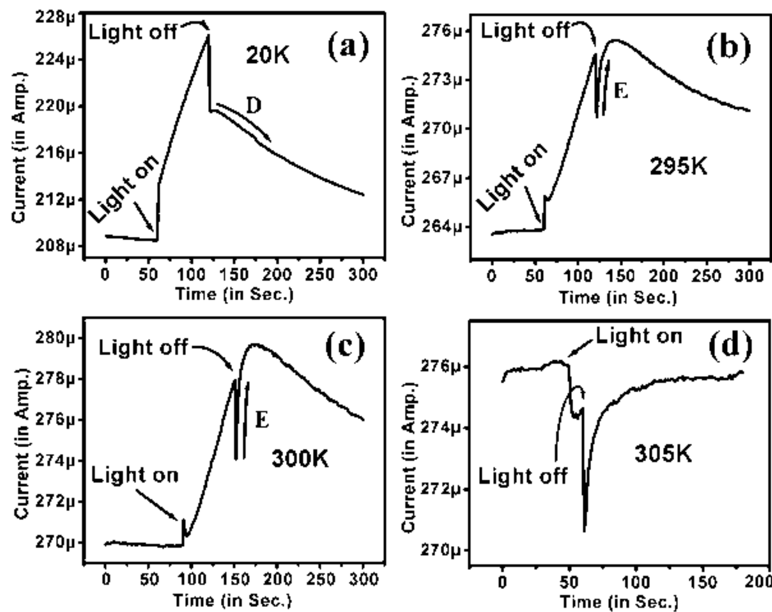

Figure 3.8: Shows the photoconductivity curve of 56IS 100 at different temperatures (a) 20K (b) 295K (c) 300K and (d) 305K.

3.4 Conclusion

γ-In_2Se_3 can show negative photoconductivity even at room temperature. This mechanism is due to (i) the trapping of photo-excited electrons at levels 1.46 and 1.32 eV above valance band (ii) destruction of minority carriers (holes), via recombination at recombination center (RC), 290 meV above valance band and (iii) the capture of conduction band electrons at RC during illumination. At low temperatures, no thermal release of electrons occurs from the levels 1.46 and 1.32 eV and the levels remained more or less filled. This allows photo-generated carriers to reach conduction band, resulting in positive photoconductivity.

References

1. A. Sh. Abdinov and A. G. Kyazym-zade, Sov. Phys. Semicond. **10** (1976) 47.
2. R. A. Hopfel, Appl. Phys. Lett. **52**(10) (1988) 801.
3. M. J. Chou, D. C. Tsui and G. Weimann, Appl. Phys. Lett. **47** (1985) 609.
4. Roger Newman, Phys. Rev. **94** (1954) 278.
5. L. Johnson and H. Levinstein, Phys. Rev. **117** (1960) 1191.
6. Claude M. Penchina, J. S. Moore and N. Holonyak Jr. Phys. Rev. **143** (1965) 634.
7. N. V. Joshi, Leticia Mogollon, J. Sanchez and J. M. Martin, Solid State Commun. **65** (1988) 151.
8. B. A. Akimov, V. A. Bogoyavlenskiy, L. I. Ryabova, V. N. Vasil'kov, Phys. Rev. B **61** (2000) 16045.
9. Br. Petretis and M. Balciuniene, J. Non-Cryst. Solids **311** (2002) 42.
10. F. Stockmann, Z. Physik **143** (1955) 348.
11. M. C. P. Chang and Claude M. Penchina, Phys. Rev. B **4** (1971) 1229.
12. K. Bindu, M. Lakshmi, S. Bini, C. Sudha Kartha, K. P. Vijayakumar, T. Abe and Y. Kashiwaba, Semicond. Sci. Technol. **17** (2002) 270.
13. B. D. Cullity B.D, Elements of X-ray Diffraction (Reading, M A: Addison-Wesley, 1978), p. 170.
14. J. I. Pankove, Optical process in semiconductors (Dover Publications, Inc. New York 1971), p. 64, 34.
15. E. J. John and H. Y. Fan, Phys. Rev. **139** (1965) A1991.
16. R. Sreekumar, R. Jayakrishnan, C. Sudha Kartha and K. P. Vijayakumar, J. Appl. Phys. **100** (2006) 33707.
17. C. Julien, A. Cheavy and D. Siapkas, Phys. Status Solidi A **118** (1990) 553.
18. M. Balkanski, C. Julien, A. Chevy and K. Kambas, Solid state commun. **59** (1986) 423.

CHAPTER 4

Low temperature material synthesis and ion beam mixing of In/Se bilayer systems using swift heavy ion irradiation

CHAPTER 4

Part A

Online interface mixing study using swift heavy ions: An attempt

Abstract

This part of the chapter summarises the attempt to study on-line/in-situ ion beam mixing between In/Se bilayer system using 'Rutherford Backscattering Spectroscopy' with the help of 40 MeV silicon ions. Deviating from conventional RBS using 3 MeV He ions, 40 MeV Si ions was used to study the mixing between In/Se bilayer system. On-line RBS study revealed the existence of threshold fluence required for mixing to take place between In and Se. Conventional RBS study carried out using 3 MeV He ions proved that mixing between In and Se takes place at a fluence of $1x10^{13}$ *ions/cm*^{2}.

4.1 Introduction

Rutherford backscattering spectroscopy (RBS) is one of the most useful tools to study the mixing between bilayer systems induced by low energy (of the order of few hundred keV) and high energy (greater than few tens of MeV) heavy ion irradiations [1]. It can also provide information about the composition of multi-elemental samples, thickness of thin films, depth-profile of elements and can also be used to identify unknown elements in the material [2]. In modern conventional RBS analysis, a collimated beam of energetic ions, usually He or H ions of energy 2-3 MeV, will be used to impinge on the sample at off normal incidence (incident angle less than 10 degree, to avoid channeling). The backscattered ions from the sample are usually detected with the help of particle detector (normally a Si surface barrier detector). The signal is further amplified, shaped and finally analysed using a multi-channel analyser, to obtain the RBS spectra. Main advantages of RBS are that it is fast, simple, easy and non-destructive. Major weaknesses of this technique are the following: this is not sensitive to lighter elements, has poor mass resolution for heavier elements and not able to provide information on the chemical state of the element. In order to overcome these difficulties several techniques were developed. By using non-Rutherford elastic scattering, we can increase sensitivity towards lighter elements such as C, N and O. In this technique, the energy of the probing ions was decreased so as to increase the scattering cross-section from the lighter elements. Resonant scattering was also employed to increase the scattering cross section, thereby enhancing the sensitivity of lighter elements. Cameron [3] and Mezey et al. [4] demonstrated investigation of O composition in thin oxide layers. In these cases, in addition to the coulombic force, nuclear force is also involved in the scattering. To improve mass resolution for heavier elements, heavier ions with higher energies were used as probe beam [5]. This technique improved the depth resolution also.

High energy heavy ions (swift heavy ions), which are having velocities

comparable to the innermost orbital electrons (~ 2.2×10^8 cm/sec), lose energy to the material in two ways, (i) electronic energy loss $(dE/dx)_e$ (ii) nuclear energy loss $(dE/dx)_n$. Electronic energy loss is a secondary process in which the projectile ions first imparts their energy to the lattice electrons and this energy is dissipated to the lattice through electron-phonon interactions. But in the case of nuclear energy loss, the ions give energy directly to the atomic nuclei via elastic collisions. However for swift heavy ions, the nuclear energy is very much negligible as compared to the electronic energy loss. Swift heavy ions can create point defects [6], columnar defects, an amorphous track or a perturbed atomic distribution along its path [7] and even an interface mixing, if it is passing through a layered system [8, 9]. Swift heavy ions are now intensively used by material scientists for modifying optical, electrical and structural properties of materials [10, 11, 12]. It is also used for interface mixing [8, 9], novel phase formation [13] and for material characterizations such as 'elastic recoil detection analysis (ERDA)' [14]. Ion beam mixing using swift heavy ions was first demonstrated by Dufour et al. [15] in 1993. Since then, several studies have been carried out in different systems such as metal/metal [16, 17], metal/semiconductor [18, 15, 19], metal/insulator [20] and metal/semi-metal [21]. On-line mixing study using elastic recoil detection analysis (ERDA) with 230 MeV Au ions in CuO/glass interface was demonstrated by Avasthi et al. [14]. In the present study, on-line mixing between In/Se interface using backscattering spectroscopy was attempted with 40 MeV Si ions.

4.2 Experiment

Thin film of selenium with thickness ~ 150 nm (measured using stylus thickness profiler Dektak6) was first deposited on to a glass substrate, using chemical bath deposition technique [22], over which 56 nm of In was vacuum evaporated (resistive heating) from Mo boat at a pressure of 2×10^{-5} mbar. Thickness of In was controlled using a quartz crystal monitor. These samples were then loaded in the ladder which is attached to a goniometer in 'general purpose scattering

chamber (GPSC)' at Inter University Accelerator Centre, New Delhi. A collimated beam of 40 MeV Si ions with 2 mm diameter was allowed to fall on the sample at an angle of 45° to the sample normal and the scattered ions were detected at an angle 90° to the backscattering geometry (Fig. 4.1). The scattered ions were analysed with 'Si surface barrier' detector located about 20 cm from the target [at solid angle 5.7 msr]. Energy resolution of the detector was 20 keV. Experiment was conducted at a pressure of $2x10^{-6}$ mbar. System calibration was done using the backscattering signals from Si wafer and In, and found each channel corresponding to energy of 7.48 keV. The electrical pulses generated in the detector was amplified, shaped and finally analysed by a multi-channel analyzer (MCA). MCA is an electronic system which converts the electrical pulses to digital signals, sorts and displays the signal on the screen in the form of 'counts' versus 'channel number' scale. During the backscattering experiment, the beam current was kept constant at 12 nA.

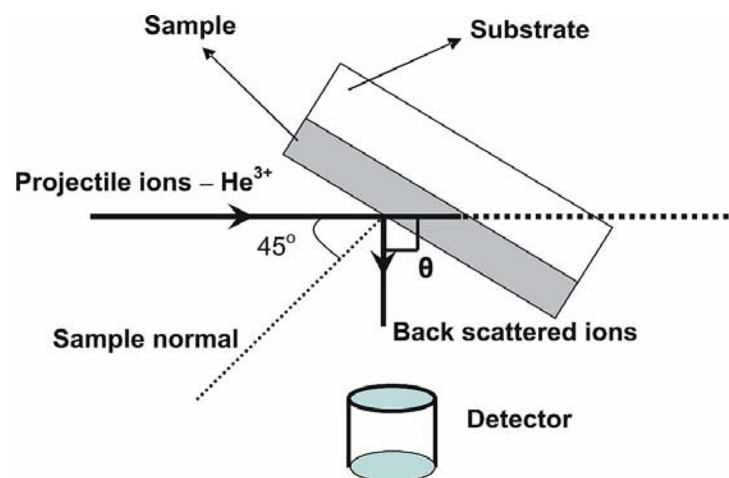

Figure 4.1: Schematic arrangement of backscattering geometry of He ions from the sample. θ is the backscattering angle.

Backscattered ions were recorded for five different doses, ranging from $1\mathrm{x}10^{11}$ to $1\mathrm{x}10^{13}$ ions. In/Se bilayer system was also irradiated using 40 MeV Si ions with a fluence of $1\mathrm{x}10^{13}$ ions/cm^2 at room temperature over an area of 1 cm^2 (by using an electromagnetic scanner). X-ray diffraction measurements on pristine and irradiated samples were carried out by varying 2θ from 10° to 60° with Cu K_α radiation (λ = 1.5405 Å), employing Rigaku (D.Max.C) X-ray diffractometer. RBS measurements were done with the help of 3 MV Pelletron accelerator (Model - 9SDH2). 3 MeV He^{2+} ions were used for RBS measurement, with an angle of incidence 10^0. A silicon surface barrier detector, placed at 160° in back scattering geometry, detected the scattered ions. Detector resolution was 20 keV and solid angle was 1msr. RBS analysis was performed with GISA simulation [23].

4.3 Principle of Rutherford backscattering technique

RBS spectroscopy is a simple technique which analyses the energy of the backscattered ions from material and obtains information about various aspects of the sample. As the energetic projectile ion pass through the material, it looses energy along the path and is scattered back by collisions with the atoms in the material. The collisions between the projectile ions and the target atom can be described as elastic collisions between two isolated particles. The energy of the projectile after collision, E can be expressed in terms of energy before collision E_o in terms of kinematic factor K as [24],

$$E = K * E_o \tag{4.1}$$

where K is expressed as,

$$K = \frac{\left\{\left[1-\left(\left(M_1/M_2\right)\sin\theta\right)^2\right]^{\frac{1}{2}} + \cos\theta\right\}^2}{\left\{1-\left(\left(M_1/M_2\right)\sin\theta\right)^2\right\}^{\frac{1}{2}}} \tag{4.2}$$

where M_1 and M_2 are the masses of projectile and target atom respectively, and θ the scattering angle. At this angle the scattered ions are detected by a solid state detector that subtends a small solid angle **Ω**. From the known values of M_1, E_o and θ one could identify the unknown element in the material with mass M_2. The number of counts, [A] registered by the detector is given as,

$$A = Q \cdot \Omega \cdot N \cdot t \cdot \sigma(E_o, \theta) \tag{4.3}$$

where 'Q' is the number of ions incident on the sample, 'N' the density of the atoms in the material, 't' the thickness of the sample and $\sigma(E_o, \theta)$ the scattering cross section for scattering into a solid angle Ω at a scattering angle θ. It is given as,

$$\sigma(E_o, \theta) = \left[\frac{Z_1 Z_2 e^2}{4E_o}\right]^2 \frac{4}{\sin^2\theta} \cdot K \tag{4.4}$$

where Z1 and Z2 are the atomic numbers of the projectile ion and the target atom respectively. The equation 4.3 shows that from the known values of Z1, Z2, Ω, E_o, θ and numbers of incident (Q) and detected ions (A), we can get the density (N.t) of the material. From this, we can measure thickness of the material. If the material is a compound with elements A and B in the atomic ratio $A_m B_n$, the backscattering spectra would record two signals corresponding to the heavy atom A and the light atom B, as sketched in figure 4.2. Using equation 4.3, we can find the composition of the compound $A_m B_n$ as,

$$\frac{m}{n} = \left[\frac{A_A}{\sigma_A(E_o, \theta)} \Big/ \frac{A_B}{\sigma_B(E_o, \theta)} \right] \tag{4.5}$$

where A_A and A_B are the area under the curves corresponding to element A and B respectively and $\sigma_A(E_o,\theta)$, $\sigma_B(E_o,\theta)$ are the scattering cross-section of elements A and B respectively, which can be calculated using equation 4.4.

As the ion passes through the material, it loses energy by scattering. Hence the energy of the scattered ion depends on the kinematic factor as well as on the depth from the sample surface where the scattering occurs. The projectile ions lose energy to reach a particular depth and after scattering, it again loses energy to come out of the sample. Thus backscattered ions contain the information about the depth also. Figure 4.2 shows the schematic picture of backscattering spectra of ions of mass M_1 from a compound thin film containing two different masses M_2 and M_3 , deposited on a low-mass (M_4) elemental substrate ($M_2 > M_3 > M_4$). Energies of the backscattered ions from various depths and various atoms are marked by arrows.

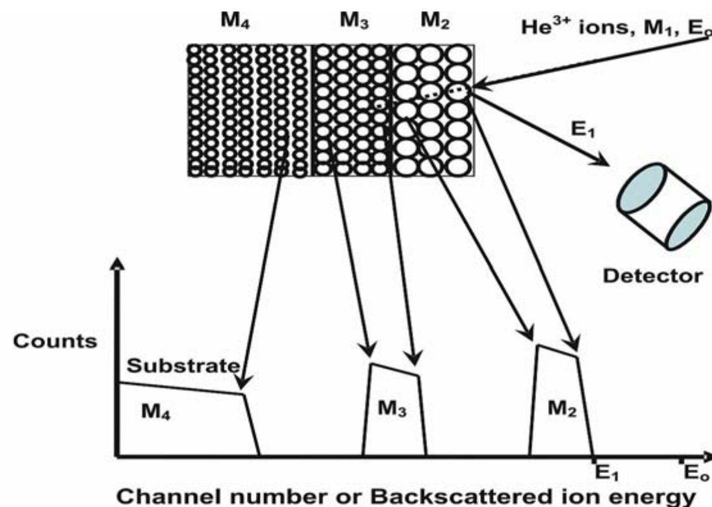

Figure 4.2. Schematic picture of RBS spectrum from a bilayer system with mass M_2 and M_3 on a substrate with mass M_4 ($M_2 > M_3 > M_4$), using He ions of energy E_o with mass M_1.

4.4 Discussion

Ion beam mixing (IBM) is one of the tools for synthesis of compounds using low energy ions [25] and the compound phases, in general, are achievable at relatively lower temperature in the process of ion beam mixing [18]. Advantage of IBM using high energy (≥ 1 MeV/amu) heavy ions (known as swift heavy ions -SHI) over low energy ion mixing is that, the fluence required for mixing is about 10^{13} ions/cm^2 to 10^{14} ions/cm^2, which is two to three orders of magnitude smaller, compared to low energy ion induced mixing [18]. IBM by high energy heavy ions was first demonstrated by Dufour et al. [15] and after that there has been intense research, to find the cause of mixing induced by swift heavy ions in different systems such as metal/metal, metal/Semiconductor, metal/insulator interfaces. Different techniques such as ERDA [14] X-ray reflectivity [20, 26], X-ray photoelectron spectroscopy (XPS) [21], cross sectional transmission electron microscopy (XTEM) [9], cross sectional scanning electron microscopy (XSEM) [27], GXRD [28, 29], Mössbauer spectroscopy [30], Auger electron spectroscopy (AES) [32] and Rutherford backscattering spectroscopy were used to detect the interface mixing in the specimen. Among these, most commonly used technique is RBS because of its simplicity in analysis and nondestructive nature. It can also give depth-wise information. The techniques mentioned above such as XPS and AES, employ ion sputtering to remove the surface layer to get the depth-wise information, whereas XTEM needs sample preparation on grids and XSEM needs a metal coating (Au) over the sample, destroying the sample.

To study IBM by conventional RBS measurements, we have to again load the samples in a scattering chamber. The pressure inside the chamber is of the order of $1x10^{-6}$ mbar., created by pumping with the help of a turbo molecular pump. Again, we have to get He ions of energy 2-3 MeV from a particle accelerator. All these equipments are very expensive and the experiment consumes time also. If the RBS measurements can be done during the irradiation experiment itself using SHI, one can avoid using the ‘million-dollar’ experimental set-up required

for conventional RBS. This can save the precious time too. For online RBS measurements, we require few additional geometrical arrangements of detectors and analyzing equipments.

In the present study, the samples were analysed using online RBS with 40 MeV Si ions. Geometries of angle of incidence (45°) of the ion beam and the scattering angle (90°) are displayed in the schematic picture (Fig. 4.1). In/Se bilayer was irradiated using 40 MeV Si ions of different doses, ranging from $1x10^{11}$ ions to $1x10^{13}$ ions and backscattered ions were detected using a 'Si surface barrier detector' and the backscattering spectra were recorded. Figure 4.3 shows the backscattering (BS) spectra of In/Se system irradiated with different doses of $3x10^{12}$ to $6x10^{12}$ ions. We could not find any mixing between In and Se until a dose of $6x10^{12}$ ions was used as evidenct from the spectra.

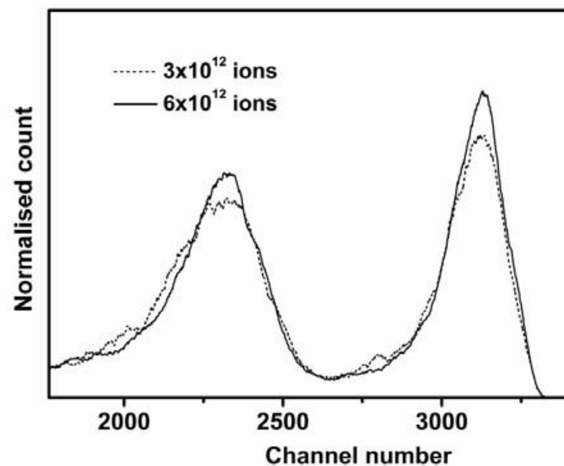

Figure 4.3: Rutherford backscattering spectra of In/Se bilayer system recorded using 40 MeV Si ions with a dose of $3x10^{12}$ and $6x10^{12}$ ions.

Figure 4.4 shows the result of BS analysis with doses $1x10^{11}$ and $1x10^{13}$ ions. In

this, one could find mixing between In and Se layers. We can observe from the BS spectra recorded with $1x10^{13}$ ions that, the counts of In and Se peaks reduced and Se peak shifted towards higher energy side or higher channel number. This represents the mixing between In and Se layers. This study also revealed that the threshold fluence required for mixing to take place between In and Se was around $1x10^{13}$ ions/cm^2 for 40 MeV Si ions.

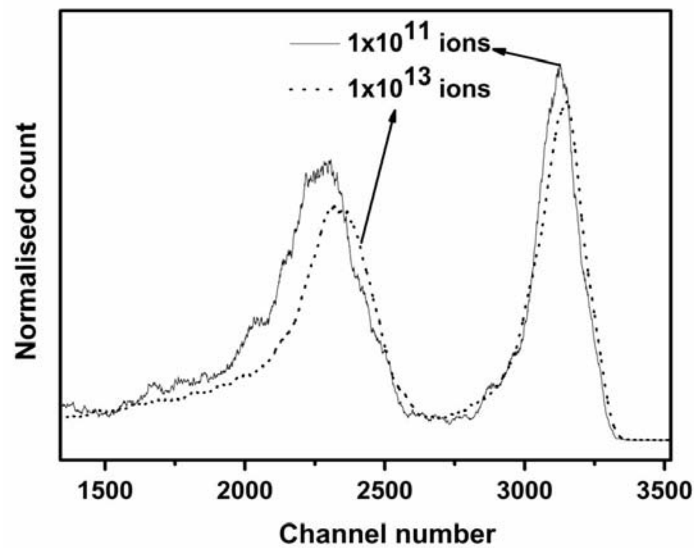

Figure 4.4: Rutherford backscattering spectra of In/Se bilayer system recorded using 40 MeV Si ions with a dose of $1x10^{11}$ and $1x10^{13}$ ions.

Figure 4.5 shows the RBS spectra of pristine and irradiated In/Se system (fluence $1x10^{13}$ ions/cm^2) recorded by conventional RBS using He ions of energy 3 MeV. The spectra revealed the mixing between In and Se layers. We can observe an increase in full width at half maximum (FWHM) of both the Se and In peaks on irradiation with $1x10^{13}$ ions/cm^2. FWHM of Se and In were increased to 17 keV and 27 keV from 16 keV and 20 keV respectively. Also a

shift towards the higher energy edge [or channel number] of Se peak and a shift towards the low energy edge or channel number by the In peak clearly shows the mixing between In and Se layers.

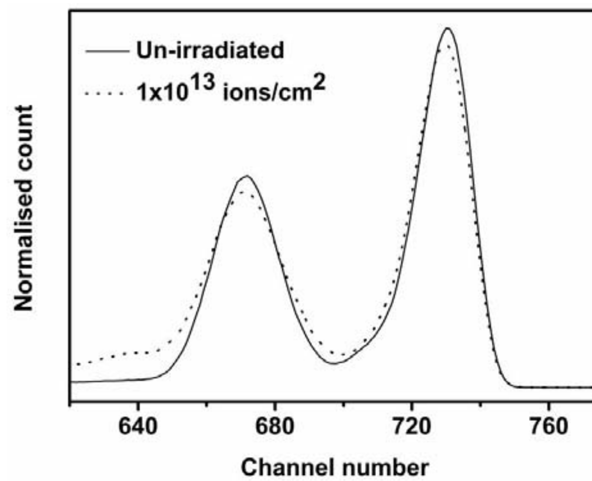

Figure 4.5: Rutherford backscattering spectra of unirradiated and irradiated (using 40 MeV Si ions of fluence $1x10^{13}$ ions/cm^2) In/Se bilayer system recorded using 3 MeV He^{2+} ions.

From the RBS spectra (Fig. 4.4 and Fig. 4.5) recorded using 40 MeV Si ions and 3 MeV He ions respectively, one could observe that the mass resolution of the spectra recorded using 40 MeV Si ions was higher than that with 3 MeV He ions. In the case of spectra recorded using 3 MeV He ions, the peaks of In and Se were separated only by 60 channels (one channel = 2.94 keV); but with 40 MeV Si ions, the peaks were separated by 845 channels (one channel = 7.48 keV). This shows the resolution is greater for the spectra, recorded using 40 MeV Si ions. When one uses heavier ions with higher energies, there is enhancement of the scattering cross section, leading to higher mass resolution [33]. The geometry of angle of incidence of probing ions and the scattering

angle plays a good role in enhancing the depth resolution. Here we have selected an angle of incidence as 45° and scattering angle 90° (Fig. 4.1). Increasing the angle of incidence increases the total path length that a particle traverses in the sample to reach the detector after scattering. The increase in total path length can greatly improve the effective depth resolution.

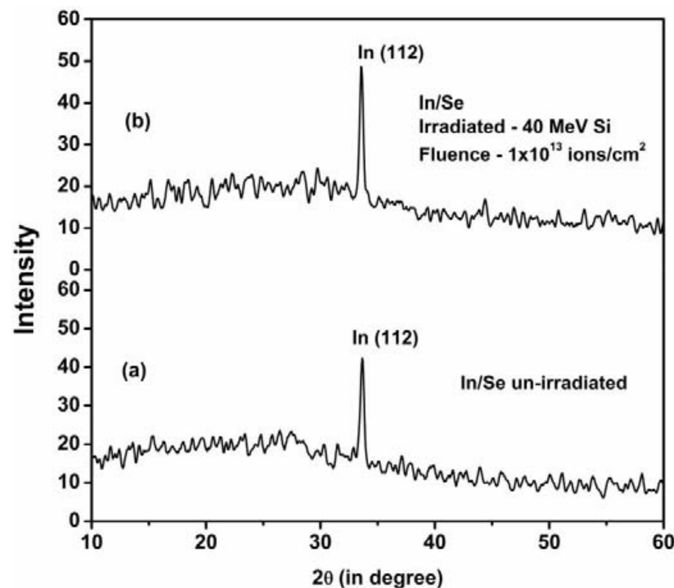

Figure 4.6: XRD pattern of (a) un-irradiated and (b) In/Se system irradiated with 40 MeV Si ions of fluence $1.05x10^{13}$ ions/cm^2.

Figure 4.6 (a) and (b) show the X-ray diffraction (XRD) pattern of In/Se system before and after irradiation. We can only observe the peak, corresponding to Indium, having reflection at $2\theta = 33.65$ from (112) plane. On irradiation with 40 MeV Si ions, an increase in peak intensity and reduction of FWHM of the In peak was observed from 0.28 to 0.25. It is to be noted that no compound formation was observed on irradiation even though we have observed mixing

between In and Se layers from RBS measurements.

Ion beam mixing in the electronic energy regime can be explained using two different models, namely (i) Coulomb-explosion model [35, 36, 37] and (ii) thermal spike model [37, 38, 39]. According to Coulomb-explosion model, as swift heavy ions passes through the material, it losses energy to the electrons in the material, by exciting the electrons and ionizing the atom. This leads to ionized cylindrical zone along the path of the ions, with a strong electronic deficiency in the centre. This creates electrostatic repulsion between the positively charged atoms in the centre resulting in an explosion-like atomic motion perpendicular to the path of ions [40]. This can lead to the formation of core with reduced atomic density, surrounded by a densified shell. This is an unstable state and the atoms try to regain or collapse back to the central part. But in the absence of recrystallisation process, there will be a highly perturbed or even amorphous latent nuclear track of few nanometers in diameter. In the case of metals and semi-metals, the conduction electrons smear out the excitation and ionization of atoms and in fact, possibility of Coulomb-explosion can be ruled out in the case of metals. Thus the 'thermal spike model' is used to explain IBM in metals and semiconductors [41, 42].

According to 'thermal spike model' the energy transferred by the SHI to the lattice electrons will be imparted to the lattice via electron-phonon coupling. This results in the heating of the lattice and generation of 'Gaussian like' temperature profile around the ions path. If the electronic energy deposited by the SHI is sufficiently high, the temperature can rise above the melting point of the material and cylindrical molten track of few nanometers can be formed. After few tens of picoseconds, rapid quenching of the melt to ambient temperature occurs. Mixing between bilayer can occur by inter-diffusion through the molten track, if the interface of the two materials in contact melted during irradiation. It was proposed that the essential condition for the mixing to take place through the interface is that, the interface of the two layers should be in a

transient molten state [43, 7].

40 MeV Si ions lose about 5.42 keV/nm and 4.13 keV/nm as electronic energy loss in In and Se respectively [calculated using TRIM] [44]. We have observed that the threshold fluence for the mixing to take place between In/Se is around $1x10^{13}$ ions/cm^2. This can be explained in the following way: if the electronic energy deposited by SHI is above the threshold energy required to make the material molten, it creates molten tracks of few nanometer diameters (track formation occurs only if the material dependent threshold electronic energy is exceeded). As the fluence increases the track density or number of tracks increase, and overlapping of these tracks results in a uniform mixing at the interface [19].

4.5 Conclusion

Deviating from conventional RBS where one uses He ions of energy 3 MeV, we made an attempt to study IBM using 40 MeV Si ions for recording the backscattering spectra. By online RBS measurements using 40 MeV Si ions, threshold fluence for mixing to take place between In/Se bilayer systems was found out. Use of high energy heavy ions provided better mass and depth resolution. Online IBM study enabled us to get the information about the mixing very quickly and hence we could avoid the entire experimental techniques used to study the IBM induced by swift heavy ions. Threshold fluence for mixing to take place between In/Se bilayer systems was found to be $1x10^{13}$ ions/cm^2 for 40 MeV Si ions. Conventional RBS spectra recorded using 3 MeV He ions proved the mixing between In/Se bilayer.

CHAPTER 4

Part B

Single-phase InSe formation using SHI irradiation and low temperature annealing

Abstract

This part summarises the formation of single phase indium selenide at lower annealing temperature induced by 40 MeV Si ion irradiation. In/Se bilayer system was irradiated using 40 MeV Si ions and annealed at different temperatures. In the case of irradiated sample single phase indium selenide formation occurs at much lower annealing temperature as compared to the un-irradiated sample. The low temperature compound formation is explained as the inter mixing of the atoms through the damages created during SHI irradiation.

.

4.6 Introduction

Indium selenide (InSe) is a III-VI compound semiconductor, having direct band gap of 1.3 eV, which has been widely studied recently, due to its potential application as an absorber layer in photovoltaic devices [45, 46, 47]. This is mainly because of its high absorption coefficient as well as optimum energy band gap, suitable for solar energy conversion [48]. Various methods such as electrodeposition [49], flash evaporation [50], sequential evaporation [51] and co-evaporation of In and Se [52] are used to prepare thin films of this material. Usually it is difficult to produce single-phase indium selenide due to the co-existence of different phases together [53]. This difficulty is evident from the narrowness of the formation range of InSe in the phase diagram of the In-Se system [52] and there are different stoichiometric compounds such as InSe, In_4Se_3, In_6Se_7, In_2Se_3 [52, 54, 55, 56] for these two elements.

Indium monoselenide (InSe) is a layered compound [57]. The absence of dangling bonds on the surface layer (001) makes it a potential material for heterojunction devices [54, 58]. Band gap of InSe is 1.3eV, which again makes it an attractive material for solar energy conversion as an absorber layer in solar cells.

It was shown by us that single phase indium selenide films is formed only at 400°C [59]. In general, large number of studies was carried out to reduce the synthesis temperature of compound semiconductors. It is because; the substrates that are used as the backing should have the capability of withstanding high synthesis temperatures. This also restricts their application to device fabrication. Ion beam mixing (IBM) is one of the techniques by which one could obtain compound phases at relatively lower temperature and/or even at room temperature without any post annealing treatment. Novel phases of compounds with required properties can also obtained using IBM.

SHI transfers energy to the target, mostly by electronic excitation, (electronic energy loss, S_e) causing point defects [60], columnar defects or a perturbed atomic distribution [7]. In this case, the energy lost by the incident ions due to nuclear energy loss (S_n) is usually negligible. Above a certain threshold of S_e, electronic excitations induce atomic displacements in majority of materials. This can lead to mixing at the interface, if it is passing through a layered system [8, 61]. SHI irradiation can produce defects at the interface [62]. Thereafter, rearrangement of the interfacial atoms and/or short-range diffusion can cause mixing of the two components. In some cases, the latter is aided by post irradiation annealing [63, 64], during which nucleation and phase growth can occur. In the present work, the compound formation in irradiated and un-irradiated In/Se bilayer system, annealed at different temperatures, were investigated using X-ray diffraction (XRD) and optical absorption techniques.

4.7 Experiment

Thin films of selenium with thickness 150 nm were deposited on glass substrates using chemical bath deposition technique [22], over which 40 nm of In was deposited by resistive heating [pressure ~ $2x10^{-5}$ mbar], with Mo boat as the heating source. Thickness of the film was measured using stylus thickness profiler. In/Se system was irradiated using 40MeV Si ions in an area of $1cm^2$ with a fluence of $1x10^{13}$ ions/cm^2 using the 15UD Pelletron accelerator. An electromagnetic scanner was used to scan the ion beam over this area. Range of 40MeV Si ions was such that these got deposited deep into the substrate, at a depth of more than 10μm. The electronic energy loss $(dE/dx)_e$, for In and Se were 5.42 keV/nm and 4.13 keV/nm respectively for 40MeV Si ions, calculated using TRIM [44]. Irradiated samples were annealed at 50 ^oC and 100 ^oC while the unirradiated samples were annealed from 50 ^oC to 400 ^oC for one hour. Both annealings were at a pressure of $2x10^{-5}$ mbar. Before annealing the unirradiated samples at higher temperatures (≥ 100 ^oC), these were kept at 50 ^oC (at a pressure of $2x10^{-5}$ mbar.) for 1hour. The irradiated samples, annealed at 50 ^oC

and 100 ^{o}C, were named as I IS50 and I IS100 and unirradiated samples annealed at 50 ^{o}C, 100 ^{o}C, 300 ^{o}C and 400 ^{o}C were named as U IS50, U IS100, U IS300 and U IS400 respectively. The RBS spectra of unirradiated and irradiated samples were recorded using 3 MeV He^{3+} ions. 3 MV Pelletron accelerator at Institute of Physics, Bhubaneswar, India was used for generating the 3 MeV He ions. XRD studies were done in the range $2\theta = 10^{o}$ to 60°, using Cu K_{α} (λ = 1.5405Å) radiation employing Rigaku (D.Max.C) X- ray diffractometer. Optical band gaps were measured from absorption spectra recorded in the range 400nm to 900nm by employing UV-VIS-NIR spectrophotometer (Model: Hitachi U-3410).

4.8 Result and discussion

4.8.1 Rutherford backscattering analysis

Figure 4.7 shows the RBS spectra of pristine (unirradiated) and irradiated In/Se bilayer system (irradiated with 40 MeV Si ions of fluence $1x10^{13}$ ions/cm^{2}). The peak at higher channel number corresponds to indium and that of lower channel number corresponds to the selenium in the bilayer system. One could see that on irradiation with 40 MeV Si ions of fluence $1x10^{13}$ ions/cm^{2}, the lower channel number edge of the indium peak shifted towards left (towards lower channel number) and that of higher channel number edge of selenium peak shifted towards right (towards higher channel number). This is due to the migration or diffusion of indium and selenium atoms across the interface during ion beam irradiation.

On diffusion of In atoms into Se layer, the energy of the ions backscattered from In atoms from the Se layer would be less (channel number is a measure of energy of backscattered ions). Also, the energy of the backscattered ions from In layer will be higher with respect to that from the Se layer. This is the reason for the shift of lower channel number edge of In peak to lower channel number and

higher channel number edge of Se peak to higher channel number. Thus we have observed ion beam mixing between In and Se layers. Explanation for mixing between In and Se layer was discussed in detail in the previous section 4.2.4.

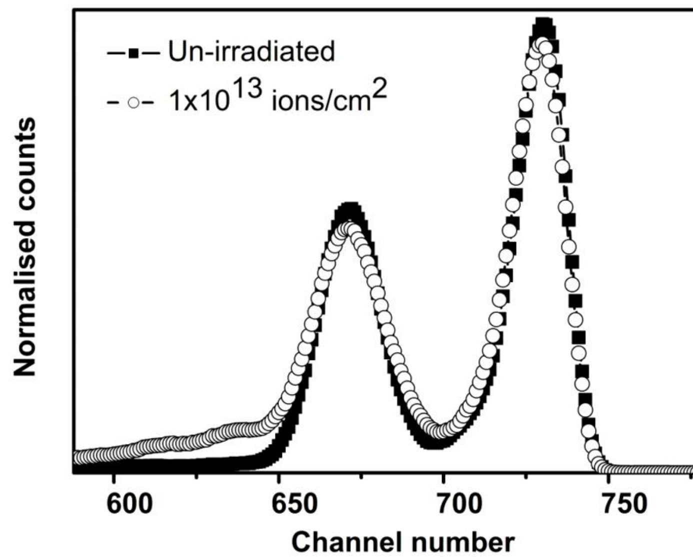

Figure 4.7: RBS spectra of un-irradiated and In/Se system irradiated with 40 MeV Si ions of fluence $1x10^{13}$ ions/cm^2.

4.8.2 X-ray diffraction analysis

Figure 4.8(a) and (b) show the XRD pattern of In/Se bilayer system before and after irradiation with 40 MeV Si ions of fluence $1x10^{13}$ ions/cm^2. The XRD peak at 2θ=33.59 was corresponding to the elemental indium in the In/Se bilayer (JCPDS number: 05-0653). Even though we have observed mixing between In and Se layer at a fluence of $1x10^{13}$ ions/cm^2 (Fig. 4.7), no compound formation was observed from the XRD analysis in as irradiated system (Fig. 4.7(b)). One could observe only a decrease in FWHM of In peak at 2θ=33.59 degree, from

0.28 to 0.25. This might be due to the clustering of In on the surface due to 40 MeV Si ion irradiation.

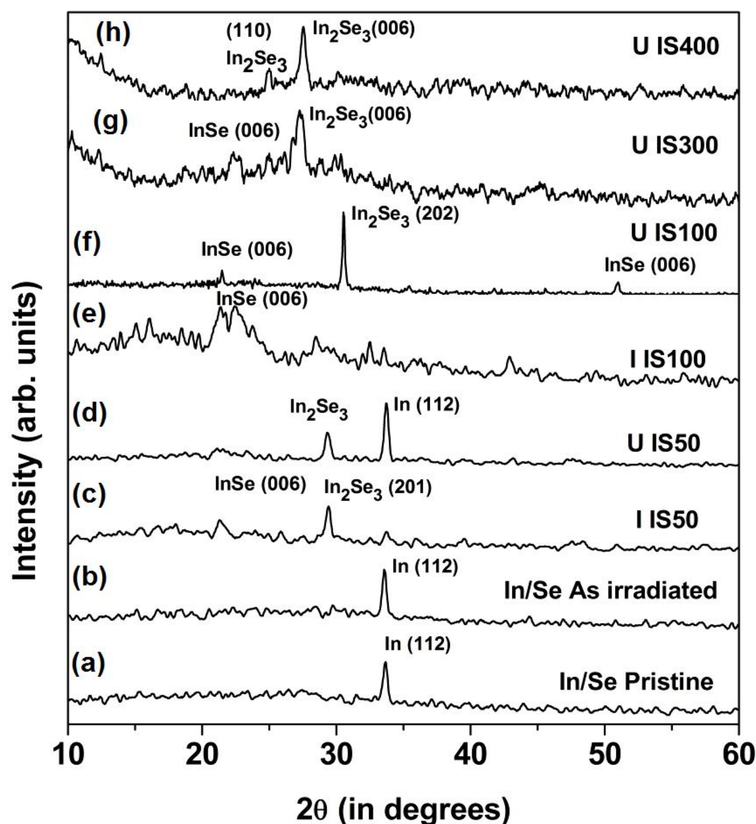

Figure 4.8: XRD pattern of In/Se system (a) pristine (b) irradiated with 40 MeV Si ions of fluence 1x 10^{13}ions/cm^2 (c) irradiated sample annealed at 50°C for 1hr. (d)unirradiated sample annealed at 50°C for 1hr. (e) irradiated sample annealed at 100°C for 1hr. and (f) un-irradiated sample annealed at 100°C for 1hr. (g) 300°C (h) 400°C respectively.

No compound formation occurred in as-irradiated In/Se system (Fig. 4.8(b)). Annealing the irradiated sample at 50 ^{o}C for one hour resulted in the formation

of In_2Se_3 and InSe phases, resulting in the peaks at 2θ=29.39 and 21.27 degree respectively (Fig. 4.8(c)). Moreover, the XRD results indicated that pure indium phase was very much reduced and this might be probably due to the good mixing taking place in irradiated annealed sample. In the case of U IS50, indium selenide formed with less vigor and there was only In_2Se_3 phase. From XRD pattern (Fig. 4.8(d)) it was also clear that there was large amount of unreacted In in U IS50. Annealing the sample I IS50 again at 100°C for one hour, resulted in formation of InSe only having orientation along (006) with less crystallinity (Fig. 4.8(e)). It was very clear that In_2Se_3 phase was almost fully lost after second annealing. In the case of U IS100, still there was mixed phase of In_2Se_3 and InSe (Fig. 4.8(f)).

Average grain size of the samples was calculated using Debye Scherrer's formula $d = (0.9\ \lambda\ /\ \beta \cos\theta)$ [65] (See section 1.10.2). Average grain size of I IS100 was ~11nm (2θ = 21.35, FWHM = 0.727) and that of U IS100 was 20nm (2θ = 30.54). We could see that in U IS300 (Fig. 4.8(g)) both InSe and In_2Se_3 existed and in U IS400 (Fig.4.8 (h)) there was only γ-In_2Se_3, with preferential orientation along (006) plane.

For irradiated sample, we obtained indium selenide at lower temperature compared to the unirradiated sample. This might be due to the enhancement in mixing. The defects (or atomic displacements which build up on either side of the interface) generated due to SHI irradiation were largely immobile. When sufficient thermal energy was supplied to the system, the atomic mobility through the defects, and across the interface enhanced [18, 62]. Even though we were getting indium selenide as a result of annealing at 100°C in unirradiated system, it was multi-phased. Even after annealing at 300°C both InSe and In_2Se_3 existed (Fig. 4.8(g)). Single phase In_2Se_3 was obtained only after 400°C annealing (Fig. 4.8(h)). Thus it was observed that annealing at 400°C was required to eliminate InSe phase in un-irradiated system.

4.8.3 Optical absorption study

Optical absorption spectra were recorded in the wavelength range 400-900 nm. In the case of U IS400 and I IS100, there was only one absorption edge. But for all other samples, in addition to the strong absorption in the range 700-850nm, there was another absorption in the range 500-600nm. This might be due to the existence or presence of multi-phases of indium selenide in the film. XRD analysis proved the presence of InSe phase in the unirradiated samples prepared up to an annealing temperature of 300°C.

According to the theory of optical interband absorption in solids, at the absorption edge, the absorption coefficient [α] varies with the photon energy hν and this is governed by the expression [66] $\alpha h\nu = A (h\nu - E_g)^n$, where A is a constant and E_g is the optical energy gap and n is an index with value ½ for the direct and 2 for in-direct allowed transitions. Figure 4.9 depicts the $(\alpha h\nu)^2$ versus hν graph of I IS100 and U IS100, whereas figure 6.10 shows that of U IS300 and U IS400 respectively. For U IS100 (E_g =1.61 eV and 1.85eV) and U IS300 (E_g =1.69 eV and 2.04 eV) we could observe two band gaps corresponding to the mixed phases existing in those samples. Of these, the lower value was that of InSe while higher value was that of In_2Se_3. But in the case of U IS400, there was only one absorption edge corresponding to E_g=2.48 eV. However irradiated sample exhibited single absorption edge (E_g =1.55 eV) just after annealing at 100 °C, which proved that the indium selenide formed with only one phase (InSe) in the case of irradiated system. X-ray diffraction study also showed only the presence of InSe phase (Fig. 4.8 (e)). Thus in the case of irradiated system, only an annealing at the temperature of 100 °C was required to obtain single-phase InSe film. This proved that SHI irradiation was assisting the formation of single phase InSe at lower annealing temperature. From figure 4.9 and figure 4.10, it was clear that for multi-phased film, there were two band gaps and for single phase film, there was only one band gap.

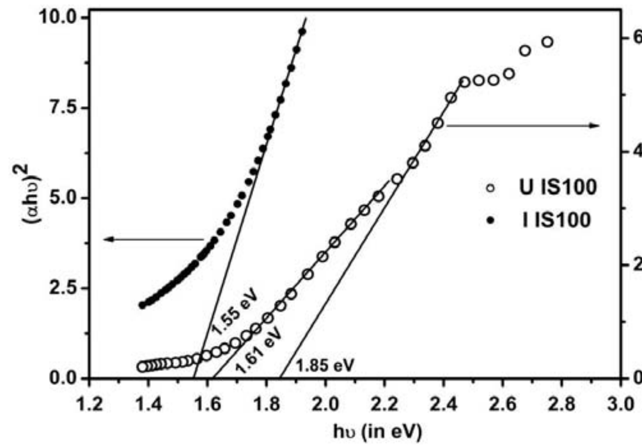

Figure 4.9: $(\alpha h\nu)^2$ versus hν graph of In/Se system (•) irradiated and (o) un-irradiated samples annealed at 100°C.

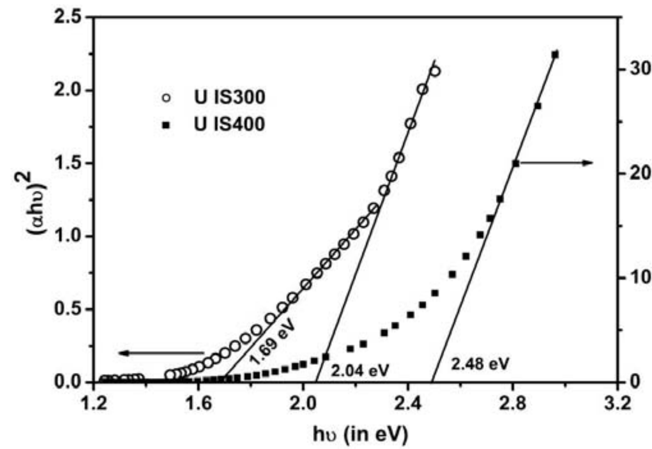

Figure 4.10: $(\alpha h\nu)^2$ versus hν graph of un-irradiated In/Se system (o) annealed at 300°C, (•) annealed at 400°C

Optical band gap of InSe film was 1.3eV [52], but in I IS100 band gap is 1.55eV. This might be due to the smaller grain size of the film. Because of the smaller grain size (~11nm) of the film, effective band gap may be larger than the

real value due to ‘quantum size effect’ [67]. The average crystallite size can be estimated using the following equation [67].

$$E_{gn} = \left[E_{gb}^{\ 2} + \frac{2\hbar^2 E_{gb} \left(\pi / R \right)^2}{m^*} \right]^{1/2} \qquad 4.6$$

Where E_{gn} and E_{gb} are the nanocrystalline and bulk semiconductor band gap, R is the particle radius and m^* (= 0.13m_o) the effective electron mass in InSe (m_o is the electronic rest mass) [68]. The average crystalline size calculated using this expression was 9.4 nm, which was in agreement with the experimental value (11nm). Another interesting observation was the phase transition of indium selenide from In_2Se_3 (hexagonal) to InSe (rhombohedral), taking place due to annealing at 100°C in the irradiated sample.

4.9 Conclusion

Single phase indium selenide can be obtained at low temperature, using ion beam mixing followed by vacuum annealing at 100°C, whereas in the un-irradiated system, single phase film was obtained only through annealing at 400°C for one hour. In/Se bilayer system irradiated using 40 MeV Si ions showed binary compound formation at lower temperature in comparison with the unirradiated sample. Again a phase transition was observed from In_2Se_3 (hexagonal) to InSe (rhombohedral) in the irradiated sample, annealed at 100°C. Swift heavy ion irradiation resulted in better atomic mixing across the interface, leading to compound formation at lower temperature and phase transition. Swift heavy ion irradiation on In/Se bilayer system followed by annealing favours InSe phase.

CHAPTER 4

Part C

Ion beam mixing in In/Se bilayer system at different electronic energy regime

Abstract

This part of the chapter elucidates the effects of inter-layer mixing between In/Se bilayer system at different electronic energy regimes. The irradiation study indicated the dependence of threshold fluence and energy of swift heavy ions required for interlayer mixing to take place between In/Se bilayer systems. Threshold fluence for mixing to take place between In/Se bilayer system was found out for 100 MeV Ag, 80 MeV Ni and 90 MeV Si ions. Optical absorption study depicted that the band gap of indium selenide can be tuned/ varied with the help of swift heavy ion irradiation followed by 100°C annealing.

4.10 Introduction

Ion beam mixing (IBM) is one of the tools used for synthesis of compound semiconductors, silicides, metal alloys at relatively low temperature [13, 69, 70, 71]. Using IBM novel phases of materials can be attained with required properties [72-76]. IBM with low energy ion beams (with few hundreds of keV energy) has been widely studied and used to form both equilibrium and meta-stable phases [77-79]. The ion beam, with this energy range loses energy of the order of keV/nucleon, to the target material through nuclear interaction with the target material (elastic collision). The atomic transport mechanism at the interface by low energy ion beams (few hundred keV energy) is explained as 'collision cascades' formed at the interface due to the atomic migration across the interface as a result of elastic collisions between projectile ions and target atoms [80, 81]. When the energy transferred to the target atoms exceed the displacement threshold of 20-50 eV, the atoms are pushed from their lattice positions and may collide with other target atoms [82]. In this manner a recoil cascade is initiated where thousands of atoms are relocated by a single ion [83]. If the recoil cascade overlaps with the interface of a layered system, this should result in atomic mixing in the vicinity of interface [84]. Fluence of the order of $1x10^{17}$ ions/cm^2 was required to obtain this type of mixing using low energy ions.

SHI's were used extensively for material modification, material synthesis, metal silicides and IBM [13, 28, 62]. The advantage of using high energy heavy ions which lose energy to the target material of the order of few MeV/nucleon is that it causes mixing with relatively low fluence ($1x10^{13}$ ions/cm^2), i.e.2-3 orders less than that of low energy ions [15, 26, 30]. In this case the energy loss is predominantly by inelastic collision with the target material, i.e. the energy loss by nuclear energy loss (by elastic collision, few eV/nm) is very negligible as compared to that of electronic energy loss, which is of the order of few tens of keV/nm. In this case, the mixing is explained using 'thermal spike model'

(discussed in section 4.2.4), in which the diffusion of atoms takes place at the interface through the molten interface. Essential condition for mixing to take place between the interfaces is that the two materials forming the interface should be in molten state, induced by SHI irradiation. But later it was proposed that if one of the materials got melted due to sudden rise of temperature induced by the dissipation of energy by SHI [85], to attain equilibrium, the molten material transfers its heat to the material in contact. If the heat transferred by the material is higher than the melting point of the material making the interface, the material in contact will also melt and mixing occurs though this molten phase.

4.11 Experiment

In/Se bilayer systems were deposited over glass substrate. Thickness of Se was 150 nm and that of In was 40 nm. These samples were irradiated using 90 MeV Si, 80 MeV Ni and 100 MeV Ag ions with fluences ranging from $1x10^{12}$ to $1x10^{14}$ ions/cm^2. Irradiation was done over an area of 1 cm^2, with the help of an electromagnetic scanner, which scanned the ion beam of 1mm diameter. Stable current of 4 nA, 9 nA and 4 nA were obtained from 15UD Pelletron accelerator (at IUAC, New Delhi) for 90 MeV Si, 80 MeV Ni and 100 MeV Ag ions respectively. RBS analysis was performed on the irradiated sample using 3 MeV He^{3+} ions. For generating 3 MeV He ions, 3 MV Pelletron accelerator at Institute of Physics, Bhubaneswar, was used. Si surface barrier detector of 20 keV resolutions, kept at a scattering angle 170°, detected the backscattered ions. Angle of incidence was kept at 10° to avoid channeling. The surface morphology of the samples was studied with a 'Veeco Digital Nanoscope IIIa SPM'. X-ray diffraction study was done to detect compound formation. Optical absorption study was done to determine the optical band gap of the samples.

4.12 Results and Discussion:

4.12.1 Rutherford backscattering analysis

(a) Irradiation using 100 MeV Ag ions

Figure 4.11(a) shows the RBS spectra of un-irradiated and irradiated In/Se bilayer system with a 100 MeV Ag ions of fluence $1x10^{12}$ ions/cm^2. We can observe a shift in the Se peak to lower channel number. But the lower channel number edge of the In peak does not show any shift. The full width at half maximum of both Se and In peak also does not show any increase. Hence one could not find any mixing between the bilayer systems. But, as the fluence increased to $6x10^{12}$ ions/cm^2 one could see the mixing between In and Se [Fig. 4.11(b)]. The lower channel number edge of the In peak (marked A), shifted towards still lower channel side. This proved the mixing between In and Se layers starting at a fluence of $6x10^{12}$ ions/cm^2. As the fluence increased to $1x10^{13}$ ions/cm^2, mixing between In and Se layers also increased further [Fig. 4.11(c)]. For 100 MeV Ag ions, the electronic energy loss is 17.75 keV/nm and 13.32 keV/nm in In and Se respectively (calculated using TRIM code 1995). From this study, we could observe that the threshold fluence for mixing to take place between In and Se layers is around $6x10^{12}$ ions/cm^2. Beyond this fluence, the mixing increased with increase in ion fluence.

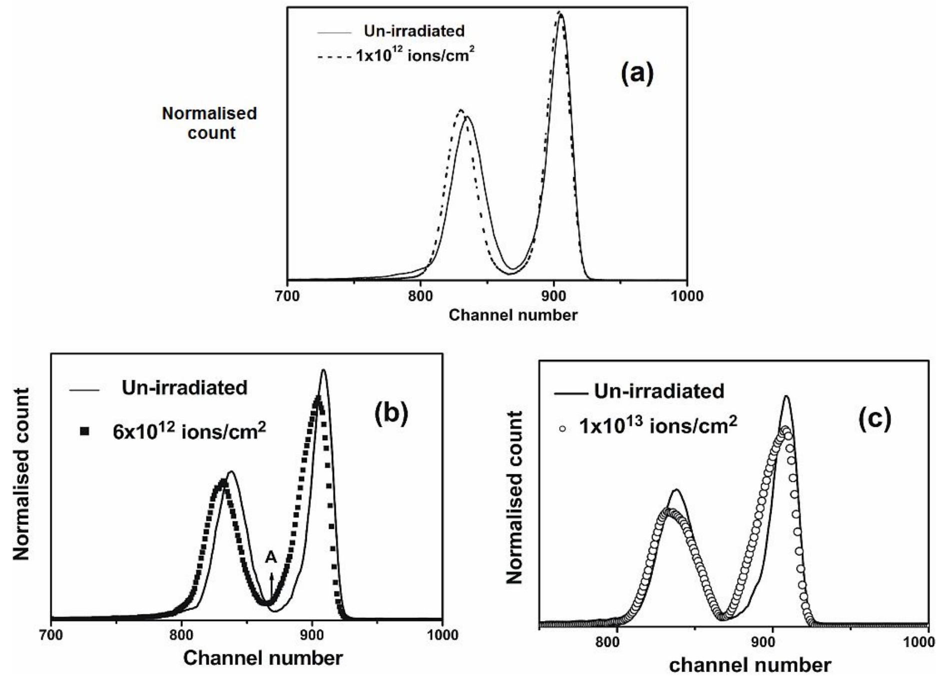

Figure 4.11: RBS spectra of un-irradiated and irradiated In/Se systems, with different fluences of 100 MeV Ag ions, (a) $1x10^{12}$ (b) $6x10^{12}$ and (c) $1x10^{13}$ ions/cm^2.

(b) Irradiation using 80 MeV Ni ions:

In the case of irradiation using 80 MeV Ni, the electronic energy loss was 12.03 keV/nm and 9.15 keV/nm on In and Se layers respectively (calculated using TRIM code 1995). Hence the mixing between the bilayer was expected to take place at higher fluence, since more ions were required for the overlapping of molten tracks. This ultimately resulted in uniform mixing at the interface [19]. Fluence ranging from $1x10^{12}$ ions/cm^2 to $1x10^{14}$ ions/cm^2 was used for irradiation using 80 MeV Ni ions. RBS study revealed that there was no mixing between the In/Se bilayer system up to a fluence of $6x10^{12}$ ions/cm^2. As the

fluence increased to $1x10^{13}$ ions/cm^2, mixing between In and Se layers was observed (Fig. 4.12). Beyond this fluence, the mixing increased with increase in ion fluence (Fig. 4.12). This proved that the threshold fluence for mixing to take place with 80 MeV Ni was around $1x10^{13}$ ions/cm^2. In comparison with the case of 100 MeV Ag ions, an additional fluence of the order of ~ $4x10^{12}$ was required to get mixing between In and Se, in the case of 80 MeV Ni ions.

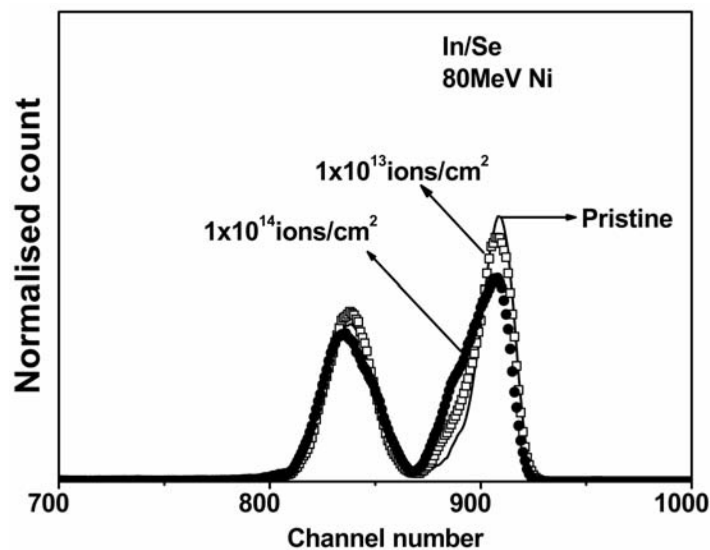

Figure 4.12: RBS spectra of un-irradiated (pristine) and irradiated In/Se systems, with fluencies $1x10^{13}$ and $1x10^{14}$ ions/cm^2 of 80 MeV Ni ions.

(c) Irradiation using 90 MeV Si

Figure 4.13 shows the RBS spectra of In/Se system irradiated using 90 MeV Si ions. In this study using 90 MeV Si ions fluences ranging from $3x10^{12}$ ions/cm^2

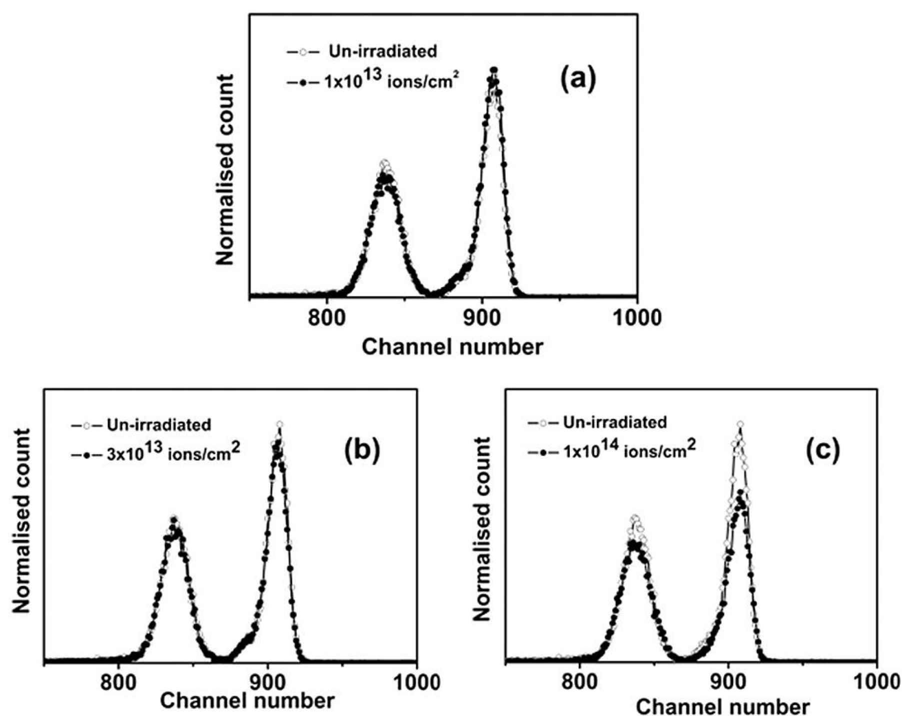

Figure 4.13: RBS spectra of In/Se systems irradiated with 90 MeV Si ions.

to $1x10^{14}$ ions/cm^2 were used for irradiation. 90 MeV Si ions lost about 4.67 keV/nm and 3.45 keV/nm as electronic energy loss in In and Se layers respectively [TRIM code 1995]. This was very much less as compared to the electronic energy loss of 100 MeV Ag and 80 MeV Ni ions. Hence we could not find any kind of mixing between In/Se bilayer up to a fluence of $3x10^{13}$ ions/cm^2. Figure 4.13 (a) and (b) depicts the RBS spectra of In/Se system irradiated with 90 MeV Si of fluence $1x10^{13}$ ions/cm^2 and $3x10^{13}$ ions/cm^2. One could not find any mixing between the bilayer systems. The full width at half maximum (FWHM) of both In and Se peaks did not show any increase, proving that there was no mixing taking place on irradiation with a fluence of $3x10^{13}$

ions/cm^2. But as the fluence increased to 1x10^{14} ions/cm^2, one could see mixing between In and Se layer [Fig. 4.13(c)]. The FWHM of the Se layer and In layer increased while the height of the both peak decreased. FWHM of Se peak increased from 18.7 to 20.9 and that of In peak increased from 13.5 to 14.9 respectively for unirradiated and In/Se system irradiated with a fluence of 1x10^{14} ions/cm^2. This showed that mixing occurred during irradiation with a fluence of 1x10^{14} ions/cm^2. One could also observe a small shift in higher channel number edge of Se peak towards right.

From RBS analysis of In/Se system irradiated using SHI of different electronic energy regimes with different ion fluences, one could get clear evidence that for different electronic energy regimes, there existed a threshold fluence for mixing to take place between the bilayer system. It can be observed from the RBS spectra [Figure 4.11(c), 4.12 and 4.13(b)] that at a fluence of 1x10^{13} ions/cm^2, the mixing between In and Se was decreasing with decrease in the electronic energy deposition. That is, we obtained more mixing in 100 MeV Ag than with 80 MeV Ni ions and very low mixing was observed for the samples irradiated with 90 MeV Si. A similar type of interface mixing with different electronic energy regime was demonstrated by Kraft et al. in which they showed the mixing of ZnO/SiO_2 using 200 MeV Xe, 260 MeV Kr and 100 MeV Ar [43]. They found that mixing was higher in the case of 200 MeV Xe than 260 MeV Kr. Again for 100 MeV Ar, there was comparatively very low mixing between ZnO/SiO_2 layers. [Electronic energy loss of 200 MeV Xe ions in ZnO/SiO2 system is 27/15.4 keV/nm; for 260 MeV Kr ions this is 18.1/10.1 keV/nm and that of 100 MeV Ar ions is 7.7/4.3 keV/nm respectively]. This revealed the dependence of electronic energy loss on the phenomena of ion beam mixing. One more thing to be noted is the dependence of fluence and the electronic energy deposited by the ions. In the case of In/Se bilayer system, one could see that only a fluence of ~ 6x10^{12} ion/cm^2 was required to probe mixing between In and Se. whereas a fluence of ~ 1x10^{13} ions/cm^2 was required in the case of 80

MeV Ni ions. But fluence of almost ~ $1x10^{14}$ ions/cm^2 was required with that of 90 MeV Si ions.

Mixing between the bilayer under dense electronic energy regime (or using SHI irradiation) is explained with the 'thermal spike model' [41, 42] (as explained in section 4.2.4). According to this model, as the ions pass through the material, if the energy of the ions are sufficiently high, it increases the lattice temperature. If the temperature rise is above the melting point of the material, material melts and a transient molten track forms. Mixing between the layers occurs across the interface by inter-diffusion of the atoms through the molten track. In our case, we observed mixing between In and Se with 90 MeV Si ions which deposited about 4.67 keV/nm and 3.45 keV/nm energy to In and Se respectively. This proved that the threshold energy for creating molten transient tracks in In and Se was about 4.67 keV/nm and 3.45 keV/nm respectively. But higher fluence of about $1x10^{14}$ ions/cm^2 was required, which was more than one order higher than that of 100 MeV Ag ions, for mixing to take place between In and Se.

Swift heavy ions pass through the material, creating molten cylindrical tracks of few nano-meters along the path, if the energy is sufficiently high. Till now, lots of studies has been carried out, experimentally and theoretically, and found that ion track radius (cylindrical molten track radius) was dependent on electronic energy deposition [85, 86, 87]. Track radius increased with electronic energy deposition [88]. Toulemonde et al. [88] found, in the case of a-Ge, a-Si and in $Fe_{85}B_{15}$ that radius of molten track increased with increase in electronic energy deposition. As the fluence increased, the ion tracks with few nanometer size overlapped and a uniform mixing occurred. In the case of ions which deposit less energy, the molten track radius will be small. Hence higher fluence was required for mixing to take place. But for ions with higher energy deposition, the track radius will be high and one can obtain mixing with lower fluence. This might be the reason why we have obtained mixing between In and Se with lower fluence for 100 MeV Ag ions as compared with 80 MeV Ni and 90 MeV Si ions.

Similar result with low fluence was reported by Kraft et al. in which they observed mixing between ZnO/SiO_2 at a fluence of $4.2x10^{15}$ ions/cm^2 when they used 200 MeV Xe ions [43], whereas a fluence of $5.7x10^{15}$ ions/cm^2 was required with 260 MeV Kr ions.

4.12.2 Atomic Force Microscopy (AFM) analysis

SHI induced modification in surface morphology of In/Se system was studied using AFM. By using AFM one could get the information of the deformation/changes of the surface occurred during SHI irradiation [89, 90]. SHI induced ditch and dick formation [91] and plastic flow of the materials [90] were observed and was attributed due to the macroscopic momentum transfer from ion beam to the target material [92]. The mechanism of surface modification due to these processes, however, is far from clear .

Figure 4.14 shows the AFM picture (5x5 μm dimension) of unirradiated and irradiated In/Se system with 100 MeV Ag ions of fluences $1x10^{12}$ and $1x10^{13}$ ions/cm^2. One could clearly observe the variation in surface morphology induced by 100 MeV Ag ions. The unirradiated In/Se system [Fig. 4.14(a)] gives the uniform surface morphology with an RMS roughness of ~15 nm and as the fluence increased to $6x10^{12}$ ions/cm^2 we can see clearly isolation/clustering of surface material [Fig. 4.14(b)]. More over, craters were observed between the clusters. When the fluence was increased to $1x10^{13}$ ions/cm^2 clustering of the surface material could be clearly observed [Fig. 4.14(c)]. Piling up of material along the sides of craters could also be observed. Craters with a radius of 0.5 μm to 0.65 μm could be seen with a fluence of $1x10^{13}$ ions/cm^2. The craters formation might be due to the explosive evaporation of material during SHI irradiation and / or due to the plastic flow of material due to tremendous electronic energy deposited during irradiation [93]. This type of crater formation was observed in different materials at high fluences. The high energy deposited

by the SHI might be breaking the bonds between the atoms, resulting in the enhancement of the mobility of atoms to form clusters of material. Clusters of different sizes, ranging from 0.5 µm to 1 µm, could be observed in the case of sample irradiated with $1x10^{13}$ ions/cm^2.

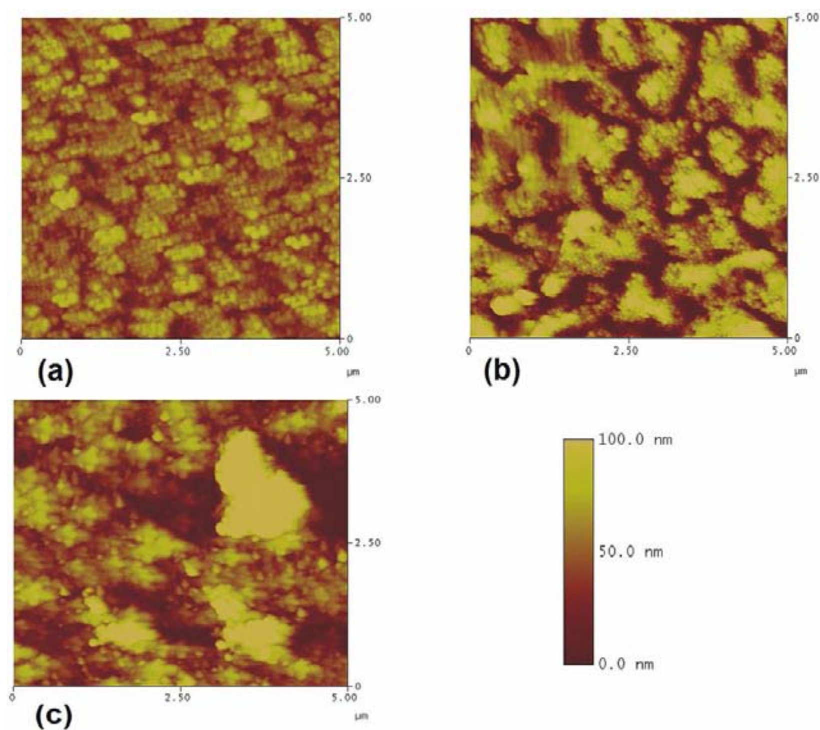

Figure 4.14: Atomic Force micrograph (AFM) of (a) un-irradiated In/Se system (b) irradiated with $6x10^{12}$ ions/cm^2 and (c) $1x10^{13}$ ions/cm^2 of 100 MeV Ag ions.

Figure 4.15 shows the AFM pictures of In/Se system irradiated using 80 MeV Ni. In this case, we can see that there is not much variation in surface morphology of the sample irradiated with a fluence of $1x10^{13}$ ions/cm^2 [Fig. 4.15(a)]. As the fluence increased to $3x10^{13}$ ions/cm^2 clustering of the surface

material along the sides of the craters can be observed [Fig. 4.15(b)]. One can also observe the clusters of different sizes here.

From the AFM study of In/Se system irradiated with different energy ions, one could find that the surface modification induced by swift heavy ions was depending on electronic energy deposition. For 100 MeV Ag ions, which deposits an energy of 17.75 keV/nm in Indium (the surface layer), lower fluence of about $6x10^{12}$ ions/cm^2 was required, while with 80 MeV Ni, which deposits an energy of 12.03 keV/nm, a higher fluence of ~$3x10^{13}$ ions/cm^2 is required to produce surface modification.

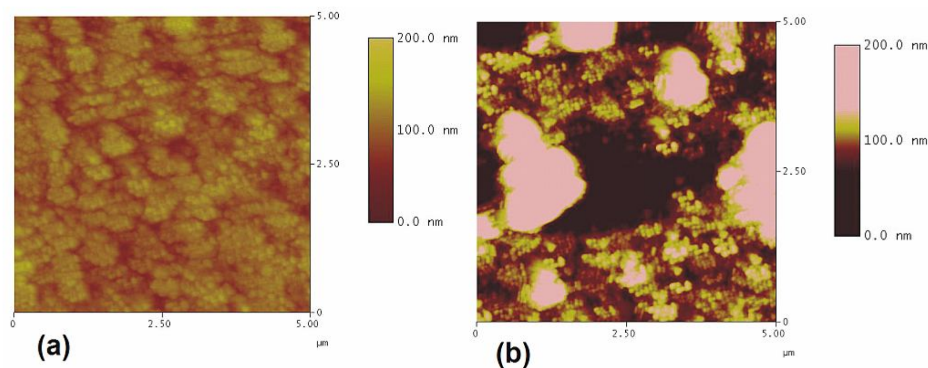

Figure 4.15: AFM pictures of In/Se system irradiated with 80 MeV Ni ions of fluence (a) $1x10^{13}$ ions/cm^2 and (b) $3x10^{13}$ ions/cm^2

4.12.3 X-ray diffraction analysis

(a) Irradiation using 100 MeV Ag ions

Figure 4.16 shows the XRD pattern of In/Se system irradiated with different fluences ranging from $1x10^{12}$ to $1x10^{13}$ ions/cm^2. The unirradiated one (Fig.

4.16(a)), showed only the x-ray diffraction peak from elemental In and Se at $2\theta = 32.75^o$ and $2\theta = 23.36^o$ respectively. The prominent peak of In at $2\theta = 32.75^o$ (unirradiated sample) with a FWHM of 0.2684 reduced to about 0.2427 on irradiation with a fluence of $1x10^{12}$ ions/cm^2. The decrease in FWHM of In peak reflects the enhancement in the crystallinity of In layer due to 100 MeV Ag ion irradiation. The other thing to be noted is that the Se peak vanished on irradiation. This may be due to the amorphisation of the Se layer. On increasing the fluence to $6x10^{12}$ ions/cm^2 we could observe the formation of indium selenide compound, [In_2Se_3 phase] at $2\theta = 36.37$, 27.84 and In_6Se_7 phase at $2\theta = 20.69^o$ respectively (Fig. 4.16 (c)). From RBS analysis, it became evident that at this same fluence ($6x10^{12}$ ions/cm^2) mixing between In/Se layers took place. XRD analysis also confirmed the compound formation at this fluence without any post annealing treatment. This proved beyond doubt that the threshold fluence for indium selenide compound formation with 100 MeV Ag ions is $6x10^{12}$ ions/cm^2. Here also we could find the presence of elemental indium in the sample. This might be due to the agglomerated / clustered indium present in the surface of the film. In this case also the FWHM of In peak decreased to a value of 0.2271. But further increase of fluence [i.e. to $1x10^{13}$ ions/cm^2] resulted in the amorphisation of indium selenide formed (peaks of indium selenide at $2\theta = 36.37$, 27.84 and 20.69^o vanished on increasing the fluence) [Fig. 4.16(d)]. But the FWHM of the In peak decreased to 0.2194. This confirmed that, in metal layer and in semiconductors, swift heavy ions behave differently. In metal (In), it is improving/ enhancing the crystallinity whereas in semiconductor (indium selenide), it is amorphising the material.

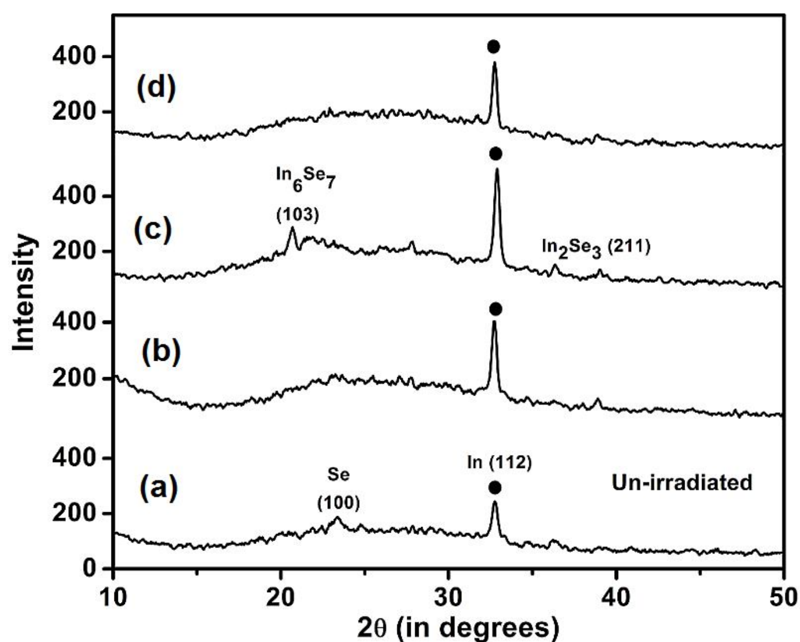

Figure 4.16: XRD pattern of In/Se system (a) un-irradiated and irradiated with 100 MeV Ag ions of fluences (b) $1x10^{12}$ (c) $6x10^{12}$ and $1x10^{13}$ ions/cm^2.

The samples were vacuum annealed at 50°C and 100°C for 1 h at the pressure of $2x10^{-5}$ mbar. Figure 4.17 shows the In/Se system annealed at 50°C for 1h. In the unirradiated sample, there was unreacted Se [XRD peak at $2\theta = 23.6$] along with In_2Se_3 formed along (202) plane [XRD peak at $2\theta = 28.95^o$] (Fig 4. 17(a)). One could also find a new XRD peak [though faint] at $2\theta = 23.88$ for the samples irradiated with $6x10^{12}$ and $1x10^{13}$ ions/cm^2, which was identified to be due to In_6Se_7 phase. The reflection from In_6Se_7 phase (Fig. 4.16(c)) at $2\theta = 20.69$ disappeared on annealing at 50 ^{o}C (Fig. 4.17(c)) in the case of sample irradiated with a fluence of $6x10^{12}$ ions/cm^2. One interesting point to be noted here is that the intensity of In peak of irradiated sample is much higher than that of un-irradiated sample. In the case of unirradiated sample, the intensity of In

decreased due to the diffusion taking place between In and Se, thereby reducing the presence of elemental In. But in the case of irradiated sample the clustered In atoms present in the surface of the sample are not participating in the diffusion process. This might be the reason for the increase in the peak intensity.

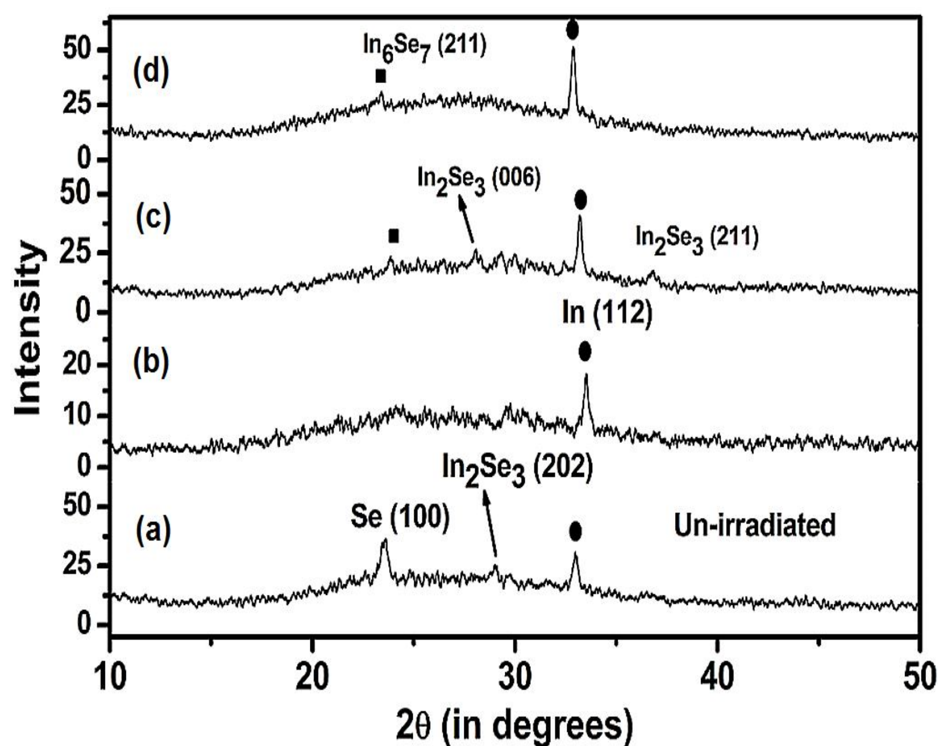

Figure 4.17: XRD pattern of In/Se system (a) un-irradiated, irradiated with 100 MeV Ag ions of fluences (b) $1x10^{12}$ (c) $6x10^{12}$ and $1x10^{13}$ ions/cm^2 and annealed at 50°C for 1h.

Figure 4.18 shows the XRD pattern of the samples annealed at 100°C for 1 h. On annealing the sample at 100 ^{o}C, we observed In_2Se_3 phase formation in all the samples. Again, the samples irradiated with $6x10^{12}$ and $1x10^{13}$ ions/cm^2 had

In_6Se_7 phase also (Fig. 4.18(c) and (d)). The sample irradiated with 6x10^{12} ions/cm^2 showed the formation of InSe phase [peak at 2θ = 32.54^o]. In this case the In peak completely vanished. This might be due to the complete mixing of In layer with Se to form indium selenide. In the case of sample irradiated with 1x10^{13} ions/cm^2, the intensity of the InSe peak increased. This shows the increase in mixing between In and Se layers.

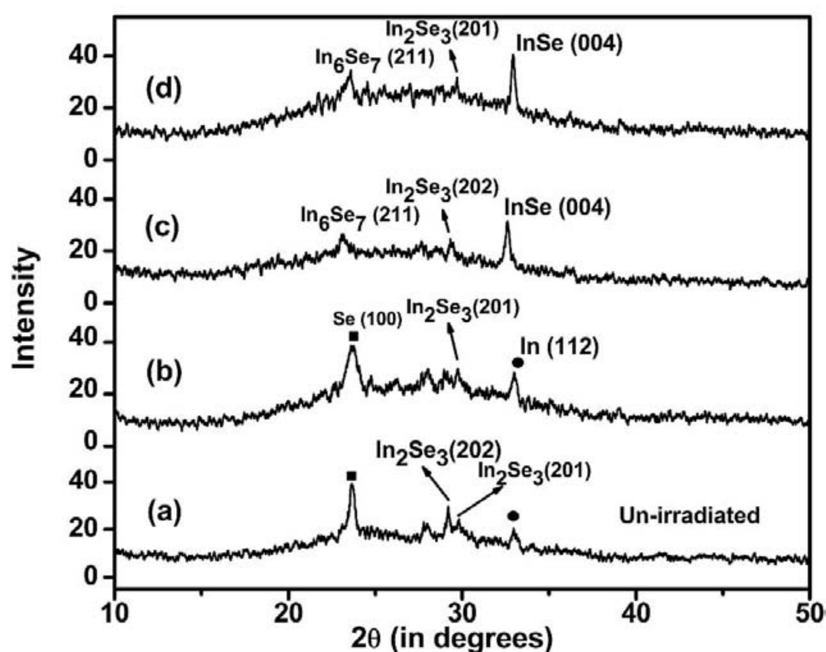

Figure 4.18: XRD pattern of In/Se system (a) un-irradiated, irradiated with 100 MeV Ag ions of fluences (b) 1x10^{12} (c) 6x10^{12} and 1x10^{13} ions/cm^2 and annealed at 100°C for 1h.

By RBS study, we found that the mixing between In and Se layers occurred at a fluence of 6x10^{12} ions/cm2 with 100 MeV Ag ions. During the passage of SHI,

it created defects and atomic displacements at the interface. These defects were immobile at room temperature and when we supplied enough energy by annealing at 100 ^{o}C, more atoms diffused across the interface through the defects and we obtained a complete mixing [62, 69].

(b) Irradiation using 80 MeV Ni ions.

In/Se bilayer system was irradiated using 80 MeV Ni ions of different fluences ranging from $1x10^{12}$ to $1x10^{14}$ ions/cm^2. XRD analysis showed no compound formation up to fluence of $3x10^{13}$ ions/cm^2 (Fig. 4.19(d)). But as the fluence increased to $1x10^{14}$ ions/cm^2 indium selenide (In_2Se_3) compound formation was observed [XRD peak at 2θ = 39.45] along (212) plane (Fig. 4.19(e)).The elemental In was also present in the sample.

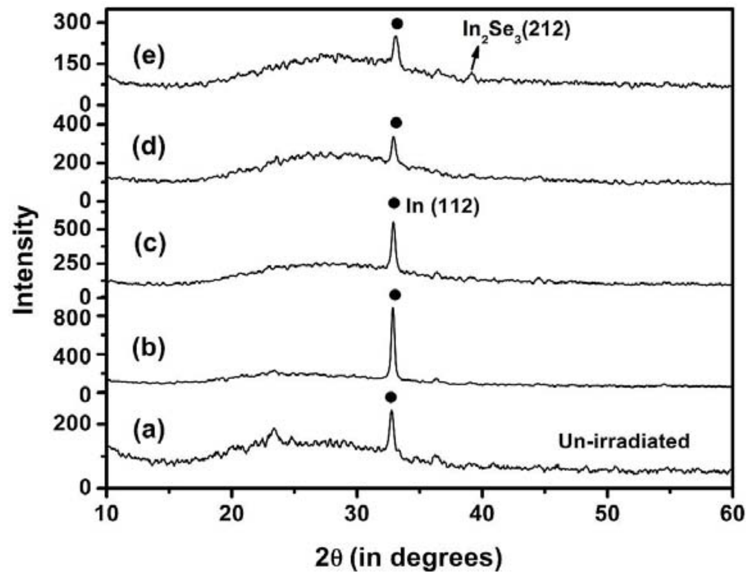

Figure 4.19: XRD pattern of In/Se systems (a) un-irradiated, and irradiated with 80 MeV Ni ions of fluences (b) $1x10^{12}$, (c) $1x10^{13}$, (d) $3x10^{13}$ and (e) $1x10^{14}$ ions/cm^2.

Figure 4.20 shows the XRD pattern of the In/Se system annealed at 50 °C for 1 h. Here in the sample irradiated with a fluence of $1x10^{12}$ ions/cm^2 itself, one could see the compound formation (In_2Se_3) resulting in the peak at 2θ = 27.82 along (006) plane. But the sample irradiated with a fluence of $3x10^{12}$ ions/cm^2 showed In_2Se_3 formation [peak at 2θ = 29.47 corresponding to (201) plane]. Samples irradiated with higher fluence did not show any sign of crystalline compound formation. In the case of samples irradiated with higher fluence, higher order of defects and/ or amorphisation might have taken place and might require more energy for crystalline indium selenide formation.

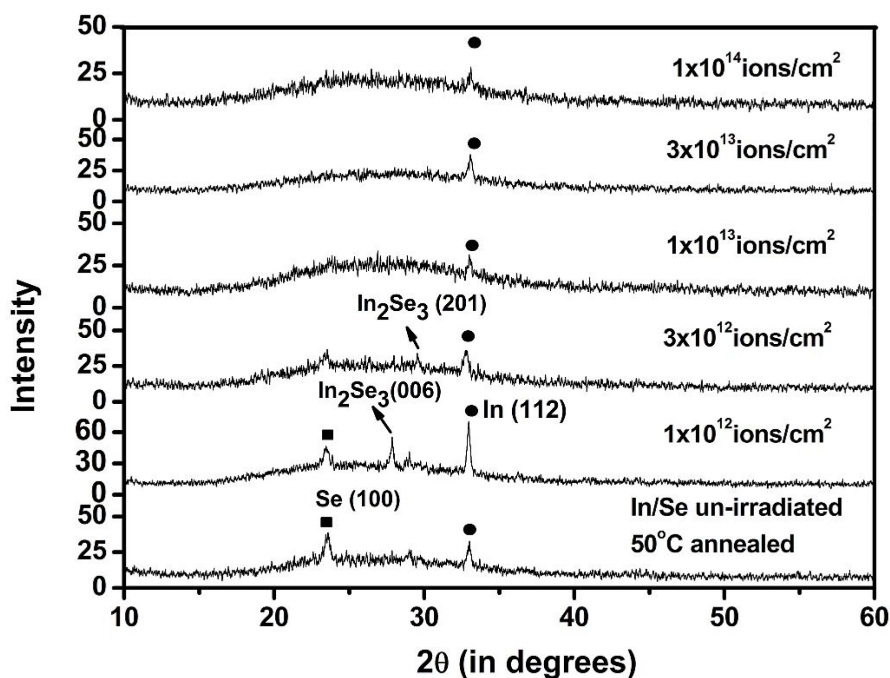

Figure 4.20: XRD pattern of In/Se systems irradiated with 80 MeV Ni ions and annealed at 50°C for 1 h.

On annealing the sample at 100 °C, we observed compound formation in all the samples (Fig. 4.21). As we supplied sufficient energy, the atoms migrated across the interface, which resulted in the formation of crystalline In_2Se_3 and InSe phases. It was also seen that the peak of elemental In completely vanished for the sample irradiated with a fluence of $3x10^{12}$ ions/cm^2 (Fig. 4.21(c)). However the sample irradiated with $3x10^{13}$ ions/cm^2 showed only the reflection from InSe phase (Fig. 4.21(e)), whereas all other samples showed multi-phased indium selenide formation.

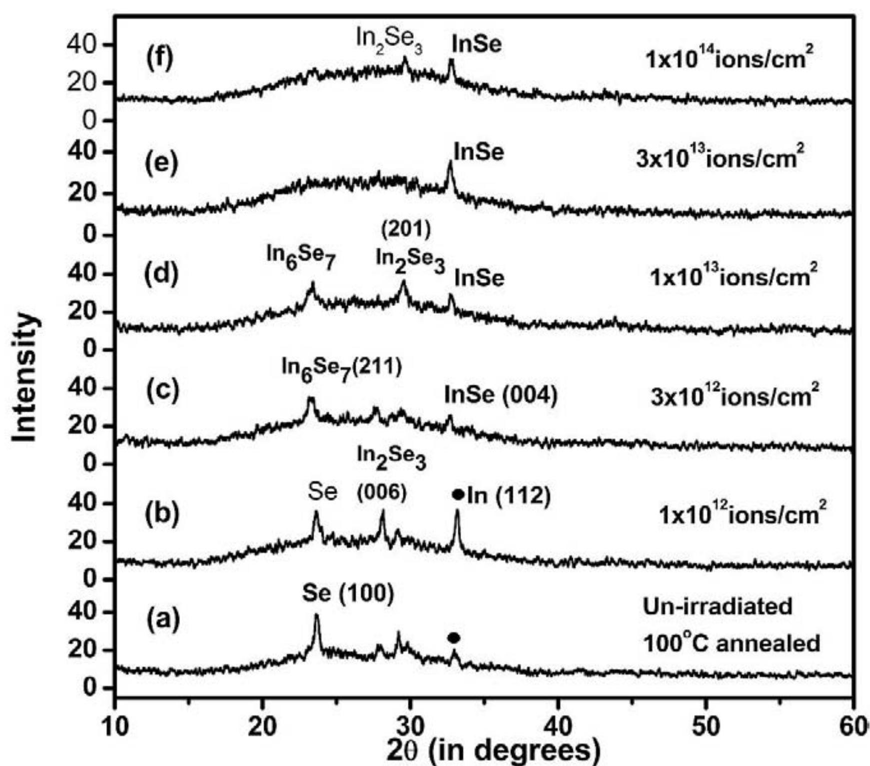

Figure 4.21 XRD pattern of In/Se systems irradiated with 80 MeV Ni ions and annealed at 100°C for 1 h.

(c) Irradiation using 90 MeV Si ions.

Different fluences ranging from $3x10^{12}$ to $1x10^{14}$ ions/cm^2 were used for irradiating the sample using 90 MeV Si ions. Figure 4.22 shows the XRD pattern of these samples. No compound formation was observed up to a fluence of $3x10^{13}$ ions/cm^2 [Fig. 4.22(b)]. But In_2Se_3 phase was formed [peak at 2θ = 27.71^o and 28.87^o corresponding to (006) and (201) planes respectively] with a fluence of $1x10^{14}$ ions/cm^2 [Fig. 4.22(c)]. However elemental In and Se were also present in the sample. Thus the threshold fluence for compound formation to take place between In and Se with 90 MeV Si ions was found to be $1x10^{14}$ ions/cm^2.

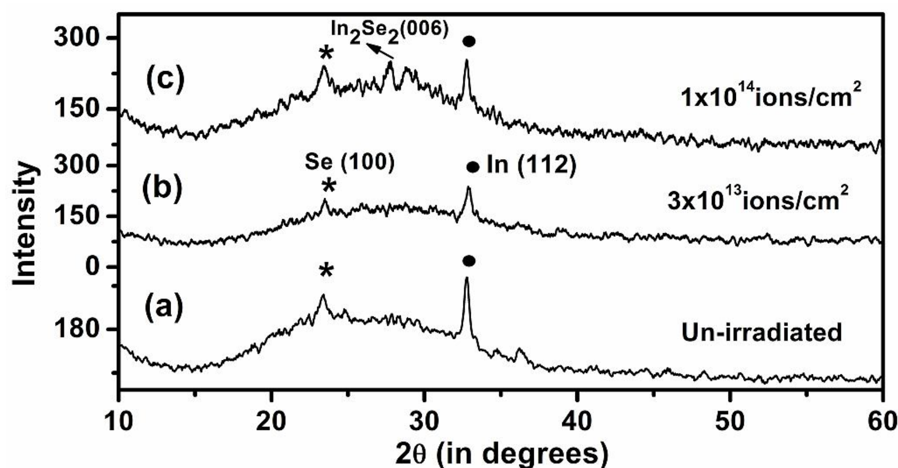

Figure 4.22: XRD pattern of In/Se system irradiated with 90 MeV Si ions.

Figure 4.23 shows the In/Se samples annealed at 50°C for 1h. No crystalline indium selenide formation was observed up to a fluence of $3x10^{13}$ ions/cm^2. But the sample irradiated with $1x10^{14}$ ions/cm^2 showed crystalline indium selenide phases as we observed in the irradiated case [Fig. 4.23(b)]. The FWHM of the peaks along (006) and (201) plane decreased on annealing at 50°C. This shows

that the crystallinity increased on annealing at 50 °C. But in this case also, elemental In was present in the sample, which might be the clustered In atoms present on the surface of the film.

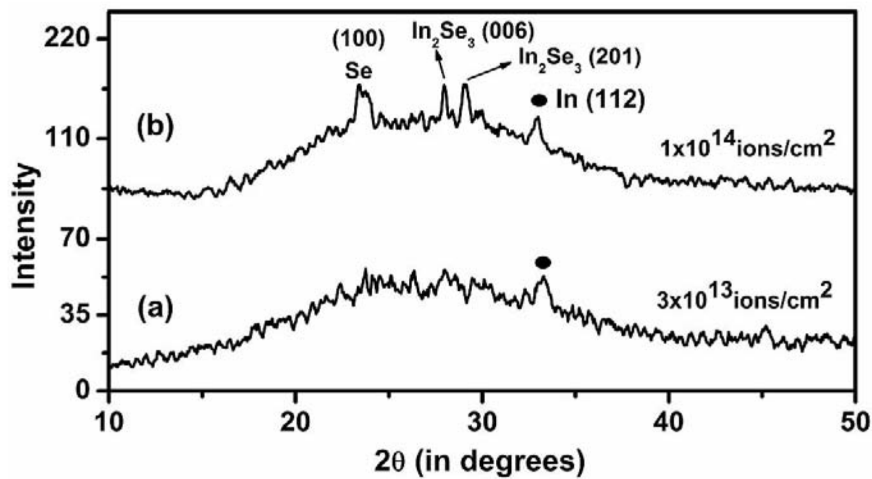

Figure 4.23: XRD pattern of In/Se system irradiated with 90 MeV Si ions and annealed at 50°C for 1 h.

On annealing the samples at 100 °C, one could see that the elemental In present in the sample was almost lost fully (Fig. 4. 24). This might be due to the mixing taking place between In and Se, when sufficient energy was supplied. But we could see the formation of mixed phases of indium selenide (In_2Se_3 and In_6Se_7) on annealing at 100 °C [Fig. 4.24(d), (e) and (f)]. One thing again to be noted is the decrease in crystallinity. The FWHM of the peaks increased on annealing.

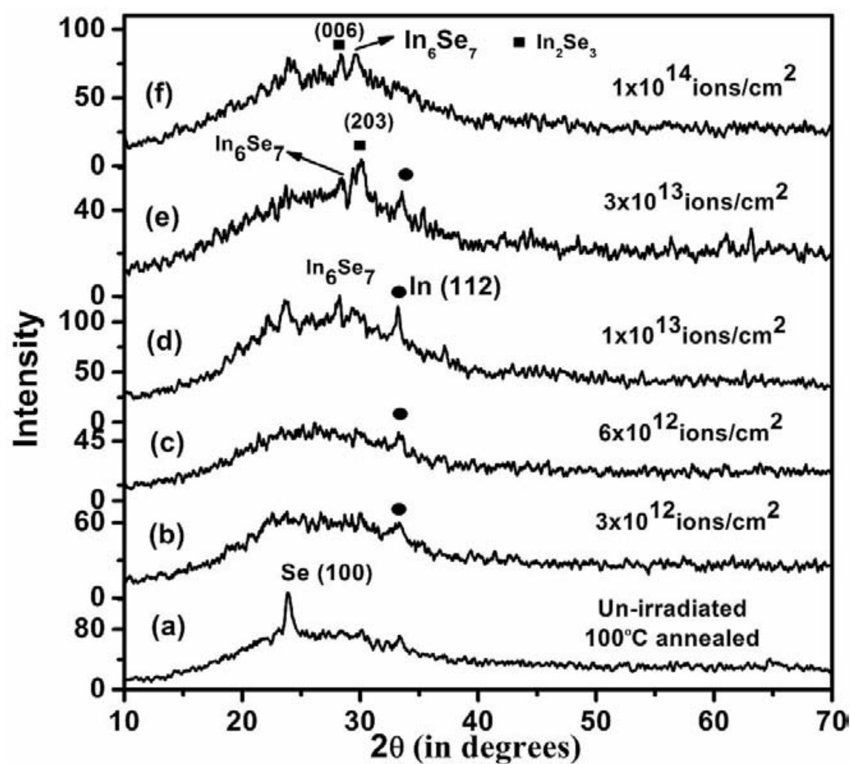

Figure 4.24: XRD pattern of In/Se system irradiated with 90 MeV Si ions and annealed at 100°C for 1 h.

4.12.4 Optical absorption studies

(a) 100 MeV Ag ion irradiation:

Optical absorption studies of samples irradiated with 100 MeV Ag ions were carried out in the range of 400 – 900 nm. Figure 4.25 shows the absorption spectra of these samples. One can clearly observe here a blue shift in the absorption edge on increasing the irradiation fluence. Optical band gap of the

material was found out from $(\alpha h\upsilon)^2$ versus $h\upsilon$ plot, by extrapolating the straight portion of the plot to $\alpha=0$ Table 4.1]. There is an increase in optical band gap of the sample from 1.83 eV to 2.01 eV on irradiation with a fluence of $6x10^{12}$ ions/cm^2 and this reveals the formation of indium selenide. In fact the XRD pattern (Fig. 4.16) proved In_2Se_3 formation along with In_6Se_7 phase. On increasing the fluence further to $1x10^{13}$ ions/cm^2, the band gap increased to 2.25 eV. Figure 4.26 shows the $(\alpha h\upsilon)^2$ versus $h\upsilon$ plot of the unirradiated and the sample irradiated with a fluence of $1x10^{13}$ ions/cm^2. From this it is clear that increase in optical band gap suggesting the formation of indium selenide phase.

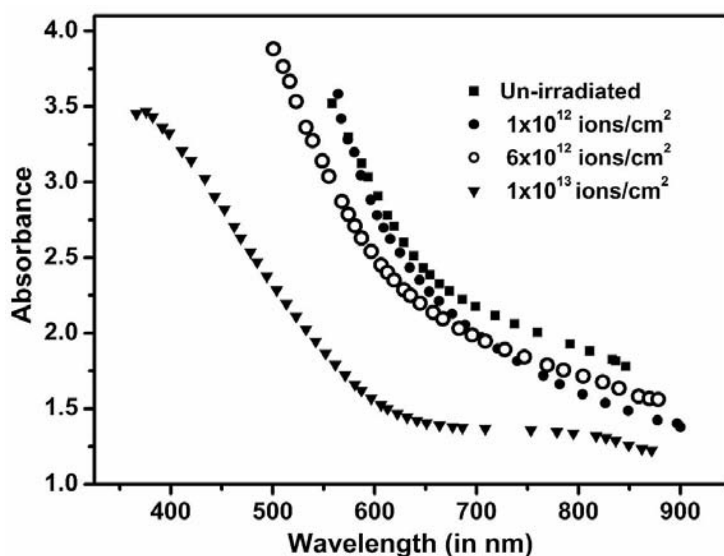

Figure 4.25 Absorption spectra of In/Se systems irradiated with different fluences of 100 MeV Ag ions.

Table 4.1: Optical band gap of the samples irradiated using 100 MeV Ag ions

Sl. No.	Irradiation fluence (ions/cm^2)	Band gap (eV)		
		As irradiated	Annealed at 50°C	Annealed 100°C
1.	Un-irradiated	1.83	1.82	1.83
2.	$1x10^{12}$	1.88	1.9	1.9
3.	$6x10^{12}$	2.01	2.07	2.05
4.	$1x10^{13}$	2.25	2.45	2.5

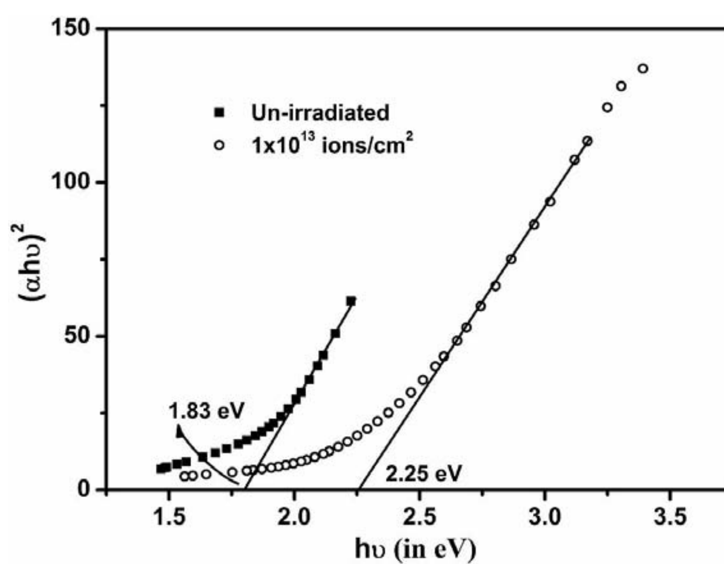

Figure 4.26 $(\alpha h\upsilon)^2$ versus hυ plot of In/Se system, un-irradiated and irradiated with 100 MeV Ag ions of fluence $1x10^{13}$ ions/cm^2

On annealing the samples at 50°C (at a pressure of $2x10^{-5}$ mbar.) for 1 h, the band gap of the samples increased further (Table 4.1). But in the case of

unirradiated sample, there was no such increase. The sample irradiated with a fluence of $1x10^{13}$ ions/cm^2 had the maximum band gap of 2.45 eV. The increase of band gap can be due to the quantum size effect [67]. This effect often appears in amorphous materials or in material with particle size of few nanometers. But in our case, we can see the XRD pattern of In_6Se_7 phase and crystalline In layer [Fig. 4.17(d)]. The average grain size of the sample irradiated with $1x10^{13}$ ions/cm^2 is about ~29 nm(2θ=23.41, FWHM=0.2766), and thus we can rule out the increase in band gap due to quantum size effect.

When these samples were further annealed at 100°C for 1 h, the band gap further increased [Table 4.1]. A band gap of about 2.5 eV was observed for the sample irradiated with a fluence of $1x10^{13}$ ions/cm^2. Average grain size of the samples irradiated with $6x10^{12}$ and $1x10^{13}$ ions/cm^2 were 39 and 44 nm respectively (2θ = 32.54, FWHM = 0.2110 and 0.1868) and hence the possibility of increase in band gap due to quantum size can be ignored. The increase in band gap in this case can be explained by considering the annihilation of defects bands or the Urbach tale due to the irradiation followed by annealing at 100 ^{o}C.

In the case of intrinsic semiconductors, there would be no defect levels in the forbidden gap, making the absorption possible only when a photon of energy greater or equal to the band gap is incident on it, leading to band-to-band transition. But in the case of impurity semiconductors, there could be defect levels in forbidden gap, resulting in the absorption of photons with sub band gap energies too. There can also be dense localized energy states, near the valence and conduction band edges, known as ‘Urbach energy bands’, whose density decays exponentially as one moves away from valence and conduction band edges [94]. Different semiconductors, namely a-SiC [95], a-C: H [96] and even chalcogenide compounds such as $CuInSe_2$ [97] and InSe [98] exhibited Urbach tail. Urbach energy width (tail width) is a measure of disorder in the material [96].

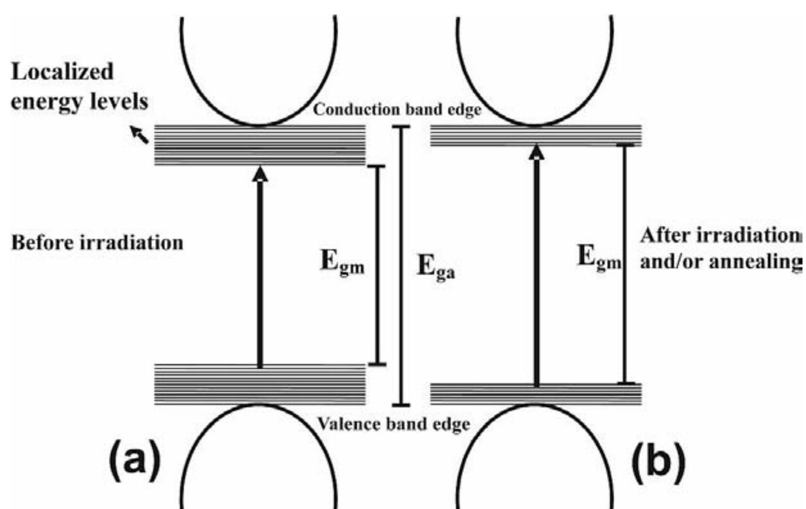

Figure 4.27: Sketch of the assumed band structure, with dense localized energy states near band edges (a) before irradiation and (b) after irradiation and/or annealing.

Figure 4.27 shows the sketch of the assumed band structure, with dense localized energy states near band edges. Because of the presence of these states, it was very difficult to distinguish between the bottom of the conduction band and the top of the valence band with the band tails and this results in absorption even at energies much below the band gap. According to Urbach rule [99, 100], below the fundamental absorption edge, the absorption coefficient α varies exponentially as $\alpha = \alpha_o \exp(h\upsilon/E_u)$, where '$\alpha_o$' is the characteristic parameter of the material, '$h\upsilon$' the photon energy and 'E_u', the width of the exponential tail, known as the Urbach energy or Urbach tail energy. This region is attributed to the electronic transition between a localized band tail and an extended band [101] and represents the degree of disorder in the material. The Urbach tail width (E_u) can be estimated from the inverse slope of the plot '($\ln \alpha$) versus $h\upsilon$' below the fundamental absorption [100]. E_u of all the samples after annealing at 50°C and 100°C were calculated and tabulated in Table 4.2. On annealing (at a pressure of $2x10^{-5}$ mbar.) the samples at 50°C for 1 h, the Urbach energy decreased from 1.67 eV (un-irradiated sample) to 901 meV for the sample

irradiated with a fluence $6x10^{12}$ ions/cm^2. One could observe that the Urbach tail width decreased further on annealing at 100°C. The decrease of Urbach tail width indicated that irradiation could anneal out the disorders (localized states) in the material, which resulted in the increase of band gap of the material. Similar type of annealing out of disorders and subsequent increase of band gap was observed in In_2Se_3 by El-Shair et al. by thermal annealing at higher temperatures [99].

Table 4.2: Urbach energy variation of samples irradiated with 100 MeV Ag ions annealed at different temperatures.

Sl. No.	Irradiation fluence (ions/cm^2)	Urbach energy (eV)	
		Annealed at 50 ^{o}C	Annealed at 100 ^{o}C
1.	Un-irradiated	1.67	1.04
2.	$1x10^{12}$	0.968	0.784
3.	$6x10^{12}$	0.901	0.877
4.	$1x10^{13}$	0.917	0.882

When we measure the optical band gap of the material, because of the band tailing, we were able to measure only the band gap Eg_m. This was very much less than the actual band gap Eg_a of the material [Fig. 4.27]. Urbach tail width measurements on the irradiated sample revealed annealing out the localized energy bands near the band edges, indicating a reduction in E_u. As a result of this, conduction and valence band tail states were separated further apart in energy [Fig. 4.27(b)], which was evident from blue shift in absorption spectra [Fig. 4.25]. This might be the reason for the increase in band gap of indium selenide samples.

(b) 80 MeV Ni ion irradiation

Optical band gap of the samples irradiated using 80 MeV Ni ions was calculated from $(\alpha h\upsilon)^2$ versus $h\upsilon$ plot [Table 4.3]. An increase in the band gap could be observed as the irradiation fluence increased, reaching a maximum of 2.34 eV, for the sample irradiated with a fluence of $1x10^{14}$ ions/cm^2. XRD analysis indicated (Fig. 4.20) indium selenide formation, at this fluence. This shows that the band gap of Indium selenide can be increased to 2.34 eV without any post annealing treatment. On annealing the samples at 50°C and 100°C for 1 h (at a pressure of $2x10^{-5}$ mbar.), the band gap further increased, reaching a value of about 2.88 eV for the sample irradiated with a fluence of $1x10^{14}$ ions/cm^2. The optical band gap of the samples was tabulated in table 4.3. In this case also the increase in band gap of the samples can be explained as due to the reduction in the Urbach energy. Urbach energy of the samples were calculated and tabulated in table 4.4. From the table we can see that the Urbach energy of the samples irradiated with 80 MeV Ni ions after annealing at (50°C and 100°C) were less than that of the unirradiated samples. This shows that, irradiation can anneal out the defect bands present at the valence and conduction edges. We can observe an increase in Urbach energy in the case of sample irradiated with a fluence of $3x10^{13}$ ions/cm^2 after annealing at 100°C. This was also reflected in the band gap of the sample. The increase in Urbach energy might be due to the increase in planar defects in the sample [102, 103], since the sample formed is single phase InSe, which has hexagonal planar structure. Reduction in Urbach energy in InSe due to decrease of planar defects in InSe was reported earlier by us due to 40 MeV Si ions in indium selenide films [103].

Table 4.3: Optical band gap of samples irradiated with 80 MeV Ni ions

Sl. No.	Irradiation fluence (ions/cm^2)	Band gap (eV)		
		As irradiated	Annealed at 50°C	Annealed at 100 ^{o}C
1.	1x10^{12}	1.7	1.76	1.63
2.	1x10^{13}	1.96	1.96	2.45
3.	3x10^{13}	2.2	2.52	2.2
4.	1x10^{14}	2.34	2.52	2.88

Table 4.4 Showing Urbach energy of the sample irradiated with 80 MeV Ni.

Sl. No.	Irradiation fluence (ions/cm^2)	Urbach energy (eV)	
		Annealed at 50 ^{o}C	Annealed at 100 ^{o}C
1.	Un-irradiated	1.67	1.04
2.	1x10^{12}	1.04	0.738
3.	1x10^{13}	0.829	0.811
4.	3x10^{13}	0.896	0.943
5.	1x10^{14}	0.952	1.01

(c) Irradiation using 90 MeV Si ions

As in the case of irradiation using 100 MeV Ag ions and 80 MeV Ni ions, the optical band gap of the material increased on irradiation with 90 MeV Si ion, followed by annealing at 50 and 100°C. Fluence used for irradiation ranges from 3x10^{12} to 1x10^{14} ions/cm^2. As the irradiation fluence increased, the optical band gap also increased. A maximum value of about 2.04 eV was achieved for the samples irradiated with a fluence of 1x10^{14} ions/cm^2 after annealing at 50°C.

When this sample was again annealed at 100°C for 1 h, the band gap reached to a value of 2.8 eV. The values of band gap are tabulated in table 4.5. Here a clear increase in optical band gap can be observed as the irradiation fluence increases. Figure 4.28 gives the $(\alpha h\upsilon)^2$ versus hυ plot of the samples which are irradiated with 90 MeV Si ions, with different fluences and annealed at 50°C. Figure 4.29 shows the absorption spectra of the samples irradiated with a fluence of $1x10^{13}$, $3x10^{13}$ and $1x10^{14}$ ions/cm^2 and annealed at 100°C. We can see a sharp shoulder at about 600 nm, corresponding to a strong defect level in the sample irradiated with $3x10^{13}$ ions/cm^2. As the fluence increased to $1x10^{14}$ ions/cm^2, the shoulder became broader. Also the absorption shifted towards lower wavelength indicating an increase in band gap of the material.

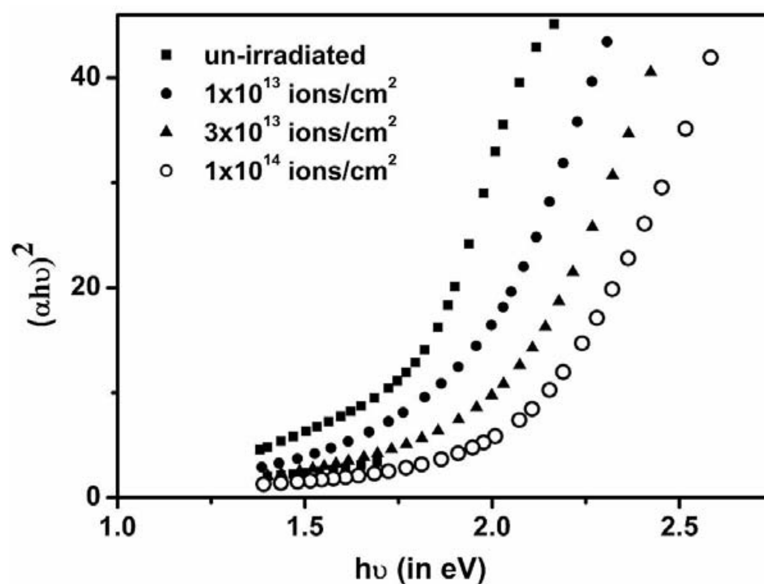

Figure 4.28 $(\alpha h\upsilon)^2$ versus hυ plot of In/Se system irradiated with different fluences of 90 MeV Si ions and annealed at 50°C for 1 h.

Table 4.5 Band gap of the samples irradiated with 90 MeV Si ions and annealed at 50 and 100 °C.

Sl. No.	Irradiation fluence (ions/cm^2)	Band gap (eV) Annealed at 50 °C	Annealed at 100 °C
1.	Un-irradiated	1.73	1.81
2.	$3x10^{12}$	1.83	2.55
3.	$6x10^{12}$	1.86	2.71
4.	$1x10^{13}$	1.87	2.13
5.	$3x10^{13}$	2.02	2.52
6.	$1x10^{14}$	2.04	2.8

Urbach energy of all the samples were calculated and tabulated in table 4.6. In the case of samples annealed at 50°C, the Urbach energy decreased as the fluence increased, showing annihilation of the defects in the samples. An increase in optical band gap was also observed [Table 4.5]. On annealing the samples at 100°C, the Urbach energy increased, i.e. on annealing, the defects in the samples increased. Interestingly the band gap of the material did not decrease. But it increased, on annealing at 100°C. In this case, the increase in band gap due to quantum size effect cannot be ruled out, since the samples obtained after 100 °C annealing was amorphous. The average grain sizes of the samples annealed at 100 °C, irradiated with fluences $6x10^{12}$, $1x10^{13}$, $3x10^{13}$ and $1x10^{14}$ ions/cm^2 were 5.2, 15, 5 and 13 nm respectively and hence the increase in band gap of the samples was attributed due to the quantum size effect.

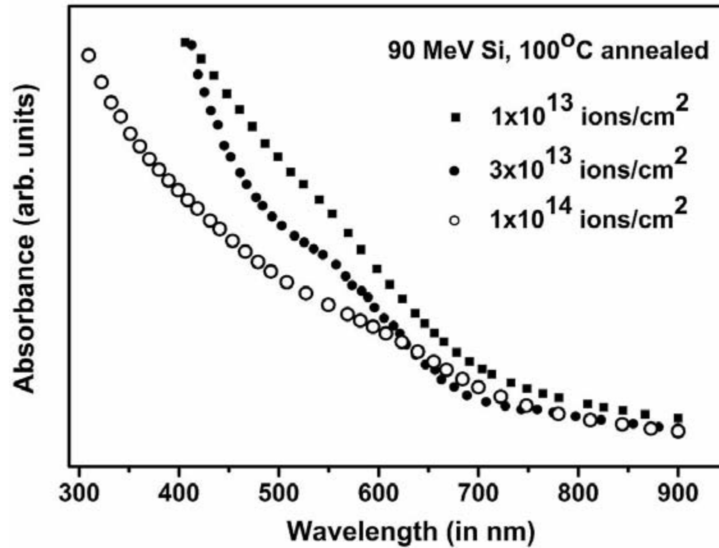

Figure 4.29 Absorption spectra of In/Se samples irradiated with 90 MeV Si ions and annealed at 100°C for 1 h.

Table 4.6: Urbach energy of the samples irradiated with 90 MeV Si ions and annealed at 50 and 100°C.

Sl. No.	Irradiation fluence (ions/cm^2)	Urbach energy (eV)	
		Annealed at 50 °C	Annealed at 100 °C
1.	Un-irradiated	1.67	1.04
2.	$3x10^{12}$	0.958	2.42
3.	$6x10^{12}$	0.887	2.34
4.	$1x10^{13}$	0.857	0.879
5.	$3x10^{13}$	0.777	1.71
6.	$1x10^{14}$	0.683	1.36

4.13 Conclusion

Threshold fluence for ion beam mixing (IBM) to take place between In/Se bilayer system was found out at different electronic energy regime. Threshold fluence for mixing using 100 MeV Ag, 80 MeV Ni and 90 MeV Si ions were $6x10^{12}$, $1x10^{13}$ and $1x10^{14}$ ions/cm^2 respectively. SHI irradiation study proved that the optical band gap of indium selenide can be tuned/ varied from 1.8 eV to 2.5 eV, without any post annealing treatment. With a post annealing treatment at 100° C for 1 h, band gap can be enhanced up to 2.88 eV. Annihilation of the localized defect levels situated near conduction and valence band edges resulted in increase in band gap.

References

1. Sankar Dhar, V. N. Kulkarni, Thin Solid Films, **333** (1998) 20.
2. Wei Kan Chue, James W Mayer and Marc A. Nicolet, Backscattering Spectrometry, Academic Press Inc. Florida (1978) p-23
3. Cameron J. R. Phys. Rev. **90** (1953) 839.
4. G. Mezey, J. Gyulai, T. Nagy, E. Kotai and A. Manuaba, Ion beam surface layer analysis, Editors : O. Meyer, G. Linker and F. Kappeler, Plenum Press, New York, (1976) p. 303.
5. S. Petersson, P. A. Tove, O. Meyer, B. Sundqvist and A. Johnson, Thin Solid Films, **19** (1973) 157.
6. M. Levalois and P. Marie, Nucl. Instr. and Meth. B **156** (1999) 64.
7. Wolfgang Bolse, Beate Schattat Nucl. Instr. and Meth. B **190** (2002) 173.
8. P. C. Srivastava, S. P. Pandey, O. P. Sinha, D. K. Avasthi, K. Asokan, Nucl. Instr. And Meth. B **156** (1999) 105.
9. T. Som, B. Satpathi, P. V. Satyam, D. Kabiraj, D. K. Avasthi, Nucl. Instr. And Meth. B **212** (2003) 206.
10. Maninder Singh Kamboj, G. Kaur, R. Thangaraj and D. K. Avasthi, J. Phys. D: Appl. Phys. **35** (2002) 477.
11. S. Sorieul, J-M Costantini, L.Gosmain,G. Calas, J-J. Grob and L. Thom´e, J. Phys.: Condens. Matter **18** (2006) 8493.
12. M. Kumar, F. Singh, S. A. Khan, V. Baranwal, S.Kumar, D. C. Agarwal, A. M. Siddiqui, A. Tripathi, A. Gupta, D. K. Avasthi and A. C. Pandey, J. Phys. D: Appl. Phys. **38** (2005) 637.
13. T. Som, P. Ayyub, D. Kabiraj, N. Kulkarni, V. N. Kulkarni and D. K. Avasthi, J. Appl. Phys. **93** (2003) 903.
14. D. K. Avasthi, W. Assman, H. Nolte, H. D. Mieskes, H. Huber, E. T. Subramanyam, A. Tripathi and S. Ghosh, Nucl. Instr. And Meth. B **156** (1999) 143.
15. C. Dufour, Ph. Bauer, G. Marchal, J. Grilhe, C. Jaouen, J. Pacaud and J. C. Jousset, Europhys. Lett. **21** (1993) 671

16. R. Lagnay, A. Dunlop, F. Dunstter and N. Lorenzelli, Nucl. Instr. and Meth. B **106** (1995) 28.
17. Alejandro Crespo-Sosa, Manuel Munoz and Juan-Carlos Cheang-Wong, Materls. Sci. and Eng. B **100** (2003) 297
18. Sarvesh Kumar, R. S. Chauhan, R. P. Singh, W. Bolse and D. K. Avasthi et al. Nucl. Instr. and Meth. B **212** (2003) 242
19. S. K. Srivastava, D. Kabiraj, B. Schattat, H. D. Carstanjen and D. K. Avasthi, Nucl. Instr. and Meth. B **219** (2004) 815
20. Ajay Gupta, Suneel Pandita, D. K. Avasthi, G. S. Lodha and R. V. Nandedkar, Nucl. Instr. and Meth. B **146** (1998) 265
21. R. Sreekumar, P. M. Ratheesh Kumar, C. Sudha Kartha, K. P. Vijayakumar, D. Kabiraj, S. A. Khan, D. K. Avasthi, Y. Kashibawa, T. Abe, Semicond. Sci. and Technol. **21** (2006) 382.
22. K. Bindhu, M. Lakshmi and C. Sudha Kartha, Semi. Conduc. Sci. and Technol. **17** (2002) 270.
23. S. Rath and S. N. Sahu, Europhys. Lett. **67** (2004) 294
24. B. N. Dev, Current science, **80** (2001) 1550.
25. Sankar Kumar and V. N. Kulkarni, Thin Solid Films **333** (1998) 20.
26. C. Detavernier, R. De Gryse, R. L. Van Meirhaeghe, F. Cardon, Guo-ping Ru, Xin-Ping Qu, Bing-Zong Li, R. A. Donaton and K. Maex, J. Vac. Sci. Technol. A **18(2)** (2000) 470.
27. E. Snoeks, A. Polman and C. A. Volkert, Appl. Phys. Lett. **65** (1994) 2487.
28. Veenu sisodia, R. K. Jain, D. bhattacharaya, D. Kabiraj and I. P. Jain, Radiation Measurements, **36** (2003) 657.
29. Sarvesh Kumar, P. K. Sahoo, R. S. Chauhan, D. Kabiraj, Umesh Tiwari, D. Varma and D. K. Avasthi, Nucl. Instr. And Meth. B, 212 (2003) 238.
30. D.K. Avasthi, Current Science **78** (2002) 1297
31. P. P. Patil, Neelima Kulkarni, S. V. Ghaisas, S. B. Ogale, V. G. Bhide and S. K. Date, Hyperfine Interactions, **35** (1987) 919
32. Iztok Arčon, Miran Mozetič, Anton Zalar, Alojz Kodre and Jacek Jagielski, Nucl. Instr. and Meth. B, **199** (2003) 222.

33. Wei Kan Chue, James W Mayer and Marc A. Nicolet, Backscattering Spectrometry, Academic Press Inc. Florida (1978) p-192
34. Wei Kan Chue, James W Mayer and Marc A. Nicolet, Backscattering Spectrometry, Academic Press Inc. Florida (1978) p-204
35. R. L. Fleisher, P. B. Price, R. M. Walker, Nuclear Tracks in Solids, University of California Press, 1975
36. A. Akkermann, J. Levinson, D. Ilberg, Y. Lifshitz, Editor - R. Baragiola, Ionisation of Solids by Heavy Particles, NATO Advanced Study Institutes Series 306, Plenum Press, New York, 1992, p. 431
37. G. Schiwietz, E. Luderee, G. Xiao, P. L. Grande, Nucl. Instrum. Methods B **175** (2001) 1
38. F. Seitz, J. S. Koehler, Solid State Phys. **2** (1956) 305
39. Z. G. Wang, Ch. Dufour, E. Paumier, M. Toulemonde, J. Phys.: Condens. Matter **6** (1994) 6733
40. Wolfgang Bolse, Surface and Coatings Technology **158** (2002) 1.
41. Pratima Dhuri, Ajay Gupta, S. M. Chaudhari, D. M. Phase, D. K. Avasthi, Nucl. Instrum. Methods B **156** (1999) 148.
42. Ph. Bauer, C. Dufour, C. Jaouen, G. Marchal, J. Pacaud, J. Grilhe, J. C. Jousset, J. Appl. Phys. **81** (1997) 116
43. Saskia Kraft, Beate Schattat and Wolfgang Bolse, J. Appl. Phys. **91** (2002) 1129
44. J. F. Ziegler, J. P. Biersack and U. Littmark, PC Programme package TRIM95, 1995
45. S.T. Lakshmikumar and A.C. Rastogi, Sol. Energy Mater. Sol. Cells **32** (1994) 7.
46. M.A. Kenawy, H.A. Zayed and A.M.A. El-Soud, J. Mater. Sci.- Mater. Electron. **1** (1990) 115.
47. Y. Hasegawa, Y. Abe, Phys. Status Solidi A. **70** (1982) 615.
48. Former J.C.W, Turner.J.A, Noufi. R, Cohen. D, J. Electrochem. Soc. **132** (1985) 1319.
49. J. Herrero and J. Ortega, Solar Energy Mater. **16** (1987) 477.
50. B. Kobbi, D. Ouadjaout, N. Kesri, Vacuum **62** (2001) 321-324.

51. S. N. Sahu, Thin Solid Films **261** (1995) 98-106.
52. M. Yudasaka, T. Matsnoka and N. Nakanishi, Thin Solid Films **146** (1987) 65-73.
53. M.Parlak and C. Ercelebi, Thin Solid Films **322** (1998) 334-339.
54. K. Ando, A. Katsui, Thin Solid Films **76** (1981) 141.
55. M. Yudasaka, and N. Nakanishi, Thin Solid Films **156**(1988)145.
56. C. Amory, J.C. Bernede and S. Marsillac, J.Appl. Phys. **94** (2003) 6945.
57. O. A. Balitskii, V.P. Savchyn and V.D. Yukhymchuk, Semicond. Sci. Technol. **17** (2002) 1
58. M.Di. Giulio, G. Micocci, A. Rizzo and A. Tepore, J. Appl. Phys. **54** (1983) 5839.
59. R. Sreekumar, P. M. Ratheesh Kumar, C. Sudha Kartha, K. P. Vijayakumar, Y. Kashibawa, T. Abe, Sol. Energy Mater. Sol. Cells, **90** (2006) 2908
60. M. Levalois, P. Marie, Nucl. Instr. and Meth. B **156** (1999) 64-71.
61. A. Gupta, Vacuum **58** (2000) 16.
62. D. Bhattacharya, S. K. Srivastava, P. K. Sahoo, D. Kabiraj et al. Surf. Coat. Technol. **158-159** (2002) 59-63.
63. P. Dhuri, A. Gupta, S. M. Chaudhuri, D. M. Phase, D. K. Avasthi, Nucl. Instr. and Meth. B **156** (1999) 148.
64. I. Kasko, C. Dehm, L. Frey, H. Ryssel, Nucl. Instr. and Meth. B **80-81** (1993) 786.
65. Cullity B.D, Elements of X-ray Diffraction (Reading, M A: Addison-Wesley) (1978) 170.
66. J.I.Pankove, Optical process in semiconductors, Dover Publications, Inc. New York (1971) 34.
67. S.N. Sahu, S.N. Sarangi and K.K. Nanda, Physics of Semiconductor Nanostructures, Editted by K.P. Jain, Narosa Publishing House, (1997) 202-216.
68. F.M. Gashlmzade, N.B. Mustafaev, Z. Phys. B: Condens. Matter **99** (1996) 219.

69. R. Sreekumar, P.M. Ratheesh kumar, C. Sudha Kartha, K.P. Vijayakumar, D. Kabiraj, S.A. Khan and D. K. Avasthi, Nucl. Instrum. Methods B **224** (2006) 190
70. W. F. Van der Weg, D. Sigurd, J. H. Mayer and S. T. Picraux (Editor), Application of ion beams to metals, Plenum Press, New York (1974) p-209
71. D. H. Lee, R. R. Hart, D. A. Kiewit and O. J. Marsh, Phys. Stat. Sol. A **15** (1973) 645
72. Y. T. Chang, Mater. Sci. Rep. **5** (1990) 45
73. M. Nastasi, J. W. Mayer, mater. Sci. Eng. R **12** (1994) 1
74. W. Bolse, Mater. Sci. Eng. R **12** (1994) 53
75. W. Bolse, Mater. Sci. Eng. A **253** (1998) 194
76. B. Schattat, W. Bolse, S. Klaumunzer, F. Harbsmeier and A. Jasenek, Appl. Phys. A **76** (2002) 165
77. S. Dhar, T. Som, Y. N. Mohapatra and V. N. Kulkarni, Appl. Phys. Lett. **67** (1995) 1700
78. S. Dhar, T. Som and V. N. Kulkarni, J. Appl. Phys. **83**(1998) 2363
79. S. Dhar, M. Milosavljevic, N. Bibie and K. P. Lieb, Phys. Rev. B **65** (2001) 024109
80. W. Bolse, Nucl. Instrum. Methods B **141** (1998) 133
81. W. Bolse, Nucl. Instrum. Methods B **148** (1999) 83
82. W. Bolse, Surface Coatings and Technology **158-159** (2002) 1
83. P. Sigmund, Rev. Roumaine Phys. **17** (1972) 823
84. P. Sigmund, A. Gras-Marti, Nucl. Instrum. Methods **182-183** (1981) 25
85. Z. G. Wang, C. Dufour, S. Euphrasie and M. Toulemonde, Nucl. Instrum. Methods B **209** (2003) 194.
86. S. Euphrasie, Rapport de\ stage, CIRIL, France 1998.
87. C. Dufour, E. paumier and M. Toulemonde, Nucl. Instrum. Methods B **122** (1997) 445.
88. M. Toulemonde, C. Dufour and E. Paumier, Phys. Rev. B. **46** (1992) 14362.
89. L. Cliché, S. Roorda, M. Chicoine and R. A. Masut, Phys. Rev. Lett. **75** (1995) 2348

90. E. Snocks, A. Polman and C. A. Volkert, appl. Phys. Lett. **65** (1994) 2487.
91. J. P. Singh, R. Singh, D. Kanjilal, N. C. Mishra and V. Ganesan, J. Appl. Phys. **87** (2000) 2742
92. L. Cliché, S. Roorda, M. Chicoine and R. A. Masut, Phys. Rev. Lett. **75** (1995) 2348.
93. L. P. Biro, J. Gyulai, K. havanesak, A. Yu Didyk, S. Bogen and L. Frey, Phys. Rev. B **54** (1996) 11853.
94. S. Sherman, S. Wagner, and R. A. Gottscho, Appl. Phys. Lett. **69** (1996), 3242
95. J. Cui, Rusli, S. F. Yoon, M. B. Yu, K. Chew, J. Ahn, Q. Zhang, E. J. Teo, T. Osipowicz, and F. Watt, J. Appl. Phys. **89** (2001) 2699
96. Rusli, J. Robertson, and G. A. J. Amaratunga, J. Appl. Phys. **80** (1996) 2998
97. C. Rincon, S. M. Wasim, G. Martin, R. Marquez, L. Nieves, G. Sanchez Perez, and E. Medina, J. Appl. Phys. **90** (2001), 4423
98. B. Gurbulak, Phys. Scr. **70** (2004) 197
99. H. T. El-Shair and A. E. Bekheet, J. Phys. D **25** (1992)1122
100. S. Chakrabarti, D. Ganguli, and S. Chaudhuri, Physica E **24** (2004) 333
101. K. Saito and A. J. Ikushima, Phys. Rev. B **62** (2000) 8584
102. B. Abay, H. S. Guder, H. Efeoglu, and Y. K. Yogurtcu, J. Phys. D **32**, (1999) 2942
103. R. Sreekumar, R. Jayakrishnan, C. Sudha Kartha, K. P. Vijayakumar, S. A. Khan and D. K. Avasthi, J. Appl. Phys. **103** (2008) 023709.

CHAPTER 5

Effect of SHI irradiation on γ-In_2Se_3 thin films

Abstract

This chapter deals with the effect of 90 MeV Si ions on γ-In_2Se_3 thin films. Study proved that the optical band gap of indium selenide can be enhanced using SHI irradiation without any considerable variation in structural and electrical properties. The increase in optical band gap was attributed to the annihilation of localized defect bands, near the conduction and valence band edges, on irradiation. It was observed that the sample, which had negative photoconductivity, exhibited positive photoconductivity, after irradiation.

5.1 Introduction

Indium selenide is a compound semiconductor, having direct band gap and belonging to III-VI group, which attracted researchers mainly due to its potential application in photovoltaic as well as in electro and photo-memory devices [1, 2]. Even though single crystal silicon solar cells are dominating the market, there is a focused attention towards compound semiconductor based solar cells because of the high cost and technology involved in the process of silicon solar cells. Among the compound semiconductors, indium selenide has made its mark in this field because of its application as window layer, absorber layer as well as a precursor for the preparation of copper indium selenide/copper indium gallium selenide based solar cells [3]. For photovoltaic device fabrication, one prefers crystalline and photoconductive samples, having low resistance. Abdinov and Kyazym-zade reported that InSe can exhibit negative photoconductivity [4]. Later we reported that γ-In_2Se_3 could also exhibit the same behaviour even at room temperature [5]. This can adversely affect the performance of the solar cell. Hence it is very important to study the photoconductivity of these films before switching on to solar cell fabrication.

Negative photoconductivity (NPC) of a semiconductor is defined as decrease in the conductivity under illumination. Ultimate reason for NPC is the combined effect of (i) trapping of photo excited carriers (electrons in n-type) (ii) destruction of minority carriers (holes in n-type) at recombination center followed by (iii) capture of electrons in the conduction band by the recombination center, during illumination [5]. Electron traps can adversely affect the photoconductivity. Removal of these traps will allow photo-generated carriers to reach conduction band, thereby enhancing the photoconductivity.

In_2Se_3 exists at least in five different phases such as α, β, γ, δ and κ with different structural and optical properties [6]. Depending upon the optical band gap of the film, it can be used as a window layer (CIS/In_2Se_3) [7] or absorber

layer (CdS/In_2Se_3) [4, 8] in solar cells. Gordillo et al. reported efficiency of 8.3% in CIS/In_2Se_3 solar cell with an open circuit voltage (V_{oc}) of 0.45 V and a fill factor of 0.6 [7]. They reduced the thickness of the In_2Se_3 film from 1µm to ~70 nm, to increase the band gap from 1.75 eV to 3 eV, to use it as a window layer [7]. This resulted in the increase of short circuit current density [J_{sc}], at the cost of the open circuit voltage V_{oc}. Optical band gap of indium selenide can be varied by altering the thickness [7] and also by varying annealing temperature [9]. But variation of thickness and annealing temperature can affect other properties of the film like sheet resistance [9, 10, 11], which can increase several orders. Hence a technique that is capable of altering the optical band gap of the material, without affecting its other important properties has great significance especially, from the point of view of technological applications.

It has been reported earlier that single phase film can be prepared using SHI irradiation [12]. Effects of SHI irradiation in metals, semi- conductors and insulators are entirely different. It is more sensitive to insulators than to metals and semiconductors [13, 14]. It can create point defects, columnar defects, amorphous track or a perturbed atomic distribution along its path as they pass through the material [15, 16]. SHI irradiations were used for controlled manipulation of optical, electrical and structural properties of materials [17, 18, 19]. SHI can also anneal out defects up to certain fluence, beyond which it creates defects in materials [20, 21]. In the present work, we used SHI to increase the photoconductivity and optical band gap of In_2Se_3 for the first time, without considerable variation in structural and electrical properties.

5.2 Experiment

Thin films of indium selenide were prepared by annealing In/Se bilayer systems, at different temperatures ranging from 100 °C to 400 °C, for duration of one hour, maintaining the pressure at $2x10^{-5}$ mbar. Thin films of selenium (150 nm thick) were first deposited on glass substrate using chemical bath deposition

technique [22], over which indium layer of thickness 56 nm was deposited with the help of resistive heating technique (using molybdenum boat) at a pressure of $2x10^{-5}$ mbar during evaporation.

Thickness of the films was measured employing stylus thickness profiler (Model – Dektak 6M). The samples annealed at different temperatures [100, 150, 200, 300 and 400°C] were named as IS100, IS150, IS200, IS300 and IS400 respectively. These samples were later irradiated using Si ions of energy 90 MeV (from 15UD Pelletron accelerator) having fluence of $2x10^{13}$ ions/cm^2 at room temperature, over an area of 1 cm^2, by using an electromagnetic scanner. Range of 90 MeV Si in In_2Se_3 is about 22 µm (calculated using TRIM code 95) [23], so that it passed through the film and got embedded in the substrate.

X-ray diffraction (XRD) patterns were recorded in the range of 2θ, 10° - 60° using Cu K_α radiation (λ=1.5405 Å) employing Rigaku (D.Max.C) X-ray diffractometer. Optical absorption spectra were recorded using UV-VIS-NIR spectrophotometer (Hitachi U-3410) in the range 400 to 900 nm. For photoluminescence (PL) measurements, samples were loaded in a closed cycle liquid He cryostat (Model - CSS 100/202, Make – Janis research Inc. USA) and cooled up to 10 K. Here the temperature was measured and controlled using a "Lakeshore autotuning" temperature controller. Continuous beam of wavelength 488 nm, from an Ar^+-ion laser, (Make – Melles Griot, Model: 35-LAL-415-230; Power: 150 mW) was used as the excitation source. Focused beam of excitation intensity 214 mW/cm^2 was used and the emission spectra were recorded employing spectrometer USB 2000 (Technosource International INC.).

Dark and photo conductivity of the samples were measured using a 'source measuring unit' (SMU-123X KEITHLEY) in the voltage range 0-5 V at room temperature. The two electrodes were patches of silver paint of size 0.6 x 0.2 cm^2, with a distance of 0.6 cm between them. Output from the sample was taken using magnanin wires, connected to the electrodes. A halogen lamp (output

power of 60 mW/cm^2) was used to illuminate the samples. The illumination time was approximately 60 s. Photoconductivity was measured after illuminating for 60 s. Low temperature photoconductivity measurements were performed by using a closed cycle liquid helium cryostat (Model-REF-396/D22, Make-Helix Technology Corporation, USA), along with "Lakeshore321 autotuning" temperature controller.

5.3 Results and discussion

5.3.1 X-ray diffraction analysis

Figure 5.1 shows the XRD pattern of samples annealed at different temperatures, ranging from 100 ^{o}C to 400 ^{o}C. Formation of γ-In_2Se_3 was confirmed even at 100 ^{o}C, through the peak at 29.76 degree, corresponding to (201) plane [JCPDS card: 40-1407]. Unreacted indium was also present in this sample. Annealing at 150 ^{o}C resulted in the complete diffusion of In into Se lattice [Fig. 5.1, IS150] resulting in the formation of β-In_2Se_3 along (110) plane [2θ = 45.18; JCPDS card: 72-1470]. Diffusion of In into Se resulted in crystallization of Se along (100) plane [confirmed by the peak at 23.27; JCPDS card: 6-0362]. This type of behaviour was reported earlier in In/Se bilayer system [9]. In the case of IS200 and IS300 films, indium mono-selenide (InSe) phase [along (006) plane; peak at 22.69; JCPDS card: 27-0244] was formed along with γ-In_2Se_3. However temperature of 400 ^{o}C was required for the formation of single-phase γ-In_2Se_3 along (006) and (111) planes [JCPDS card: 40-1407]. The average grain size of the samples was calculated using Debye Scherrer's formula [24] (see section 1.10.2),and the results are tabulated in table 5.1.

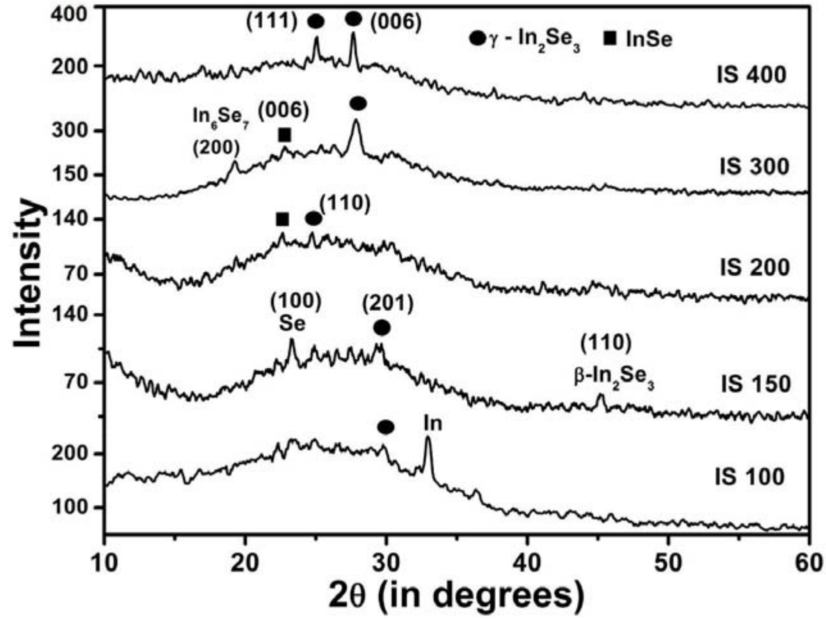

Figure 5.1: XRD pattern of In_2Se_3 samples prepared at different annealing temperatures from 100 °C to 400 °C

Table 5.1: Average grain size of the samples before and after irradiation. Crystal structure of β-In_2Se_3, γ-In_2Se_3 and InSe were rhombohedral, hexagonal defect wurtzite and hexagonal layered structure respectively.

Sample name	un-irradiated samples				Irradiated samples			
	2θ	FWHM	Average grain size	Phase	2θ	FWHM	Average grain size	Phase
IS100	29.76	0.43	191 Å	γ-In_2Se_3	28.38	0.22	372 Å	γ-In_2Se_3
IS150	45.18	0.61	141 Å	β-In_2Se_3	23.08	0.22	369 Å	InSe
IS200	22.69	0.63	129 Å	InSe	30.35	0.29	288 Å	γ-In_2Se_3
IS300	27.83	0.57	143 Å	γ-In_2Se_3	27.33	0.59	139 Å	γ-In_2Se_3
IS400	27.65	0.17	480 Å	γ-In_2Se_3	28.15	0.15	550 Å	γ-In_2Se_3

XRD patterns of the irradiated samples are depicted in figure 5.2. On irradiation with Si ions [90 MeV], the unreacted indium in IS100 got mixed with Se lattice, leading to the formation of indium mono-selenide (InSe) along with γ-In_2Se_3. Irradiating IS150 resulted in the elimination of γ- In_2Se_3 and β-In_2Se_3 phases completely, leading to the formation of single phase InSe. SHI induced single phase InSe formation was earlier reported in which we used 40MeV Si ions for irradiation [12]. But, in the case of IS200 and IS300, the irradiation favoured growth of γ- In_2Se_3 only, which was evident from the XRD spectra (Fig. 5.2). Average grain size of the irradiated samples is tabulated in table 5.1. It showed that 90 MeV Si ions of fluence $2x10^{13}$ ions/cm^2 did not cause any amorphisation in γ-In_2Se_3 thin films. Moreover it increased the average grain size of the samples except IS300. IS300 did not show any considerable variation in the average grain size. Increase in the average grain size of the crystallites also indicated the reduction in the density of grain boundaries present in the samples upon irradiation. XRD patterns (Fig. 5.1 and 5.2) of all the samples (irradiated

and un-irradiated) showed a broad X-ray scattering background at 2θ ~ 25°. This broad hump might be due to the backscattering from the glass substrate. Since our samples were only ~206 nm thick, there is a possibility of background scattering from the glass substrate.

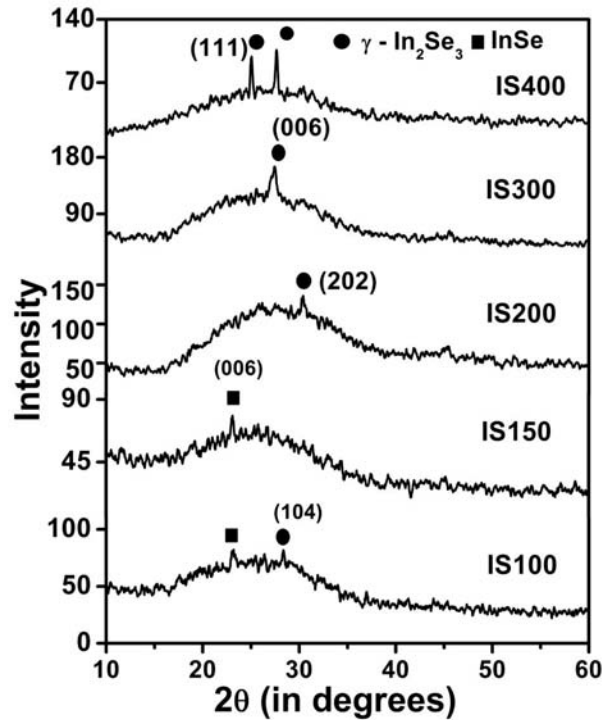

Figure 5.2: XRD pattern of samples irradiated by 90 MeV Si ion with a fluence of $2x10^{13}$ ions/cm^2.

XRD analysis showed that, irradiation using 90 MeV Si ions, eliminated secondary phase from indium selenide thin films. 90 MeV Si ions lose about ~ 4 keV/nm energy to In_2Se_3 as electronic energy loss (S_e) and about $3.5x10^{-3}$ keV/nm as nuclear energy loss S_n, calculated using TRIM code 95 [23]. S_n is negligible as compared to S_e and causes very little effects on In_2Se_3 films.

Electronic energy loss of ~ 4 keV/nm in In_2Se_3 might not be sufficient for amorphisation of these films. However, this is sufficient to increase the average grain size of the samples [Table 5.1]. Swift heavy ions transferred energy to the lattice via electron – phonon interaction, according to thermal spike model [25]. The energy lost by the SHI is mostly converted into the kinetic energy of the electrons, in the target material. This energy is dissipated to the lattice, via electron – phonon coupling, resulting in heating up of lattice. If the electronic energy deposited is sufficiently high, the temperature may rise above the melting point of the material and a molten cylinder, of diameter some nanometers, is formed. This can persist up to tens of picoseconds before rapid quenching of the melt to ambient temperature, resulting in defect rich or even amorphous cylindrical latent tracks. Track formation only occurs if the threshold electronic stopping energy (S_e) of the material is exceeded. Previous study using 40 MeV Si ions [12], in In/Se bilayer system showed that S_e (5.42 keV/nm in indium and 4.13 keV/nm in selenium) was not sufficient to produce a transient molten track in In/Se bilayer system. Hence an electronic energy 4 keV/nm of 90 MeV Si may not be sufficient to produce latent tracks in In_2Se_3 thin films. This may be the reason why we have no amorphisation even after irradiation with 90 MeV Si ions.

In our case, we observed an increase in average grain size of the samples after irradiation. This might be due to the annealing effect of SHI below the threshold S_e value [21, 26]. Kamarou et al. [21] found, in the case of pre-damaged InP, that 'damage-annealing' dominates the 'damage-formation' for sub-threshold energy (using 140 MeV Kr ion). But above the threshold energy (S_e) (using 390MeV Xe, 150 MeV Au and 600 MeV Au ions) irradiation caused higher damage in InP and observed hardly any effect of annealing. Similar case was reported in the case of GaAs and InP in which annealing was observed at low fluence with sub threshold energy [21, 26]. Hence the increase in average grain size of the indium selenide samples was attributed to the annealing of point

defects and the growth of small crystalline inclusions present in the film, leading to local crystallisation [26].

5.3.2 Optical studies

(a) Determination of band gap energy and Urbach energy

Optical absorption spectra of irradiated and unirradiated samples were recorded in the range of 400 to 900 nm. The unirradiated samples showed multiple absorptions in the ranges 650-850 nm and 500-600 nm, whereas the irradiated samples showed only one absorption each in the range 500 – 650 nm (for IS100 and IS150) and in the range 400 – 550 nm (for IS200, IS300 and IS400), respectively. Figure 5.3 shows the absorption spectra of IS100 before and after irradiation. In the case of unirradiated IS100 [Fig. 5.3(a)], clear extrinsic absorption could be seen, indicating the presence of strong levels, existing below the conduction band. But on irradiation, these levels got eliminated [Fig. 5.3(b)].

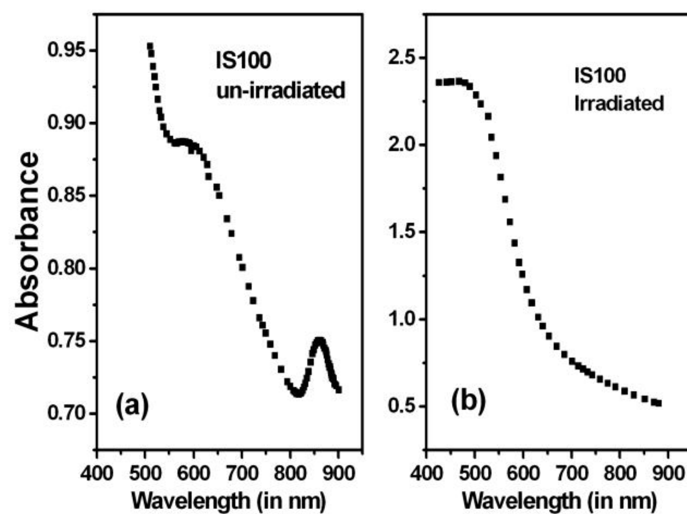

Figure 5.3: Absorption spectra of IS100 (a) before and (b) after irradiation

The optical band gap (E_g) of the samples was determined by extrapolating the straight line portion of $(\alpha h\upsilon)^2$ versus $h\upsilon$ plot to $\alpha = 0$ [27], where $h\upsilon$ is the incident photon energy and α is optical absorption coefficient, determined from the absorption spectra. Extrapolating the other straight line portions of $(\alpha h\upsilon)^2$ versus $h\upsilon$ plot to $\alpha = 0$, gave the indications of defect levels and/or the band gap of the secondary phase present in the sample [5, 9, 27]. .The optical band gap of irradiated and unirradiated samples is tabulated in table 5.2.

Table 5.2: Optical band gap of the samples before and after irradiation.

Sl.	Sample name	Optical band gap	
		Un-irradiated	Irradiated
1.	IS100	1.84eV	2.02eV
2.	IS150	1.81eV	2.31eV
3.	IS200	2eV	2.74eV
4.	IS300	2.04eV	2.71eV
5.	IS400	2eV	2.8eV

Figure 5.4 shows the $(\alpha h\upsilon)^2$ versus $h\upsilon$ plot of IS100 (band gap=1.84 eV). Extrapolating the straight line portions of this plot to α=0, one could get three more activation energies 1.42 eV (level-A), 1.26eV (level-B) and 1.08 eV, corresponding to defect levels present in the forbidden energy gap in this sample. The defects at 1.42 eV and 1.26 eV were already attributed to light activated electron traps [5]. IS150 showed the band gap of β and γ-phase present in the sample corresponding to an energy 1.7 eV and 1.81 eV respectively (Fig. 5.1, IS150) [9]. But IS200 and IS300 (with band gap=2.02 and 2.04 eV respectively) showed a defect level at 1.65 eV above the valence band (Fig. 5.5).

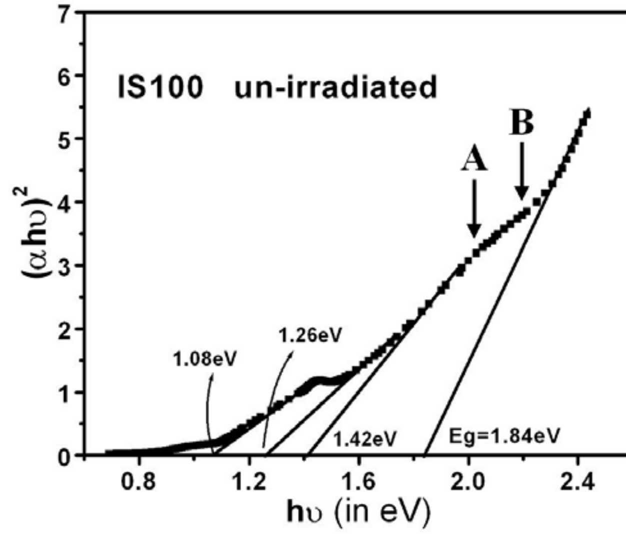

Figure 5.4 $(\alpha h\nu)^2$ versus hν plot of IS100 **before** irradiation

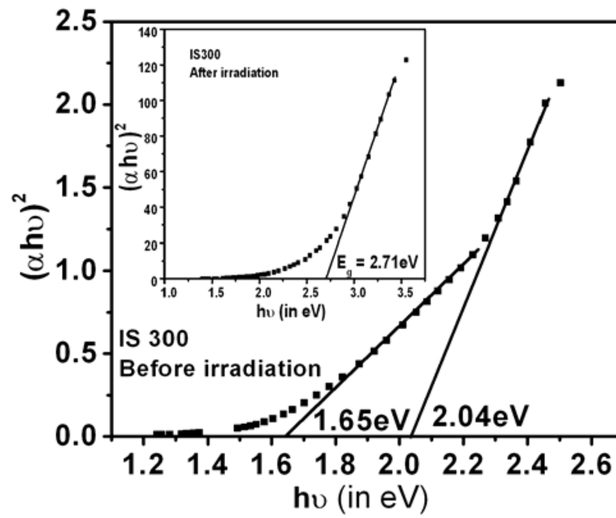

Figure 5.5: $(\alpha h\nu)^2$ versus hν plot of IS300 **before** irradiation. Inset shows the plot after irradiation.

Figure 5.6 depicts the optical absorption spectra of IS400. In addition to the absorption in the range 500 nm – 650 nm (2 eV; band to band absorption) this sample had an additional absorption in the range 700 nm – 850 nm [1.62 eV]. As IS400 did not show any secondary phase in XRD analysis (Fig. 5.1), this absorption might be due to the defect level, present in the sample. From $(\alpha h\upsilon)^2$ versus $h\upsilon$ plot of this sample, (inset of Fig. 5.6), the defect level was identified at 1.62 eV above the valence band. But on irradiation, the absorption spectra indicated that this defect level [at 1.62 eV] was annealed out (Fig. 5.6). An increase of band gap from 2 eV to 2.8 eV was also observed on irradiation.

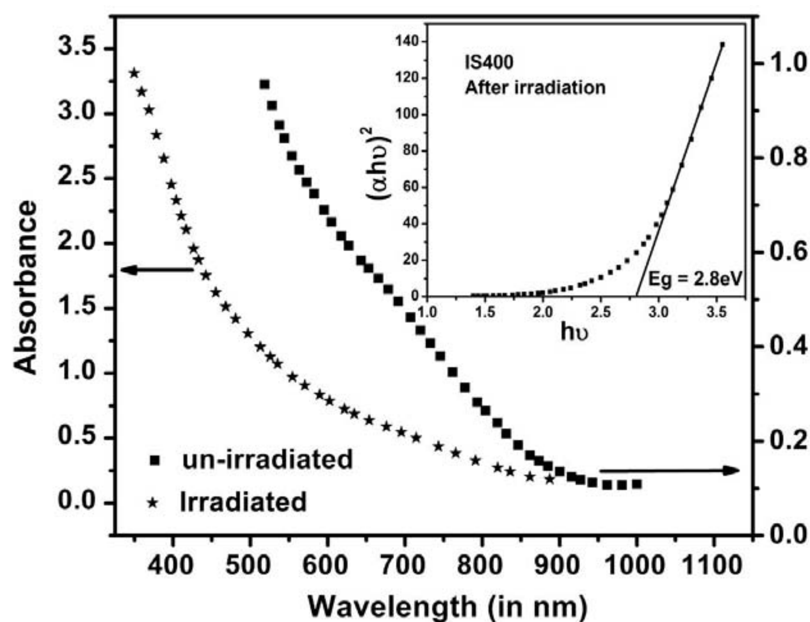

Figure 5.6: Absorption spectra of IS400 **before and after** irradiation. Inset shows $(\alpha h\nu)^2$ versus $h\nu$ plot of IS400 before irradiation.

For all the samples, irradiation caused an increase in optical band gap, with the maximum increase of about 40% in the case of IS400 (Table 5.2). One of the factors, which could affect the optical band gap, is the quantum size effect [12, 29]. If the grain size of the samples was reduced to the order of few nano meters, optical band gap should increase. But here XRD analysis revealed that, the grain size actually increased on irradiation (Table 5.1), proving that quantum size effect was to be ruled out. Hence this could be explained in the following way. In the case of intrinsic semiconductors, there would be no defect levels in the forbidden gap, making the absorption possible only when a photon of energy greater or equal to band gap was incident on it, leading to band-to-band transition. But in the case of impurity semiconductors, there could be defect levels in forbidden gap, resulting in the absorption of photons with sub band gap energies. There can also be dense localized energy states, near the valence and conduction band edges, known as 'Urbach energy bands', whose density decays exponentially as one moves away from valence and conduction band edges [29, 30]. Different semiconductors, namely a-SiC [32], a-C:H [33] and even chalcogenide compounds such as $CuInSe_2$ [34] and InSe [35] exhibited Urbach tail. Urbach energy width (tail width) is a measure of disorder in the material [33]. Figure 5.7 shows the sketch of the assumed band structure, with dense localized energy states near band edges. Because of the presence of these states, it was very difficult to distinguish between the bottom of the conduction band and the top of the valence band with the band tails, and this resulted in absorption spectrum, showing absorption even at energies much below the band gap [for example the absorption spectrum of IS100 in Fig. 5.3(a)]. In this figure, we could observe a broad shoulder in the range 550 nm - 650 nm, which strongly indicated the presence of dense state near the conduction band (see region marked A-B in Fig. 5.4). According to Urbach rule [28, 36], below the fundamental absorption edge, the absorption coefficient α varies exponentially as $\alpha = \alpha_o \exp (h\upsilon/E_u)$, where '$\alpha_o$' is the characteristic parameter of the material, '$h\upsilon$' the photon energy and 'E_u', the width of the exponential tail, known as the Urbach energy or Urbach tail energy. This region is attributed to the electronic

transition between a localized band tail and an extended band [31]. This represents the degree of disorder in the material. The Urbach tail width (E_u) can be estimated from the inverse slope of the plot '(ln α) versus hυ' below the fundamental absorption [28].

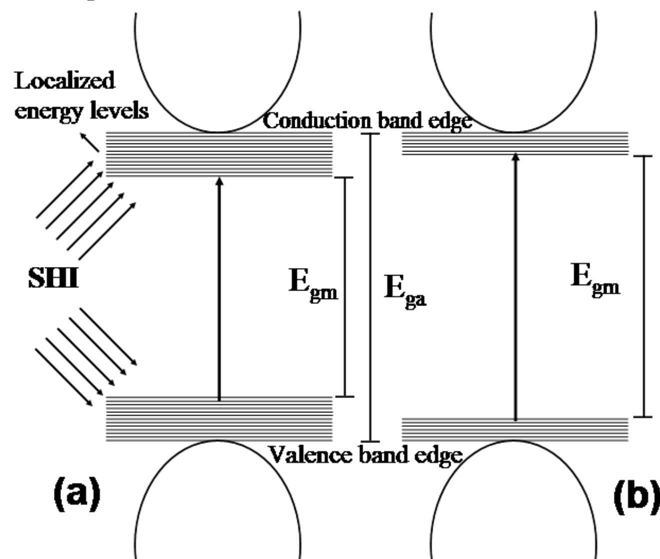

Figure 5.7: Sketch of the assumed band structure with dense localized bands, (a) before and (b) after irradiation.

Figure 5.8 shows the same plot ('(ln α) versus hυ') of IS200, before and after irradiation. E_u of all the samples before and after irradiation with 90MeV Si ions was calculated and tabulated (Table 5.3). One could observe that the Urbach tail width decreased for all samples except IS150, after irradiation. The decrease of Urbach tail width shows that irradiation could anneal out the disorders (localized states) in the material, which resulted in the increase of band gap of the material. Similar type of annealing out of disorders and subsequent increase of band gap was observed in In_2Se_3 by El-Shair et al. by thermal annealing at higher temperatures [36]. Increase in Urbach tail width in the case of IS150 after

irradiation might be due to the creation of planar defects during irradiation, since InSe has a hexagonal layered structure. Abay et al. [37] observed a decrease in Urbach energy in InSe due to the reduction of planar defects. One point to be noted here is that, the samples, except IS100 and IS150, were formed with single phase γ-In_2Se_3, which has a hexagonal defect wurtzite structure [6].

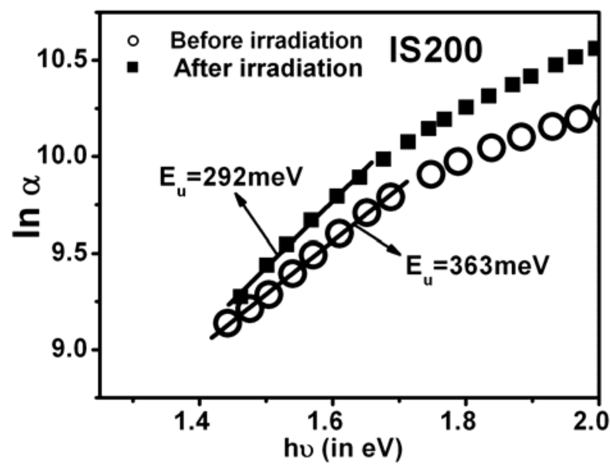

Figure 5.8: ln α versus hυ plot of IS200 before and after irradiation.

Table 5.3: Variation of Urbach energy with irradiation.

Sl.	Sample name	Urbach energy	
		Before irradiation	After irradiation
1.	IS100	2.04eV	858meV
2.	IS150	450meV	498meV
3.	IS200	363meV	292meV
4.	IS300	400meV	320meV
5.	IS400	418meV	343meV

When we measured the optical band gap of the material, because of the band tailing, we were able to measure only the band gap Eg_m. This was very much less than the actual band gap Eg_a of the material (Fig. 5.7(a)). Optical absorption study revealed that irradiation could anneal out defects from forbidden energy region. Urbach tail width measurements on the irradiated sample showed annealing out the localized energy bands near the band edges, which indicated a reduction in E_u. As a result of this, conduction and valence band tail states were separated further apart in energy (Fig. 5.7(b)), which was evident from blue shift in absorption spectra (Fig. 5.6). This might be the reason for the increase in band gap of indium selenide samples. It is also worth mentioning here that the highest optical band gap already reported for In_2Se_3 was ~3eV, which is very close to the value obtained in the present study [7].

(b) Photoluminescence

Figure 5.9 shows the PL spectra of IS100 before and after irradiation. The emission at 746 nm (peak-X, Fig. 5.9) was attributed to the transition to a

recombination center 1.66 eV (level-C) below the conduction band [5, 10]. (Interestingly the third activation energy (1.08 eV) obtained in IS100 from optical absorption study exactly coincides with energy between level B and level C, and hence attributed as the transition from level C to level B). The emission at 675 nm (1.84 eV) was attributed to the transition from defects below the conduction band to the defect states above the valence band (peak-Y), since the measured band gap of unirradiated IS100 was 1.84 eV (Fig. 5.4). Band gap increased from 1.84 eV to 2.02 eV and a shift in PL emission towards lower wavelength [from 675 nm to 664 nm, corresponding to energy of 1.87 eV], was also observed on irradiation. But it is to be specifically mentioned here that the emission at 1.66 eV remained without any change. This indicated that irradiation was not affecting the recombination center, while annihilation of localized states near band edges caused the shift of emission at 1.84 eV to 1.87 eV. The full width at half maximum (FWHM) of the peak-Y reduced from 85.5 nm to 47.5 nm, on irradiation. The blue-shift and the reduction of FWHM of PL peak were due to the annihilation of localized states near band edges [32, 33], which ultimately resulted in increasing optical band gap of the material. Earlier Kamboj et al reported annihilation of defects induced by 40 MeV Si ions in $Se_{80-x}Te_{20}Pb_x$ in which an increase in band gap from 1.36 eV to 1.48 eV was also observed [38]. But Sorieul et al. [18] observed a decrease in optical band gap of α-SiC single crystals due to heavy ion irradiation (4 MeV Xe and 4 MeV Au ions) and this was attributed to the creation of localized states in the forbidden energy region. They also found that Urbach energy was increasing with the irradiation fluence. The increase of Urbach energy reflected the introduction of disorders/defects in α-SiC, which ultimately resulted in reduction of optical band gap [18]. But in our case, Si ions of energy 90 MeV, annealed out the defects/disorders in In_2Se_3, which was evident from x-ray diffraction and optical absorption studies. Urbach energy also decreased on irradiation, and this again supported our argument.

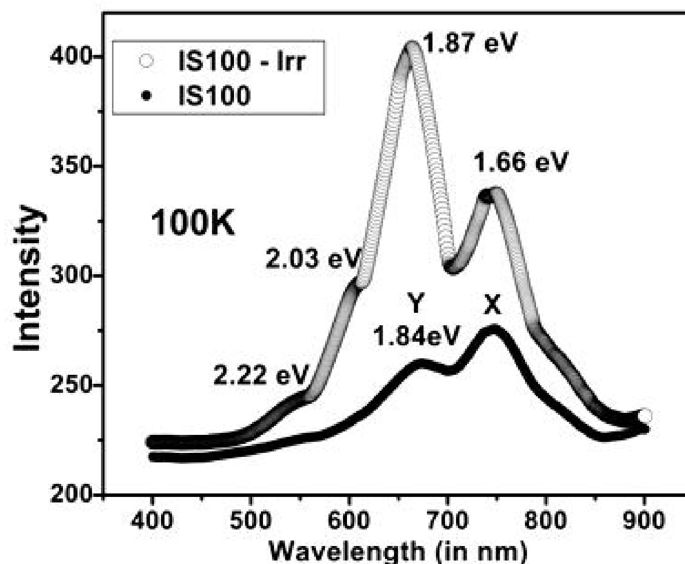

Figure 5.9: PL spectra of IS100 (●) before and (○) after irradiation.

In the case of IS400, one could observe a large blue shift in absorption spectra, induced by irradiation [Fig. 5.6]. Figure 5.10 shows the PL spectra of the sample IS400 recorded at 100 K before and after irradiation. This also showed a blue-shift. The unirradiated sample showed an emission at 631 nm (1.97 eV). As the band gap of IS400 was 2 eV, the emission at 1.97 eV is attributed to the band-to-band (i.e., defect tail-to-defect tail) recombination. On irradiation, the emission was shifted to 594 nm and an additional emission at 495 nm corresponding to 2.51 eV, was also observed. Higher energy emission at 2.45 eV is reported in κ-In_2Se_3,[10] but XRD analysis did not show any presence of κ phase [Fig. 5.2]. At higher temperatures, emission at 495 nm vanished and a broad peak at 584 nm (2.13 eV) was observed (inset of figure 5.10). Hence the shift of PL emission, from 631 nm to 584 nm, again shows the annihilation of localized states near band edges, as the cause of this shift.

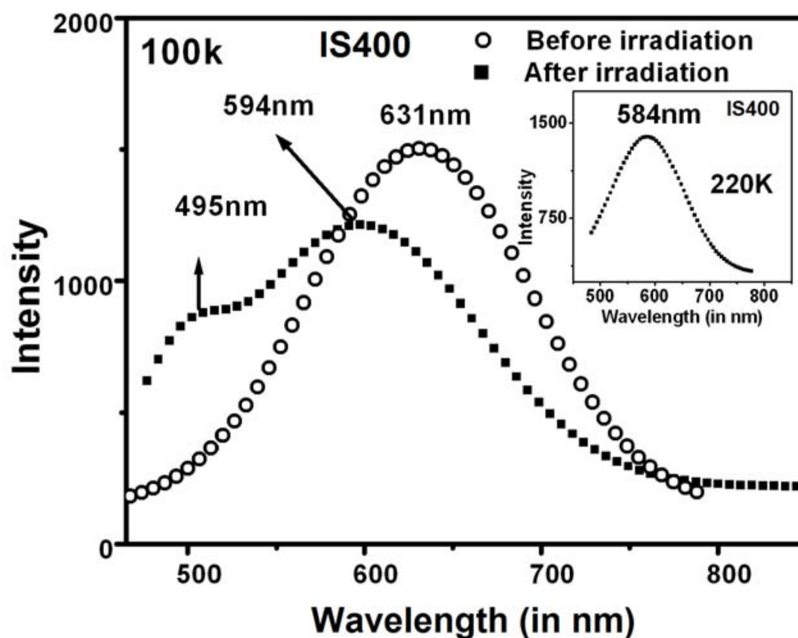

Figure 5.10: PL spectra (recorded at 100 K) of IS400 before and after irradiation with 90MeV Si ions. Inset shows the PL spectra recorded at 220 K of IS400 after irradiation.

In addition to the emission at 1.87 eV and 1.66 eV, two more broad emissions were observed at 611 nm and 559 nm, [corresponding to energies 2.03 eV and 2.22 eV respectively] on irradiation of IS100 (Fig. 5.9). The emission at 2.03 eV might be probably, the band-edge emission while the broad emission centered at 2.22 eV might be from the tiny amount of κ-In_2Se_3 phase present in the film [10]. But again XRD analysis did not show any sign of the κ phase (Fig. 5.2). Irradiation annealed out the defects present in the forbidden gap. This allowed more photo-generated carriers to reach the conduction band, which participated in the recombination process too. This might be the reason for the increase in PL intensity of the peaks X and Y [Fig. 5.9] [5]. One interesting point to be noted is

the dominance of the PL peak Y over X on irradiation. This suggested that the destruction of minority carriers by the recombination center (at 1.66 eV) was more in the unirradiated sample than in irradiated sample.

5.3.3 Electrical study

(a) Room temperature photoconductivity

Dark and photo conductivity of irradiated and unirradiated samples were measured at room temperature and tabulated in table 5.4. Irradiation caused only marginal increase in sheet resistance of the films. Increase in photosensitivity S, [S = $(I_l-I_d) / I_d$], (ie, the ratio of difference between photocurrent (I_l) and dark current (I_d) to the dark current) was clearly seen for all the samples. Here we could observe a conversion of photoconductivity/photosensitivity from negative to positive in IS100 upon irradiation.

Table 5.4: Variation of photosensitivity and Sheet resistance before and after irradiation.

Sl.	Sample name	Photosensitivity		Sheet resistance (in ohm cm)	
		Un-irradiated	Irradiated	Un-irradiated	Irradiated
1.	IS100	- 0.04	0.3	1.9 k	5.83 k
2.	IS150	0.11	1.04	8.11 k	8.23 k
3.	IS200	0.07	1.3	2.05 k	83.2 k
4.	IS300	0.06	0.22	3.9 k	6.76 k
5.	IS400	0.37	0.48	6.1 k	9.24 k

Figure 5.11 shows the photoconductivity spectrum of IS100, before and after irradiation. For the unirradiated sample, when the light was turned on, the current decreased to a lower value, below the dark current and when the light was turned off, the current increased back to the dark current. But in the case of

irradiated sample (IS100) we could observe that the conductivity was positive on illumination (Fig. 5.11(b)). From this observation, one could find that irradiation caused the photoconductivity to change from negative to positive, probably due to the annealing out of the defects, which were responsible for negative photoconductivity.

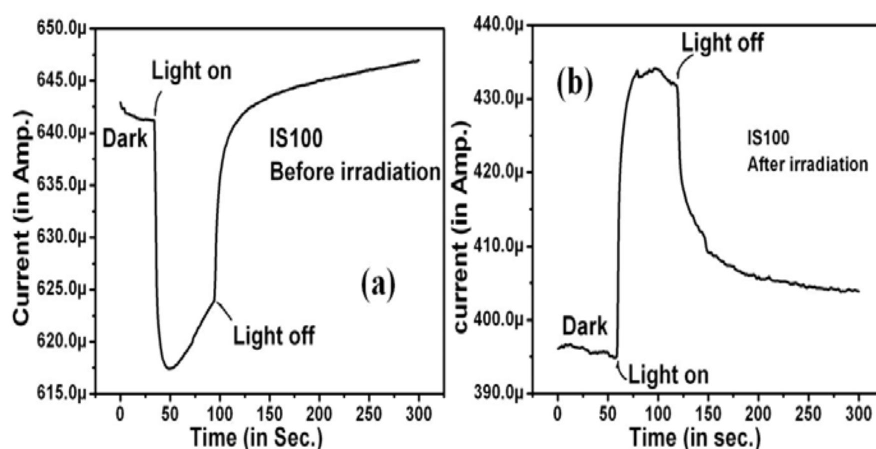

Figure 5.11: Photoconductivity spectra of IS100 (a) before and (b) after irradiation.

To explain the negative photoconductivity in IS100, earlier we used a model for γ-In_2Se_3 (Fig. 5.12) [chapter 3, section 3.4.4]. Blocking of excited electrons from reaching the conduction band by the levels A and B and the recombination taking place at level C were the most important processes leading to the negative photoconductivity of γ-In_2Se_3 at room temperature [5] (for more details please see chapter 3). Optical absorption study revealed the annihilation of trap levels at 1.42 eV (level A) and 1.26 eV (level B) in the case of IS100 upon irradiation. Annihilation of these trap levels A and B allowed photo-generated carriers to reach conduction band, which resulted in increasing the photosensitivity. Photoluminescence study also revealed that, on irradiating IS100 (Fig. 5.9) PL

emission peak Y dominated the peak X, which suggested that the destruction of minority carriers at recombination centre was reduced considerably on irradiation. Low photosensitivity registered for IS200 and IS300 might be due to the presence of light activated electron trap (1.65 eV) in the sample. Annealing of this trap, due to SHI irradiation, resulted in the increase of photosensitivity. Grain boundaries in the sample may also act as electron traps. Irradiation using 90 MeV Si ions increased the average grain size of the crystallites thereby reducing the density of grain boundaries. This might have helped the photo-generated carriers to survive, resulting in the increase of the photosensitivity/photoconductivity. Thus by controlled dense electronic energy deposition using SHI irradiation, one could eliminate electron traps and enhance the photoconductivity and optical band gap of γ-In_2Se_3 with a marginal increase of sheet resistance.

Figure 5.12: Band structure of IS100 before irradiation.

5.4 Conclusion

Through SHI irradiation, using 90 MeV silicon ions, one could increase optical band gap and photoconductivity of γ-In_2Se_3 without decreasing the thickness and considerable variation in resistance. Annihilation of defects, which trapped photo-excited electrons, may be the reason for increase in photoconductivity. Annealing of traps at 1.42 eV and 1.26 eV above the valence band in IS100 converted the photoconductivity from negative to positive. Optical band gap of γ-In_2Se_3 can be increased from 2 eV to 2.8 eV due to irradiation. Annihilation of localized defect levels near the band edges increased the optical band gap of the material.

References

1. S.T. Lakshmikumar and A. C. Rastogi, Sol. Energy Mater. Sol. Cells **32** (1994) 7.
2. A. Sh. Abdinov and Kyazym-Zade, Sov. Phys. Semicond. **9**, (1975) 1113.
3. C. Amory, J. C. Bernede E. Halgand and S. Marsillac, Thin Solid Films **431-432** (2003) 22.
4. A . Sh. Abdinov and A. G. Kyazym-zade, Sov. Phys. Semicond. **10** (1976) 47.
5. R. Sreekumar, R. Jayakrishnan, C. Sudha Kartha and K. P. Vijayakumar, J. Appl. Phys. **100** (2006) 33707.
6. C. Amory, J. C. Bernede and S. Marsillac, J. Appl. Phys. **94** (2003) 6945.
7. G. Gordillo and C. Calderon. Sol. Energy Mater. Sol. Cells **77** (2003) 163.
8. M.A. Kenawy, H.A. Zayed and A.M.A. El-Soud. J. Mater. Sci.- Mater. Electron. **1** (1990) 115.
9. R. Sreekumar, R. Jayakrishnan, C. Sudha Kartha, K. P. Vijayakumar, Y. Kashiwaba and T. Abe, Sol. Energy Mater. Sol. Cells **90** (2006) 2908.
10. A. Chaiken, K. Nauka, G. A. Gibson, Heon Lee, C. C. Yong, J. Wu, J. W. Ager, K. M. Yu and W. Walukiewicz, J. Appl. Phys. **94**, 2390 (2003).
11. M. Yudasaka, T. Matsuoka and K. Nakanishi, Thin Solid Films **146** (1987) 65.
12. R. Sreekumar, R. Jayakrishnan, C. Sudha Kartha, K. P. Vijayakumar, S. A. Khan and D. K. Avasthi, Nucl. Instr. and Meth. B **244** (2006) 190.
13. Saskia Kraft, Beate Schattat and Wolfgang Bolse, J. Appl. Phys. **91** (2002) 1129.
14. K. Nordlund, M. Ghaly and R.S Averback, J.Appl. Phys. **83** (1998) 1238.
15. M. Levalois and P. Marie, Nucl. Instr. and Meth. B **156** (1999) 64.
16. Wolfgang Bolse and Beate Schattat Nucl. Instr. and Meth. B **190** (2002) 173.
17. Maninder Singh Kamboj, G. Kaur, R. Thangaraj and D. K. Avasthi, J. Phys. D: Appl. Phys. **35** (2002) 477.
18. S. Sorieul, J-M Costantini, L.Gosmain,G. Calas, J-J. Grob and L. Thom´e, J. Phys.: Condens. Matter **18** (2006) 8493.

19. M. Kumar, F. Singh, S. A. Khan, V. Baranwal, S.Kumar, D. C. Agarwal, A. M. Siddiqui, A. Tripathi, A. Gupta, D. K. Avasthi and A. C. Pandey, J. Phys. D: Appl. Phys. **38** (2005) 637.
20. P. M. Ratheesh Kumar, C. Sudha Kartha, K. P. Vijayakumar, F. Singh, D. K. Avasthi, T. Abe, Y. Kashiwaba, G. S. Okram, M. Kumar and Sarvesh Kumar, **97** (2005) 13509.
21. A. Kamarou, W. Wesch, E. Wendler and S. Klaumunzer, Nucl. Instr. and Meth. B **225** (2004) 129.
22. K.Bindu, M. Lakshmi and C. Sudha Kartha, Semicond. Sci. Tech. **17** (2002) 270.
23. J.F. Ziegler, J.P. Biersack, U. Littmark, PC program package TRIM95, 1995.
24. Cullity B.D, Elements of X-ray Diffraction (Reading, M A: Addison-Wesley, 1978), p.170.
25. Wolfgang Bolse, Surface and Coating Technology, **158-159** (2002) 1.
26. W. Wesch, A. Kamarou, E.Wendler, K.G artner, P. I. Gaiduk and S. Klaumunzer, Nucl. Instr. and Meth. B **206** (2003) 1018.
27. J. I. Pankove, Optical process in semiconductors (Dover Publications, Inc. New York 1971), p. 34
28. S. Chakrabarti, D. Ganguli and S. Chaudhuri, Physica E **24** (2004) 333.
29. S.N. Sahu, S.N. Sarangi and K.K. Nanda, Physics of Semiconductor Nanostructures, edited by K.P. Jain, (Narosa Publishing House, 1997), p.202-216.
30. S. Sherman, S. Wagner and R.A. Gottscho, Appl. Phys. Lett. **69** (1996) 3242.
31. K. Saito and A. J. Ikushima, Phy. Rev. B **62** (2000) 8584.
32. J. Cui, Rusli, S. F. Yoon, M. B. Yu, K. Chew, J. Ahn, Q. Zhang, E. J. Teo, T. Osipowicz and F. Watt, J. Appl. Phys. **89** (2001) 2699.
33. Rusli, J. Robertson and G. A. J. Amaratunga, J. Appl. Phys. **80** (1996) 2998.
34. C. Rincon, S. M. Wasim, G. Martin, R. Marquez, L. Nieves, G. Sanchez Perez and E. Medina, J. Appl. Phys. **90** (2001) 4423.
35. B. Gurbulak, Phys. Scr. **70** (2004) 197.
36. H. T. El-Shair and A. E. Bekheet, J. Phys. D: Appl. Phys. **25** (1992) 1122.

37. B. Abay, H. S. Guder, H. Efeoglu and Y. K. Yogurtcu, J. Phys. D: Appl. Phys. **32** (1999) 2942.
38. Maninder Singh Kamboj, R. Thangaraj, D. K. Avasthi and D. Kabiraj, Nucl. Instr. and Meth. B **211** (2003) 369.

CHAPTER 6

Integration of InSb in Si matrix using swift heavy ion irradiation

Abstract

This chapter presents the works done to integrate In/Sb with Si through swift heavy ion beam mixing. The samples of In/Sb deposited on Si substrate were irradiated using 100 MeV Au, 100 MeV Ag and 80 MeV Ni ions. Threshold fluence for InSb phase formation, without any post irradiation annealing, was found to be $1x10^{13}$ ions/cm^2 for all energies. But integration of InSb in Si matrix was achieved only using 100 MeV Au ions with a fluence of $3x10^{13}$ ions/cm^2. Thus the threshold energy required to integrate InSb with Si was found to be 100 MeV of Au, which loses about 19, 16.65 and 11.72 keV/nm as electronic energy loss in In, Sb and Si respectively.

6.1 Introduction

Indium antimonide (InSb) is the binary semiconductor in the III-V group having the lowest band gap of 0.17eV at 300K, corresponding to infrared wavelength 6.2 µm. Another peculiarity of this material is low effective mass and high mobility of carriers [electron] [1, 2]. InSb attracted several research groups because of the wide applications in the fields of magnetic sensors, infrared detectors as well as in infrared laser devices [3-5]. For device applications, amplification and signal processing are required. Usually it has been done using discrete circuits which are physically separated from the InSb sensor array. By Integrating InSb with highly advanced Si circuitry, one could get significant gain in terms of reliability and speed. Moreover, high density of integration will allow considerable cost savings in the manufacturing process. However, direct growth of InSb on the Si substrate is very difficult (because of large lattice mismatch - over 19% - and different thermal expansion co-efficient) and little has been reported in the literature [1, 6, 7]. Recently significant advance in InSb devices has been achieved and developed large area InSb focal plane arrays on Si substrates [8, 9]. Moreover the advantage of growing InSb on Si is the availability of high quality and large size Si substrates. In the present work, integration of InSb with Si was achieved by ion beam mixing of In/Sb layers deposited on Si wafer.

Currently, there is an increasing drive to reduce the synthesis temperature of materials. Different techniques such as molecular beam epitaxy (MBE) [1,10], metal-organic magnetron sputtering [11], metal-organic vapour phase epitaxy [12] and vertical Bridgemen technique [13] have been used to prepare InSb films. All the techniques mentioned here required post deposition annealing of samples or substrate heating (190°C-850°C) during the deposition process, which restricts their application to device fabrication processes capable of withstanding such temperature. Ion beam mixing (IBM) is one of the tools for synthesis of compounds, using low energy ions [14]. The compound phases, in

general, are achievable at relatively lower temperature in the process of ion beam mixing [15]. Advantage of IBM using high energy ($\geq$ 1 MeV/amu) heavy ions (known as SHI) over low energy ion mixing is that, the fluence required for mixing is about 10^{13}ions/cm^2 to 10^{14} ions/cm^2, which is two to three orders of magnitude smaller, compared to low energy ion induced mixing [16]. IBM, using high energy heavy ions, was first demonstrated by Dufour et al. [17] in 1993 and since then, several researchers have shown mixing in various insulator/insulator [18, 19], metal/insulator [20], metal/metal [21, 22] and metal/semi-conductor [15, 17, 23] systems. To the best of our knowledge, there is no report of IBM in semi-metal/metal system, as being reported in the present work.

In the present work, we investigated the compound formation due to mixing induced by 100 MeV Au^{8+}, 100 MeV Ag and 80 MeV Ni ions at In/Sb interface. The ion induced interface modification has been investigated by using high resolution X-ray diffraction (XRD) analysis, X-ray photoelectron spectroscopy (XPS) and Rutherford backscattering spectroscopy (RBS). Variations in composition along the depth of the sample was also analysed with the help of XPS.

6.2 Experiment

In/Sb bilayer systems were prepared on Si (100) wafers. Thin film of In (50 nm thick) was evaporated first (by resistive heating technique), over which 40nm Sb was subsequently deposited (by e-gun evaporation) without breaking the vacuum. Pressure during evaporation was about 1x10^{-6}mbar and the rate of evaporation was 0.2 nm/s. Thickness was monitored with the help of quartz crystal monitor. These samples were irradiated using 100 MeV Au, 100 MeV Ag and 80 MeV Ni ions (from 15 UD Pelletron Accelerator) of fluence ranging from 1x10^{12} ions/cm^2 to 1x10^{14} ions/cm^2 at room temperature (RT) over an area of 1 cm^2 with the help of an electromagnetic scanner. XRD measurements on

unirradiated and irradiated samples were carried out by varying 2θ from 20° to 60° with Cu K_α radiation, employing Philips (X'Pert pro.) X-ray diffractometer. X-ray photoelectron spectra were recorded using an ULVAC-PHI unit (model-ESCA-5600CIM) employing Ar ion sputtering (voltage=3kV, raster size=3mm^2). RBS measurements were done with the help of 3MV Tandem Pelletron Accelerator (Model - 9SDH2). 3MeV He^{2+} ions were used for RBS analysis of the samples, placed at an angle 10^0 to the ion beam and a silicon surface barrier detector placed at 160° in back scattering geometry, to detect the scattered ions. Detector resolution was 20 keV and solid angle was 1msr. RBS analysis was performed with GISA simulation [24].

6.3 Results and discussion

6.3.1 X-ray diffraction analysis

(a) Irradiation using 100 MeV Au ions

Figure 6.1 shows the result of high resolution X-ray diffraction (XRD) analysis of unirradiated and irradiated In/Sb system with different fluences. Unirradiated sample showed a peak of In [at 2θ=33.02^o along (101) plane] and two peaks of Sb [at 2θ=23.84^o and 39.38^o along (003) and (210) planes] [Fig. 6.1(a)]. At the fluence of 1x10^{13}ions/cm^2, InSb phase appeared at 2θ=33.31^o [JCPDS Card: 19-577] along (011) plane (FWHM=0.205) and 2θ=24.13^o [JCPDS Card: 6-208] along (111) plane [Fig. 6.1(b)]. Increasing the fluence to 3x10^{13}ions/cm^2, resulted in a decrease in crystallinity (FWHM = 0.222). A complete mixing was observed with no trace of Sb peak at a fluence of 6x10^{13} ions/cm^2 [Fig. 6.1(d)].

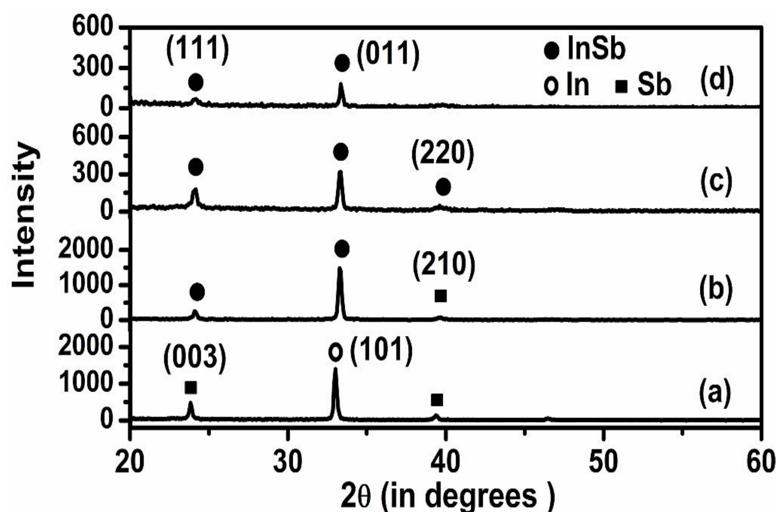

Figure 6.1: XRD pattern of (a) unirradiated and irradiated In/Sb system, with 100MeV Au ions of fluence (b) $1x10^{13}$ions/cm^2 (c) $3x10^{13}$ions/cm^2 and (d) $6x10^{13}$ions/cm^2.

Average grain size of the samples was calculated using Debye scherrer's formula [25]. Average grain size of the samples irradiated with fluences $1x10^{13}$ ions/cm^2, $3x10^{13}$ ions/cm^2 and $6x10^{13}$ ions/cm^2 were 410 Å, 400 Å and 470 Å respectively.

From the XRD analysis, we found that film consisted of mixed phases. The d-values of the InSb peak at $2\theta=24.13^o$ was corresponding to cubic phase whereas that of the peak at $2\theta=33.31^o$ was corresponding to orthorhombic phase of InSb. One could also observe from the XRD pattern that, as the fluence increased from $3x10^{13}$ions/cm^2 [Fig. 6.1(c)] to $6x10^{13}$ ions/cm^2 [Fig. 6.1 (d)], the relative intensity of InSb peak at $2\theta=24.13^o$ decreased from 43.78 to 21.51 with respect to the peak at $2\theta=33.31$ (with relative intensity 100). This showed that as the fluence increased, the growth of orthorhombic phase was preferred at the expense of cubic phase.

(b) Irradiation using 100 MeV Ag ions

XRD patterns of the samples, irradiated with 100 MeV Ag ions in the fluence ranging from $1x10^{12}$ ions/cm^2 to $6x10^{13}$ ions/cm^2 are depicted in Fig. 6.2. InSb phase formation was not observed up to a fluence of $3x10^{12}$ ions/cm^2 (Fig. 6.2(b) and (c)). But as the fluence increased to a value of $1x10^{13}$ ons/cm^2 we could see InSb formation at 2θ=23.81 along (111) plane, 2θ=33.27 along (011) and at 2θ=39.21 along (220) plane. Here also, similar to the case of irradiation with 100 MeV Au ions, the films were formed with cubic and orthorhombic phases of InSb. As the irradiation fluence increased to $3x10^{13}$ ions/cm^2, we could observe a new XRD reflection from 2θ=61.9 corresponding to the cubic phase of InSb (JCPDS card: 36-1284). This sample (irradiated with $3x10^{13}$ ions/cm^2) showed the maximum crystallinity, with an average grain size of 670 Å. However, further increase of fluence to $6x10^{13}$ ions/cm^2 resulted in the decrease of crystallinity and elimination of reflection from 2θ=61.9. Average grain sizes of the samples are tabulated in table 6.1. One interesting thing to be noted here is that preferential orientation is along (111) plane of cubic InSb phase, whereas in the case of 100 MeV Au irradiation, the orthorhombic phase was preferred at higher irradiation fluence.

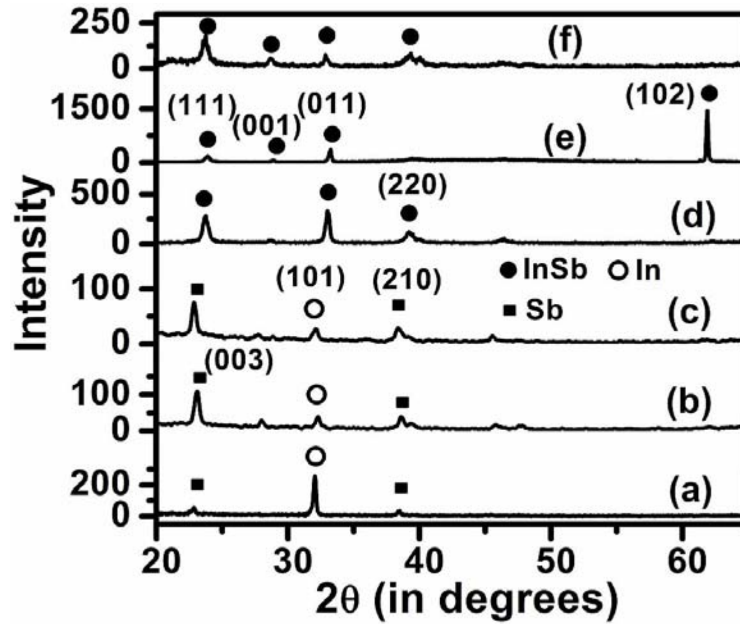

Figure 6.2: XRD pattern of (a) un-irradiated and irradiated In/Sb system, with 100MeV Ag ions of fluence (b) $1x10^{12}$ ions/cm^2 (c) $3x10^{12}$ ions/cm^2 (d) $1x10^{13}$ ions/cm^2 (e) $3x10^{13}$ ions/cm^2 (f) $6x10^{13}$ ions/cm^2

Table 6.1: Variations of grain size with irradiation fluence

Sl. No.	Fluence (ions/cm^2)	2θ	FWHM	Average grain size
1.	$1x10^{13}$	33.27	0.3063	270 Å
2.	$3x10^{13}$	61.9	0.1348	670 Å
3.	$6x10^{13}$	23.81	0.4106	198 Å

(c) Irradiation using 80 MeV Ni ions

Figure 6.3 shows the XRD pattern of In/Sb system irradiated with 80 MeV Ni ions of fluence ranging from $1x10^{12}$ to $1x10^{14}$ ions/cm^2. Here also InSb phase formation induced by irradiation was observed at a fluence of $1x10^{13}$ ions/cm^2. In this case the reflection from cubic phase of InSb at 2θ=61.9 was observed even at $1x10^{13}$ ions/cm^2. Also the growth of cubic phase increased on increasing the fluence to $3x10^{13}$ ions/cm^2. The intensity of the reflection from cubic phase at 2θ=61.9 along (102) plane increased considerably with respect to the peak from orthorhombic phase along (011) plane. On increasing the fluence to $1x10^{14}$ ions/cm^2 the peak at 2θ=61.9 vanished. Crystallinity of the film also degraded. Average grain size of the sample irradiated with fluence $1x10^{13}$, $3x10^{13}$ and $1x10^{14}$ ions/cm^2 were 433 Å (FWHM=0.191), 440 Å (FWHM=0.1882) and 332 Å (FWHM=0.2492) respectively. In this case, the orthorhombic phase dominated the cubic phase. But one interesting point to be considered is that the intensity of reflection from the cubic phase along (111) plane is increasing with respect to the reflection from orthorhombic phase along (011) as the fluence increased. The relative intensity of the (111) plane increased as 18.7, 27 and 64 with fluence $1x10^{13}$, $3x10^{13}$ and $1x10^{14}$ ions/cm^2 respectively. This shows that as the fluence increased, cubic phase was growing at the expense of orthorhombic phase.

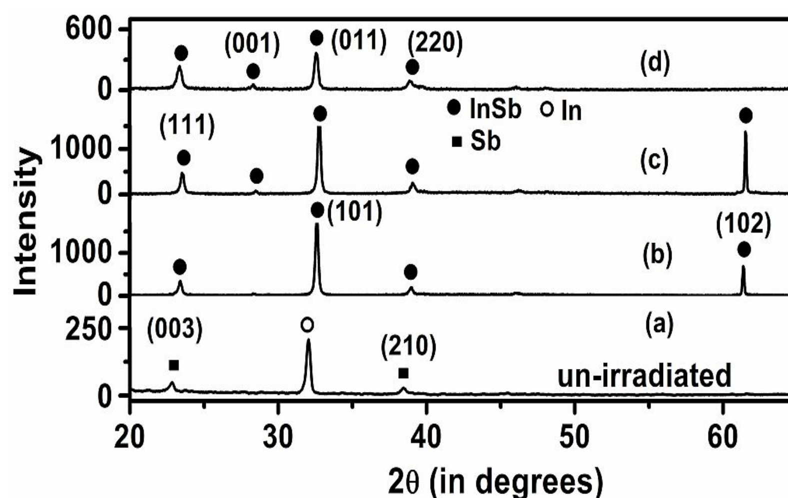

Figure 6.3: XRD pattern of (a) unirradiated and irradiated In/Sb system, with 80 MeV Ni ions of fluence (b) 1×10^{13} ions/cm^2 (c) 3×10^{13} ions/cm^2 (d) 1×10^{14} ions/cm^2.

XRD analysis revealed that InSb phase could be obtained using SHI irradiation, without any post annealing treatment. The electronic energy deposition of different ions of different energies, used in this study is listed in table 6.2. In this study using three different energy regime, we found InSb formation at the fluence of 1×10^{13} ions/cm^2.

Table 6.2: The energy loss of ion beams in In and Sb respectively.

Sl. No.	Energy & ion beam	Electronic energy loss (in keV)		
		In	Sb	Si
1.	100 MeV Au	19	16.65	11.72
2.	100 MeV Ag	17.75	16	10.51
3.	80 MeV Ni	12.03	10.91	7.03

Interface mixing using SHI irradiation could be explained on the basis of “thermal spike model” [32]. As explained in the previous chapters, SHI deposits tremendous amount of energy on passing through the material. This causes temperature rise in the material for nano second duration. This can create molten tracks having few nano-meters in diameter and few tens of nanometer in length in the direction of propagation. As the ion fluence increases, these tracks elongate along the direction of propagation, and overlap to get uniform mixing at the interface. The dependence of ion track radius and electronic energy loss is shown by many scientists and proved that the track radius increased with the increase of electronic energy deposited in the material. This suggests that, for higher electronic energy loss, radius of the molten track would be higher and the overlapping of tracks would be occurring with lower ion fluence. But in the present case, [irradiation using 100 MeV Au, 100 MeV Ag and 80 MeV Ni ions], we obtained mixing between In and Sb at the fluence of $1x10^{13}$ ions/cm^2. This again suggested that for all these ions of different energies, the molten track radius might be the same or comparable. This might be the reason for obtaining interface mixing at the fluence of $1x10^{13}$ ions/cm^2 for all the three ions.

6.3.2 Rutherford backscattering analysis

RBS analysis was carried out to study the mixing between In/Sb bilayers. Because of the closeness of the density between In and Sb (7.3 g/cm^2 and 6.68 g/cm^2 respectively), we were not able to deduce any useful information about the mixing between layers of In and Sb. But we could get the information of mixing or embedment of InSb in Si wafer/ substrate, using RBS measurements. Figure 6.4 displays the RBS spectra of unirradiated In/Sb system in which one can see that channel number of In and Sb are overlapped.

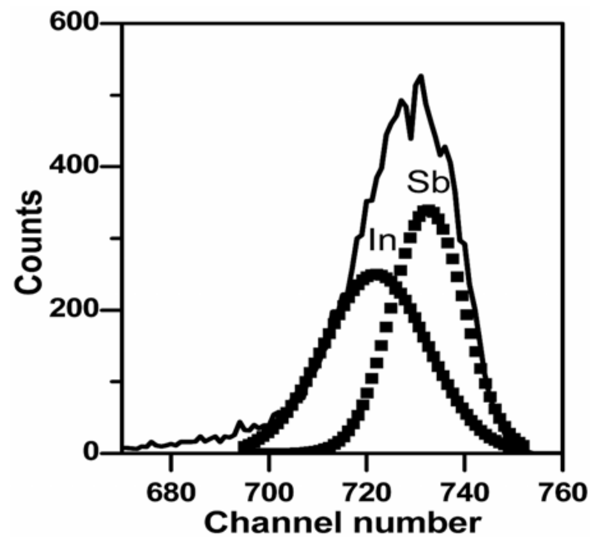

Figure 6.4: RBS spectra of unirradiated Si/In/Sb system. Line (—) plot shows the experimental spectra whereas, dark dotted square (■) plot shows the fitted curve.

Figure 6.5 shows the RBS spectra of Si/In/Sb system irradiated with 100 MeV Au ion beam of fluence of $3x10^{13}$ions/cm^2. Even though it was not possible to resolve peaks of In and Sb in RBS spectra (because of the closeness of density between In and Sb), one could observe that the lower energy edge of 'In peak' was shifted towards the substrate edge due to irradiation with a fluence of $3x10^{13}$ ions/cm^2. This was due to embedment of InSb into Si substrate [27, 28]. No embedment was observed up to a fluence of $1x10^{13}$ ions/cm^2.

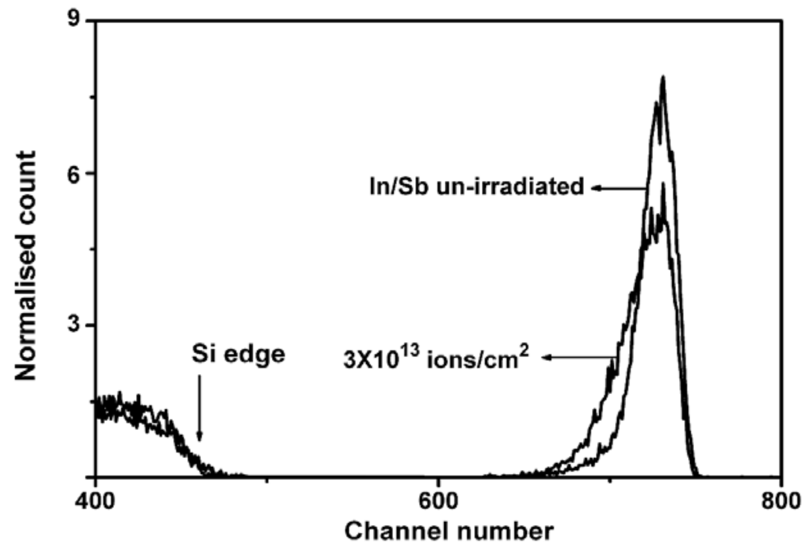

Figure 6.5: RBS spectra of unirradiated and irradiated Si/In/Sb system using $3x10^{13}$ ions/cm^2 of 100 MeV Au ions.

RBS spectra of samples irradiated with 100 MeV Ag and 80 MeV Ni ions were also recorded. But there was no sign of embedment of InSb. Figure 6.6 depicts RBS spectra of the sample irradiated using 100 MeV of Ag ions of fluence $6x10^{13}$ ions/cm^2. One can not find any incorporation of InSb in Si matrix as observed in the case of sample irradiated with 100 MeV Au ions. This proved that the energy required for incorporating InSb in Si matrix can be supplied by 100 MeV Au, which is 19, 16.65 and 11.72 keV/nm in In, Sb and Si respectively.

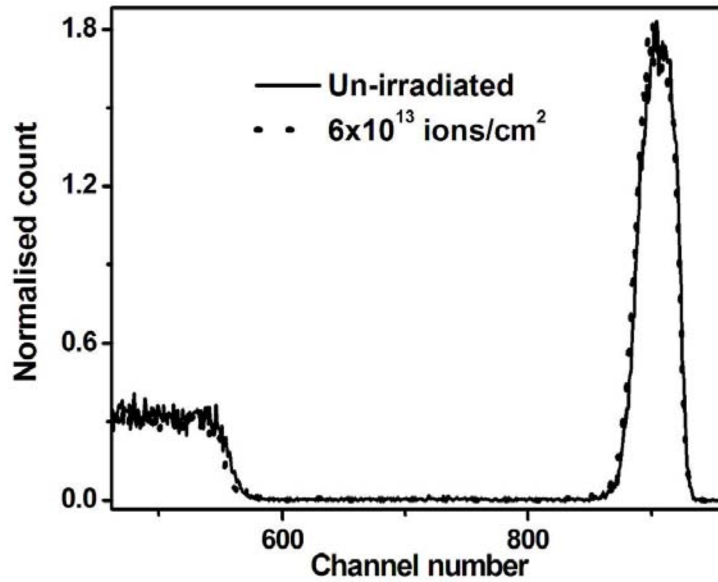

Figure 6.6: RBS spectra of unirradiated and irradiated Si/In/Sb system using $6x10^{13}$ ions/cm^2 of 100 MeV Ag ions.

6.3.3 X-ray photoelectron spectroscopy analysis

Figure 6.7 shows the X-ray photoelectron spectra (depth-wise compositional analysis) of In/Sb system, irradiated with different fluences of Au ions. One can understand from the figure that composition of In and Sb was almost constant up to $3x10^{12}$ ions/cm^2. Atomic concentrations of In as well as Sb decreased on irradiation with a fluence of $1x10^{13}$ ions/cm^2 (Fig. 6.7(c)). This was attributed to the mixing between In and Sb. On increasing fluence to $3x10^{13}$ ions/cm^2 we could observe that both In and Sb were embedding into the Si substrate (Fig. 6.7(d)].

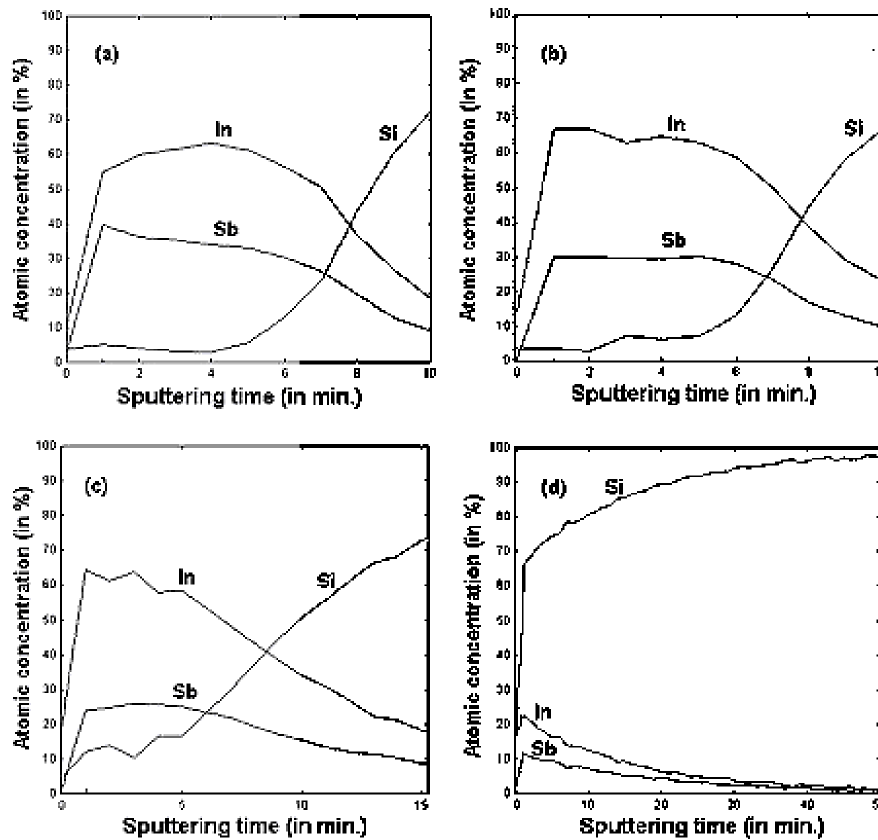

Figure 6.7: XPS spectrum showing atomic concentration of In and Sb in Si/In/sb system irradiated with different fluence of Au ions (a) un-irradiated (b) $3x10^{12}$ ion/cm^2 (c) $1x10^{13}$ ion/cm^2 (d) $3x10^{13}$ ion/cm^2.

The composition of InSb was found to be $In_{0.71}Sb_{0.29}$ for the film irradiated with $1x10^{13}$ ions/cm^2 and was able to obtain stoichiometric InSb with a composition of $In_{0.58}Sb_{0.42}$ with a fluence of $3x10^{13}$ ions/cm^2. With this fluence ($3x10^{13}$ions/cm^2) we could get embedded InSb system in Si up to a depth of 0.30μm.

Figure 6.8 shows the results of XPS analysis (binding energy versus depth) of In/Sb system. Binding energy (B.E) of In and Sb were 444.2eV and 528eV respectively (Fig. 6.8(a)). But the B.E of In ($3d_{5/2}$) in the elemental state was in the range 443.57eV - 444 and that in InSb was in the range 443.82eV - 444.32eV [26]. Hence it was confirmed from the B.E values that, InSb phase was formed after irradiating with a fluence of 1×10^{13} ions/cm^2. B.E of elemental Si was in the range 98.79eV-99.5eV and that of silicides were between 99.38eV and 99.92eV [26]. Here we could notice that, with increase in fluence from 1×10^{13} ions/cm^2 onwards, there was a shift in Si peak towards higher B.E. This suggested the possibility of silicide formation. However the results from XRD studies did not reveal any silicide formation. Hence the shift in Si peak might be more likely due to the embedment of In and Sb into the silicon.

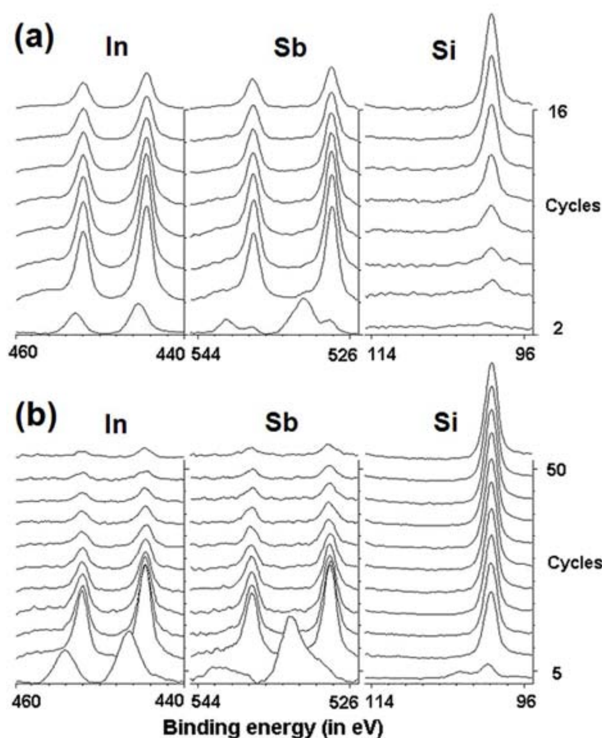

Figure 6.8: XPS spectrum (B.E Versus depth) of Si/In/Sb system irradiated with Au ions of fluence (a) $1x10^{13}$ions/cm^2 (b) $3x10^{13}$ions/cm^2.

It was observed that the, compound formation between In and Sb occurred on irradiation with 100 MeV Au, 100 MeV Ag and 80 MeV Ni ions, with a fluence of $1x10^{13}$ions/cm^2 at room temperature. No compound formation took place for the fluences $1x10^{12}$ ions/cm^2 and $3x10^{12}$ ions/cm^2. This indicated that the threshold fluence for compound formation to take place between In and Sb was about $1x10^{13}$ ions/cm^2. RBS analysis showed that the integration of InSb with Si was possible only with 100 MeV Au ion irradiation. As the fluence increased above the threshold fluence ($1x10^{13}$ ions/cm^2), the intensity of the XRD peaks

decreased. This might be due to the creation of defects by SHI irradiation [29, 30]. But in the case of samples irradiated with 100 MeV Au ions, the average grain size of the crystallites remained constant around 400 Å. This suggested that the decrease in XRD peak intensity was due to the embedment of InSb into the Si substrate. Since XRD analysis did not reveal any silicide formation we could rule out any compound formation between Si and InSb. With higher fluence ($3x10^{13}$ ions/cm^2 and above) the Sb peak (at 2θ=39.33) almost vanished. This indicated that Sb completely mixed with In to form InSb. B.E values from XPS analysis (Fig. 6.8) also confirmed the compound formation (InSb). Depth profiling using XPS (Fig. 6.7(d)) showed embedment of InSb into Si up to a depth of 0.30µm with a fluence of $3x10^{13}$ ions/cm^2. This could be observed in figure 6.8(b) in which we noticed a peak shift of Si to higher B.E.

Essential condition for swift heavy ion beam induced mixing to take place between a bilayer system (say In/Sb) was that, the interface of the two layers should be in a transient molten state [18, 31]. Each material has a threshold value of electronic stopping power (Se) to become molten. Saskia Kraft et al. studied the mixing of Ni/Sb (metal/semi-metal) interface by using 200MeV Xe ions with fluences $1.4x10^{15}$ ions/cm^2 and $4.2x10^{15}$ ions/cm^2 [18]. They found that there was no mixing between Ni/Sb, as the melting point of Ni was 1453°C and that of Sb was 630°C. But in the present case (in In/Sb), the melting point of In is only 157°C, so that 12.03 keV/nm 10.91 keV/nm might be sufficient for In and Sb to form molten state at the interface. Thus a metal/semi-metal mixing, induced by SHI, in electronic energy regime was observed.

One could explain the mixing between In and Sb using “thermal spike” model [32]. According to this model, kinetic energy of excited electrons was transferred to lattice via electron – phonon coupling. Recently it has been shown by Srivastsva et al. [33] that the mixing in Fe/Si was a consequence of inter-diffusion during transient melting. In the present case too, the passage of SHI caused tremendous increase in local temperature, thereby creating a transient

molten state of In and Sb (for about pico second duration), resulting in atomic transport across the interface, to form the binary compound InSb. Since in metals and semi-metals, conduction electrons would quickly smear out the excitation and ionization of atoms, the possibility of Coulomb explosion was ruled out.

6.4 Conclusion

Integration of InSb system with Si matrix was achieved using SHI irradiation. 100 MeV Au ions of fluence $3x10^{13}$ is required to integrate InSb in Si up to a depth of 0.30μm. InSb can be prepared on Si substrate using SHI irradiation without any post annealing treatment at room temperature. Threshold fluence for compound formation to take place between In/Sb was found out to be $1x10^{13}$ ions/cm^2 using 100 MeV Au, 100 MeV Ag and 80 MeV Ni ions. Threshold energy loss for integrating InSb with Si was found to be 19, 16.65 and 11.72 keV/nm in In, Sb and Si respectively.

References

1. B.V. Rao, D. Gruznev, T. Tambo and C. Tatsuyama, Semicon. Sci. Technol. **16** (2001) 216
2. Stradling. R. A, Braz. J. Phys. **26** (1996) 7
3. Gert Finger, Reinhold J. Dorn, Manfred Meyer, Leander Mehrgan, Jorg Stegmeier and Alan Moorwood, Nucl. Instr. and Meth A. **549** (2005) 79
4. Atsushi Okamoto, Takashi Yoshida, Shogo Muramatsn and Ichiro Shibasaki, J. Crystal Growth **201** (1999) 765
5. Ozer. S and Besikci, J. Phys. D : Appl. Phys. **36** (2003) 559
6. B.V. Rao, Atoji. M, Li D M, Okamoto. T, Tambo. T and Tatsuyama. C, Jap. J. Appl. Phys. **37** (1998) L1297
7. Franklin. G. E, Rich. D. H, Hawoong Hong, Miller. T and Chiang T. C, Phy. Rev. B **45** (1992) 3426
8. Michel. E, Xu J, Kim J. D, Ferguson. I and Razeghi. M, IEEE Phot. Tech. Lett. **8** (1996) 673
9. Rogalski. A, Infrared Phys. Technol. **43** (2002) 187
10. Orias. G, Hoffman A. W and Casselman M. F, SPIE J. **627** (1986) 408
11. Webb. J. B and Halpren. C, Appl. Phys. Lett. **47** (1985) 831
12. Chang. P. K and Bedair S. M, Appl. Phys. Lett. **46** (1985) 383
13. N. K. Udayasankar and N.L. Bhat, Bull. Mater. Sci. **24** (2001) 445
14. Sankar Kumar and V. N. Kulkarni, Thin Solid Films **333** (1998) 20
15. Sarvesh Kumar, R. S. Chauhan, R. P. Singh, W. Bolse and D. K. Avasthi et al. Nucl. Instr. and Meth. B **212** (2003) 242
16. D.K. Avasthi, Current Science **78** (2002) No: 11, 1297
17. C. Dufour, Ph. Bauer, G. Marchal, J. Grilhe, C. Jaouen, J. Pacaud and J. C. Jousset, Europhys. Lett. **21**(6) (1993) 671
18. Saskia Kraft, Beate Schattat and Wolfgang Bolse, J. Appl. Phys. **91** (2002) 1129
19. D.K. Avasthi, W. Assmann, H. Nolte and H.D. Mieskes, Nucl. Instr. and Meth. B **156** (1999) 143

20. Ajay Gupta, Suneel Pandita, D. K. Avasthi, G. S. Lodha and R. V. Nandedkar, Nucl. Instr. and Meth. B **146** (1998) 265
21. R. Lagnay, A. Dunlop, F. Dunstter and N. Lorenzelli, Nucl. Instr. and Meth. B **106** (1995) 28
22. Alejandro Crespo-Sosa, Manuel Munoz and Juan-Carlos Cheang-Wong, Materls. Sci. and Eng. B **100** (2003) 297
23. S. K. Srivastava, D. Kabiraj, B. Schattat, H. D. Carstanjen and D. K. Avasthi, Nucl. Instr. and Meth. B **219** (2004) 815
24. S. Rath and S. N. Sahu, Europhys. Lett. **67** (2004) 294
25. Cullity B.D, Elements of X-ray Diffraction (Reading, M A: Addison-Wesley) 1978 page no:170
26. Jill Chastain, Handbook of X-ray Photoelectron Spectroscopy, Elmer Corporation, United States of America. 1992 page no: 125, 57
27. M. Milosavljevic, G. Shao, R. M. Gwilliam, C. Jeynes, C.N. Mc Kinty and K. P. Homewood, Nucl. Instr. and Meth. B **175-177** (2001) 309
28. L. Rissanen, S. Dhar, K.P. Lieb, K. Engel and M. Wenderoth, Nucl. Instr. and Meth. B **161-163** (2000) 986
29. P.Satyavathi, S.T. Chavan, D. Kanjilal and V.N. Bhoraskar, Nucl. Instr. and Meth. B **156** (1999) 72
30. S.T. Chavan, P.S. Bhave, V.N. Bhoraskar and D. Kanjilal, J. Appl. Phys. **78** (1995) 2328
31. Wolfgang Bolse and Beate Schattat, Nucl. Instr. and Meth. B **190** (2002) 173
32. Z.G. Wang, C. Dufour, E. Paumier and M. Toulemonde, Phys.: Condens. Matter **6** (1994) 6733
33. S.K. Srivastava, D.K. Avasthi, W. Assmann, Z. G. Wang, H. Kucal, E. Jacquet, H.D. Carstanjen and M. Toulemonde. Phy. Rev. B **71** (2005) 193405

CHAPTER 7

Summary and outlook

Abstract

This chapter summarises the results obtained in the entire work followed by the scope for the future work.

7.1 Conclusion

From the present work we can conclude that single phase indium selenide can be prepared using SHI irradiation at relatively lower annealing temperature of 100°C, whereas a temperature of 400°C is required without irradiation. Interestingly γ-In_2Se_3 thin film prepared using this method (annealing only) exhibited negative photoconductivity even at room temperature. This behaviour showed by γ-In_2Se_3 is due to the trapping of photogenerated carriers at trap levels, 1.46 and 1.32 eV and destruction of conduction band electrons at recombination centre at 290 meV above valance band on illumination. SHI irradiation annihilated the trap levels in the sample and converted negative photoconductivity to positive photoconductivity. Structural analysis proved that the growth of γ-In_2Se_3 along c-axis depends on In concentration and annealing temperature. However Se rich indium selenide film never grew along c-axis whatever may be the annealing temperature. Irradiation using 40 MeV Si ions resulted in the variation of the band gap of γ-In_2Se_3 from 2 eV to 2.8 eV. In fact this is due to the reduction of Urbach energy induced by SHI irradiation. On-line RBS study using 40 MeV Si ions proved that swift heavy ions can be used for online interface mixing study. Irradiation study at different electronic energy regime explored the threshold fluence for mixing to take place between In/Se bilayer system is $6x10^{12}$, $1x10^{13}$ and $1x10^{14}$ ions/cm^2 for 100 MeV Ag, 80 MeV Ni and 90 MeV Si ions respectively.

Irradiation study in In/Sb system, deposited on Si substrate, proved that InSb can be prepared on Si substrate using SHI irradiation at room temperature. This work also proved that InSb can be integrated with Si matrix using 100 MeV Au ion irradiation without any post annealing treatment. To the best of our knowledge there is no report on integration of InSb with Si using IBM technique.

7.2 Scope for future work

The present study proved that the structural, electrical and optical properties of γ-In_2Se_3 can be improved using SHI irradiation. Hence we can adapt this technique to increase the band gap of indium selenide and could fabricate $CuInS_2/In_2Se_3$ solar cells. As we are using SHI irradiation, there is no need to decrease the thickness of the window layer, and we can get better solar cell characteristics than that obtained earlier in $CuInSe_2/In_2Se_3$ based solar cells. Since single phase films without traps are forming induced by SHI irradiation we can expect more reliable and better reproducibility. Lots of work has been done on $CuInSe_2/In_2Se_3$, and CdS/In_2Se_3 p-n junctions. But with $CuInS_2/In_2Se_3$ junctions, little work was reported. Because both $CuInS_2$ and γ-In_2Se_3 have tetragonal structure with lattice parameter a = 5.52Å, c = 11.13Å and a = 7.11Å, c = 19.34Å respectively, lattice mismatch will be very much less. This opens a new scope for future work.

The fact that InSb could be integrated with Si using SHI irradiation even at room temperature will really benefit semiconductor industry, since they are using discrete circuits which are physically separated from the InSb sensor array for signal processing and amplification. By Integrating InSb with highly advanced Si circuitry, one could get significant gain in terms of reliability and speed. Moreover, high density of integration will allow considerable cost savings in the manufacturing process.